1-1-2005

Use of alloy 800H for applications in hydrogen generation using nuclear power

Vinay Virupaksha
University of Nevada, Las Vegas

USE OF ALLOY 800H FOR APPLICATIONS IN HYDROGEN GENERATION USING NUCLEAR POWER

by

Vinay Virupaksha

Bachelor of Engineering in Mechanical Engineering
University of Mysore, Mysore, India
August 2001

A thesis submitted in partial fulfillment of the
requirements for the

Master of Science Degree in Mechanical Engineering
Department of Mechanical Engineering
Howard R. Hughes College of Engineering

Graduate College
University of Nevada, Las Vegas
May 2006

UNLV
UNIVERSITY OF NEVADA LAS VEGAS

Thesis Approval

The Graduate College
University of Nevada, Las Vegas

March 31, 2006

The Thesis prepared by

Vinay Virupaksha

Entitled

Use of Alloy 800H for Applications in Hydrogen Generation using Nuclear Power

is approved in partial fulfillment of the requirements for the degree of

Master of Science Mechanical Engineering

Gigis K. Roy
Examination Committee Chair

Dean of the Graduate College

Kathy E. Hechanova
Examination Committee Member

Brendan J. Toole
Examination Committee Member

Edward S. Neumann
Graduate College Faculty Representative

ABSTRACT

Use of Alloy 800H for Applications in Hydrogen Generation using Nuclear Power

by

Vinay Virupaksha

Dr. Ajit K. Roy, Examination Committee Chair
Associate Professor of Mechanical Engineering
University of Nevada, Las Vegas

Alloy 800H, a candidate structural material for heat-exchangers to be used in nuclear hydrogen generation, was investigated for its high-temperature tensile properties and corrosion behavior. The tensile properties evaluated at different temperatures indicate that Alloy 800H was capable of maintaining high strength up to 600°C followed by its reduction in yield strength and ultimate tensile strength beyond this temperature. Further, the ductility was reduced at some critical temperatures, possibly due to the dynamic strain aging effect. Alloy 800H did not exhibit cracking in acidic aqueous solutions, both under constant-load and self-loaded conditions. Slight reductions in the true failure stress, percent elongation, percent reduction in area, and time-to-failure were observed when tested under a slow-strain-rate condition. The critical potentials became more active with increasing temperature determined by an electrochemical technique. The effect of anodic applied potential was more pronounced on the cracking susceptibility. Dimpled microstructures, characteristic of ductile failure, with some intergranular cracks were observed in the tested specimens. Typical austenitic grains with annealing twins and precipitates were observed in the microstructure.

TABLE OF CONTENTS

LIST OF TABLES

LIST OF FIGURES

ACKNOWLEDGMENTS

I am extremely indebted to Dr. Ajit Roy, who has given me so much guidance, insight and encouragement throughout this research. From the beginning, he had confidence in my abilities to not only complete a degree, but to complete it with excellence. I have found my research stimulating and thoughtful, providing me with the tools to explore new horizons.

I am thankful to Dr. Anthony E. Hechanova, Dr. Brendan J. O'Toole, Dr. Edward S. Neumann, and other faculty members for their support, patience and good humor.

I would like to acknowledge the assistance offered by my colleagues at the Materials Performance Laboratory, UNLV. I appreciate Kam Products for providing the specimens at the right time for this work. I would like to thank my friends and family members for their support and patience. I express my gratitude to Ancila for her continuous support suggestions and encouragement in many ways. Finally, the financial support of United States Department of Energy is thankfully acknowledged.

The number of people that have contributed towards this research during the past two years is too high to list them explicitly, so rather than risking forgetting anybody, I would just like to thank all of you.

CHAPTER 1

INTRODUCTION

Since the mid-19th century, the world has seen a gradual shift from one form of energy to another, specifically from wood to coal to liquids to gases. The latest form of energy includes hydrogen (H_2). The driving forces behind these gradual shifts are twofold: increase of energy density at one hand, and easiness of transport at the other. Oil is easier to transport than coal, and natural gas is even easier to transport through pipelines than oil. Fossil fuels have been the primary source of energy for an extended period, still providing about 68% of the power requirements in the United States (U.S.), as shown in Figure 1.1 [1-3].

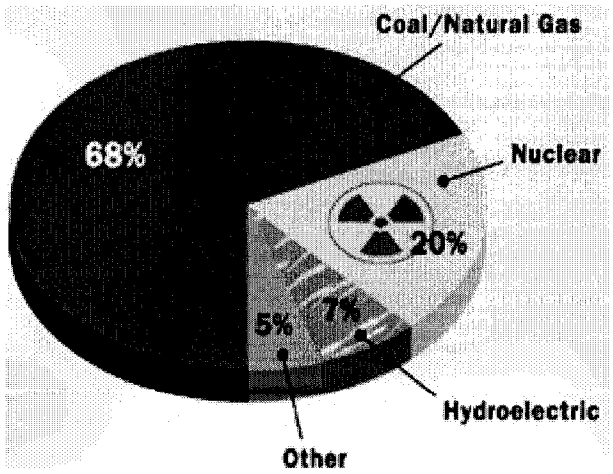

Figure 1.1. Distribution of US Power Source

Due to the growing demand of oil and gas, their productions are expected to reach the pinnacle by the year 2010. The ongoing dependence on expensive fossil fuels has created a significant interest worldwide to explore alternate sources of energy and to develop them in a cost-effective manner. Since 55% of the fuel need in the U.S. is met by import, and the oil and gas prices are increasing at an alarming rate, there are needs to develop non-fossil fuels. However, the alternate sources of energy to be developed in the future must be clean, environment-friendly and cost-effective. H_2 is considered to be one such energy that has been proposed to be developed by the United States Department of Energy (USDOE) for commercial applications.

The H_2 economy promises to eliminate problems associated with the fossil fuel generation, which includes the elimination of environmental pollution, greenhouse gases, and economic dependence. H_2 is the lightest and the most abundant element in the universe, and makes up about 90% of its weight. The demand for H_2 is expected to rise with a factor of four. This increased demand is independent of any future H_2 utilization yet to occur due to the increased demand from the chemical, fertilizer, and petrochemical industries including oil-refineries. Numerous methods have been identified to produce pure H_2 in a cost-effective manner. However, a majority of these methods involves high temperatures and hence, needs high heat sources. Clean H_2 generated in a cost-effective manner on a commercial scale, and the subsequent production of electricity from it is expected to dominate the world energy system in the long run.

One of the existing methods to produce H_2 in small quantities is steam reforming of natural gas, which can generate a major portion of H_2 currently being used [4]. A promising alternative method of producing H_2 is to use process heat from a high-

temperature nuclear reactor to drive a set of chemical reactions. The primary reason for the production of H_2 using nuclear heat includes its cleanliness and capability of generation on a continuous basis. It can also result in reduced or almost no emission of carbon dioxide (CO_2), thus, producing no greenhouse effect.

The USDOE is currently considering both the high-temperature electrolysis and thermochemical processes to produce H_2 involving nuclear power as a potential source of heat. The thermochemical production of H_2 involves the dissociation of water into H_2 and oxygen (O_2) through chemical reactions at high temperatures. So far, two thermochemical processes are being envisioned, namely the sulfur-iodine (S-I) and calcium-bromine (Ca-Br) cycles, none of which would result in CO_2 emission. Also, the reactants used in these processes can be recycled for repeated generation of H_2, rendering them to be more efficient than the high-temperature electrolysis process. The efficiency of the thermochemical water-splitting cycles may be estimated to be around 50% [5, 6], while that of the high-temperature electrolysis may be substantially less due to the unusually high temperature needed to dissociate water [7].

Since significant scientific and technical knowledge currently exists on the S-I cycle, the USDOE is seriously considering this process as the primary method of H_2 generation through utilization of nuclear heat. The maximum temperature proposed for the S-I cycle is in the vicinity of 950°C. Conversely, the Ca-Br process may operate at relatively lower temperatures. However, the efficiency of the later cycle is estimated to be reasonably lower (~40%), compared to that of the S-I cycle (~50%) [8].

The S-I process will consist of three chemical reactions [9] leading to the dissociation of water using iodine (I_2) and sulfur dioxide (SO_2) as chemical catalysts, as shown in Figure 1.2. These reactions are given below.

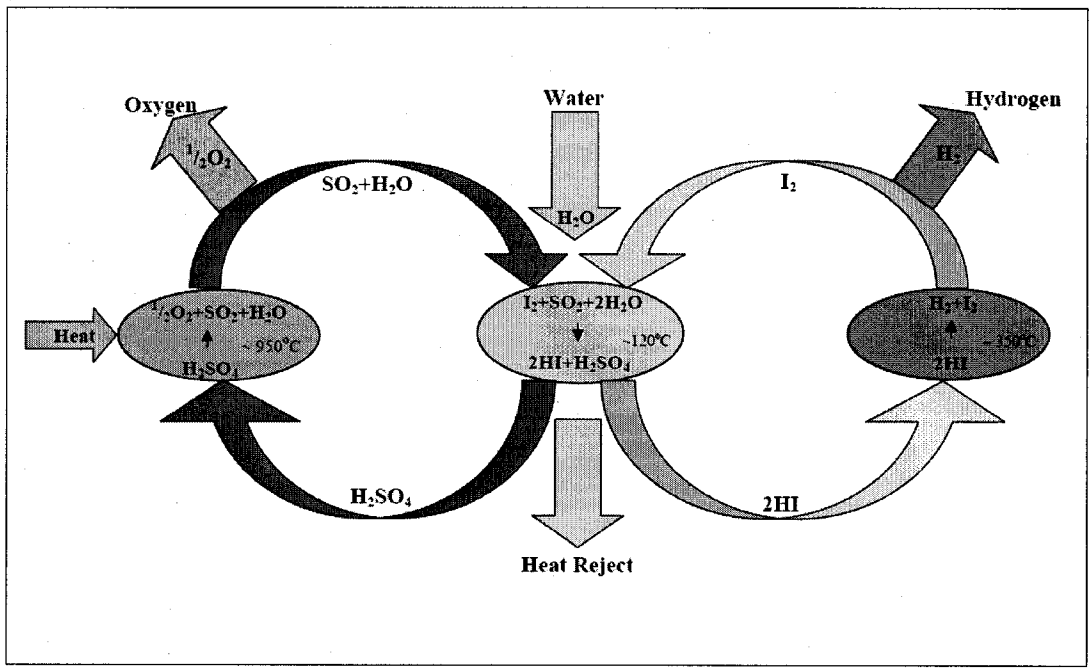

Figure 1.2. Sulfur-Iodine Cycle

$$I_2 + SO_2 + 2H_2O \rightarrow 2HI + H_2SO_4 \qquad \text{(Temperature} \sim 120°C\text{)}$$

$$H_2SO_4 \rightarrow H_2O + SO_2 + \tfrac{1}{2} O_2 \qquad \text{(Temperature} \sim 950°C\text{)}$$

$$2HI \rightarrow H_2 + I_2 \qquad \text{(Temperature} \sim 350°C\text{)}$$

$$H_2O \rightarrow H_2 + \tfrac{1}{2} O_2$$

As shown in Figure 1.2, water reacts with I_2 and SO_2 to form hydrogen iodide (HI) and sulfuric acid (H_2SO_4), which will eventually be separated from each other. I_2 and SO_2 are then recovered as byproducts from the breakdown of HI and H_2SO_4, and recycled. H_2

and O_2 gases will then be collected separately. As shown above, the reaction that requires the greatest heat input is the thermal decomposition of H_2SO_4 that lies in the vicinity of 950°C. Since the efficiency of the process (H_2 produced per unit of heat input) decreases rapidly at reduced temperatures, high temperatures are necessary to produce large quantities of H_2 in a cost-effective manner. A schematic view of the H_2 generation system involving a nuclear reactor, an intermediate heat exchanger, and a H_2 generation plant is shown in Figure 1.3.

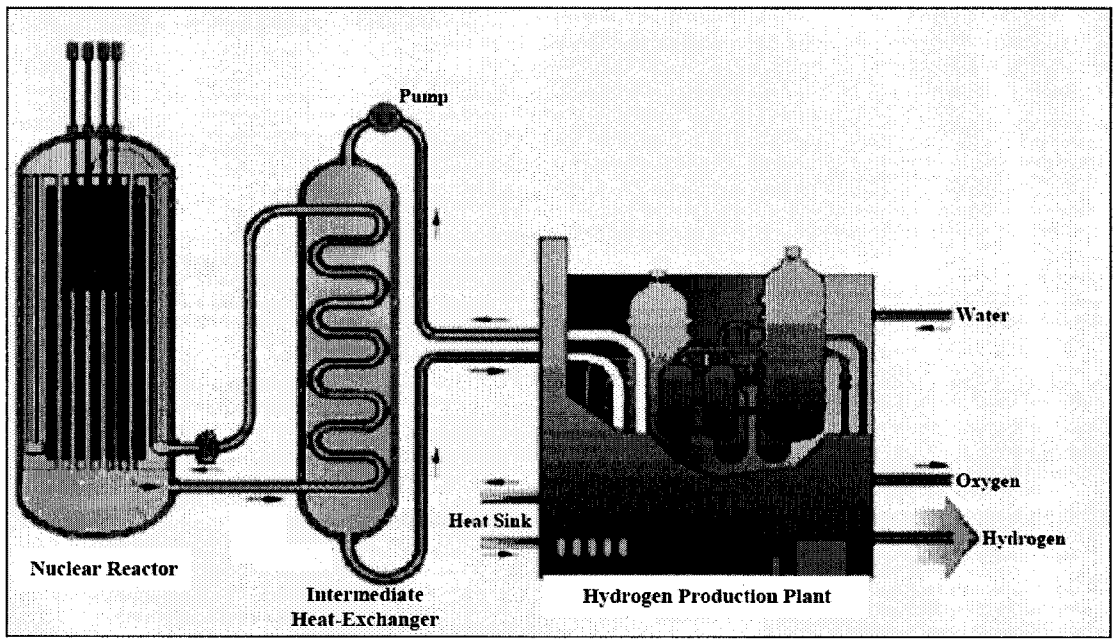

Figure 1.3. Nuclear Hydrogen Generation System

It is obvious from the preceding discussion that the heat exchanger system (S-I cycle) proposed for nuclear H_2 generation will have to operate at an approximate temperature of 950°C in the presence of aggressive chemical species such as H_2SO_4 and HI. Thus, the structural materials to be used in the H_2-producing heat exchangers may become

susceptible to different forms of environment-assisted degradation. Further, these components may develop high stresses resulting from plastic deformation during the fabrication processes, thus, subjecting them to the stressed condition at elevated temperatures. Obviously, the selected structural materials must possess excellent corrosion resistance and superior high-temperature tensile properties including strength and deformation resistance. While the concept of H_2-generation using the S-I cycle is being explored nationally, the researchers at the University of Nevada, Las Vegas (UNLV) have been concentrating on the identification and characterization of suitable structural materials for such applications. Different types of structural materials are currently being investigated at the Materials Performance Laboratory (MPL), UNLV to characterize their metallurgical and the corrosion behavior under simulated conditions. This investigation is focused on presenting the results of metallurgical and corrosion studies involving Alloy 800H for prospective applications as a heat exchanger material in nuclear H_2 generation using the S-I cycle.

The use of Alloy 800H, an iron-nickel-chromium (Fe-Ni-Cr) alloy, possessing high strength, appreciable resistance to oxidation and carburization at elevated temperatures, and excellent corrosion resistance in a wide variety of hostile environments is well documented in the published literature [10-14]. The high strength and superior corrosion resistance of this alloy may be attributed to the continuous matrix of face centered cubic solid solution of chromium and iron in large amount [15]. Alloy 800H has been known to be suitable for high-temperature equipment in the petrochemical industry due to the absence of the embrittling sigma phase which may develop after prolonged exposure at temperatures up to 1200°F (649°C), where many stainless steels can undergo

embrittlement. Excellent resistance to chloride-induced stress-corrosion-cracking (SCC) is another beneficial important feature of this alloy. Alloy 800H is a solution heat-treated (2100°F/1150°C), controlled-carbon version of Alloy 800 with improved elevated temperature properties. It has improved creep and stress-rupture characteristics in the 1100 to 1800°F (593 - 982°C) temperature range. Typical applications of Alloy 800H are in heat exchangers and process piping, furnace components, electric range heating-element sheathing, ammonia effluent coolers and hydrocarbon processing industry]y. Alloy 800H has also been used in power generation for steam superheating tubing and high temperature heat exchangers in gas-cooled nuclear reactors [16]. The chemical balance allows this alloy to exhibit excellent resistance to carburization, oxidation and nitriding atmospheres. The superior mechanical properties of Alloy 800H combined with its excellent resistance to high temperature corrosion make this alloy exceptionally useful for many applications involving long-term exposure in highly corrosive environment at unusually elevated temperatures.

This investigation is focused on the metallurgical and corrosion characterization of Alloy 800H for application as a heat exchanger material in nuclear H_2 generation using the S-I cycle. Even though the decomposition of H_2SO_4 is proposed to occur at a maximum temperature of 950°C, it is extremely difficult to evaluate the performance of Alloy 800H in the presence of H_2SO_4 at such an elevated temperature. Therefore, extensive efforts have been made in this study to characterize the corrosion susceptibility of this alloy in a simulated aqueous solution containing H_2SO_4 and sodium iodide at relatively lower temperatures using different state-of-the-art experimental procedures. The susceptibility of this candidate alloy to SCC has been determined under both

constant-load and slow-strain-rate (SSR) condition. The localized corrosion behavior of this alloy has been studied by an electrochemical polarization method. Further, the cracking susceptibility of this alloy has been determined under anodic and cathodic controlled potential using the SSR technique, since, the application of external potential is known to influence the cracking propensity while the specimens are loaded in tension in damaging aqueous environments.

The tensile properties of Alloy 800H have been evaluated in the presence of an inert atmosphere at temperatures ranging between ambient and 1000°C. The morphology of failure of specimens used in both corrosion and tensile testing has been determined by scanning electron microscopy. Further, the metallurgical microstructure of the tested material has been evaluated by optical microscopy. This thesis presents the comprehensive test results obtained from corrosion studies, tensile testing and microscopic evaluations. It is anticipated that the findings of this investigation may shed a significant light on the basic understanding of high-temperature deformation mechanism, and degradations of Alloy 800H in environments relevant to the H_2 generation using nuclear power.

CHAPTER 2

TEST MATERIAL, SPECIMEN AND ENVIRONMENT

2.1. Test Material

The proposed application of the sulfur-iodine (S-I) cycle involving high temperature (up to 950°C) and the presence of aggressive chemical species (SO_2, I_2) necessitates the identification and selection of a suitable structural material to sustain such operating conditions. Based on the literature search and the recommendation of the national materials advisory board, Alloy 800H was selected as one of the candidate material for evaluation of its metallurgical and corrosion properties. Alloy 800H, also known as Incoloy 800H, was originally developed by the Special Metals Corporation Group of Companies to achieve high-temperature strength and superior resistance to oxidation, carburization and corrosion for numerous industrial applications [17-45].

Compared to the conventional nickel-base alloys, Alloy 800H contains relatively less nickel content, low carbon and substantial chromium content to provide the desired metallurgical and corrosion properties for applications under many hostile operating conditions. This alloy has been known to be highly resistant to corrosive degradation in many environments while maintaining the structural stability at elevated temperatures. It is interesting to note that Alloy 800H is synonymous with Alloy 800HT and 800 in terms of its chemical composition with a slight variation in composition limits for carbon,

aluminum and titanium content. The compositional variations of all three alloys are given in Table 2.1 [16]. All three alloys are used in a solution-annealed condition with a minimum annealing temperature of 2100°F (1149°C).

Table 2.1. Limiting Chemical Compositions (%)

General Requirements			
UNS designation	**N08800**	**N08810**	**N08811**
INCOLOY alloys	**800**	**800H**	**800HT**
Nickel	30.0-35.0	30.0-35.0	30.0-35.0
Chromium	19.0-23.0	19.0-23.0	19.0-23.0
Iron	39.5 min	39.5 min	39.5 min
Carbon	0.10 max	0.05-0.10	0.06-0.10
Aluminum	0.15-0.60	0.15-0.60	0.25-0.60
Titanium	0.15-0.60	0.15-0.60	0.25-0.60
Aluminum+Titanium	0.30-1.20	0.30-1.20	0.85-1.20
ASTM grain size	Not specified	5 or coarser	5 or coarser

In view of the insignificant variation in chemical composition for Alloy 800, 800H and 800HT, all three alloys exhibit very similar physical and thermal properties. The physical properties of Alloy 800H are given in Table 2.2 [16, 46-56].

Table 2.2. Physical Properties of the Test Material

Physical Property	Temperature, °C	Metric Units
Density	Room	7.94 g/cm^3
Melting Point	1357-1385	---
Electrical Resistivity	21	0.989 μohm-m
Coefficient of Thermal Expansion	100	14.4 μm/m/°C
Modulus of Elasticity	20	196.5 GPa
Poisson's Ratio	20	0.339
Thermal Conductivity	21	11.5 W/m-K
Specific Heat	0-100	460 J/Kg°C
Curie Temperature	-115	---

Alloy 800H, tested in this program, was procured in the form of round bars from the Fry steel company in a heat-treated condition. The heat treatment involved annealing at 2200°F (1204°C) followed by rapid cooling, providing a fully austenitic microstructure. The chemical composition and the tensile properties of the as-received material, based on the vendor certification, are given in Tables 2.3 and 2.4, respectively. No additional thermal treatments were given to the test material prior to the machining of the desired specimens.

Table 2.3. Chemical Composition (wt %)

Element	Material/Heat Number
	Alloy 800H/HH6274AG
C	0.08
Mn	0.75
Fe	46.04
S	0.001
Si	0.24
Cu	0.26
Ni	31.99
Cr	19.67
Al	0.44
Ti	0.53
Al+Ti	0.97

Table 2.4. Ambient Temperature Tensile Properties

Yield Strength, ksi (MPa)	Ultimate Tensile Strength, ksi (MPa)	Percent Elongation	Percent Reduction in Area
30.7 (211.7)	88.6 (610.90)	58.6	64.2

2.2. Test Specimens

The heat-treated round bars were machined into smooth cylindrical specimens having 4-inch (101.6 mm) overall length, 1-inch (25.4 mm) gage length and 0.25-inch (6.35 mm) gage diameter such that the gage section was parallel to the longitudinal rolling direction. The ratio of the gage length to the gage diameter of these specimens was maintained at 4,

as prescribed by the ASTM designation E 08 (2004) [57]. The configuration and the dimensions of the smooth cylindrical specimen are shown in Figure 2.1. These specimens were used in both tensile testing and stress-corrosion-cracking (SCC) tests.

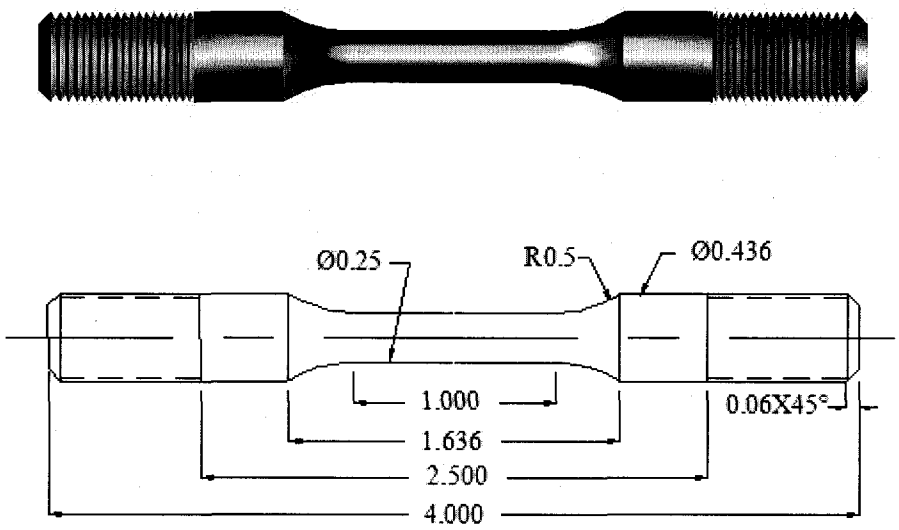

Figure 2.1. Smooth Cylindrical Specimen

The effect of stress concentration on both the room temperature tensile properties and SCC behavior of Alloy 800H was studied by introducing a circular notch at the center of the gage section having a diameter and root radius of 0.156-inch (3.96 mm) and 0.049-inch (1.245 mm), respectively, as shown in Figure 2.2. The stress concentration factor (K_t) corresponding to this notch was approximately 1.45 [58]. The magnitude of K_t was determined using equations 2.1, 2.2, and the plot shown in Figure 2.3 [59].

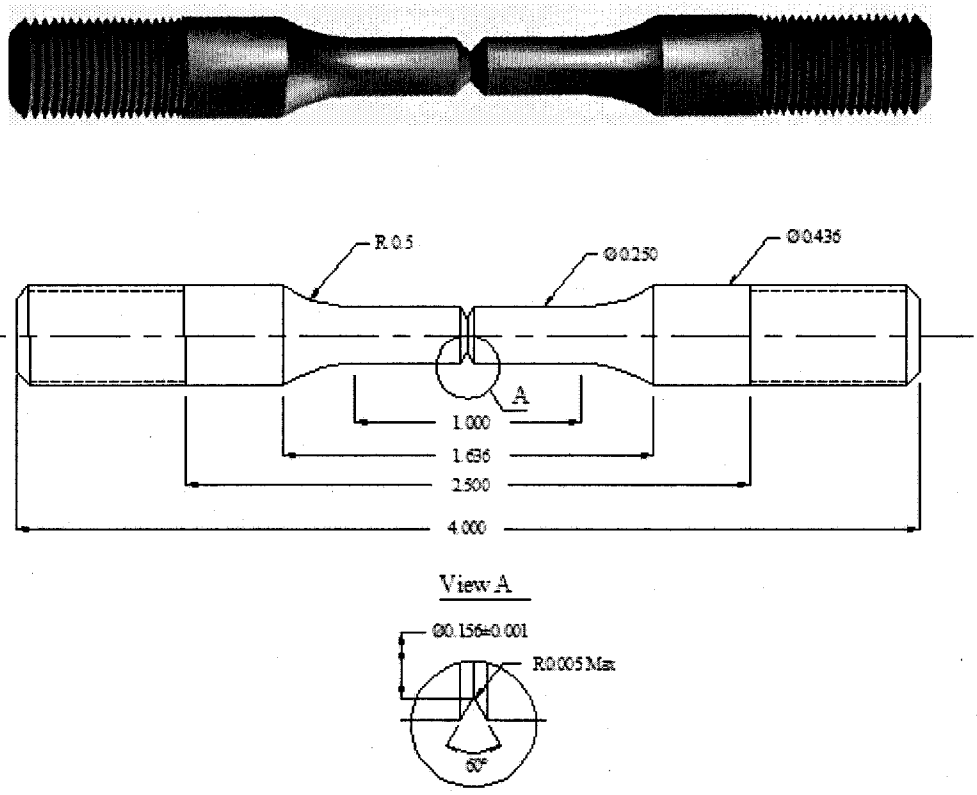

Figure 2.2. Notched Cylindrical Specimen

$$\frac{D}{d} = \frac{0.250\ in}{0.156\ in}$$

$$\frac{D}{d} = 1.60 \qquad \text{(Equation 2.1)}$$

$$\frac{r}{d} = \frac{0.0468\ in}{0.156\ in}$$

$$\frac{r}{d} = 0.30 \qquad \text{(Equation 2.2)}$$

Where,

D = gage diameter

d = notch diameter

r = radius of curvature at the root of the notch

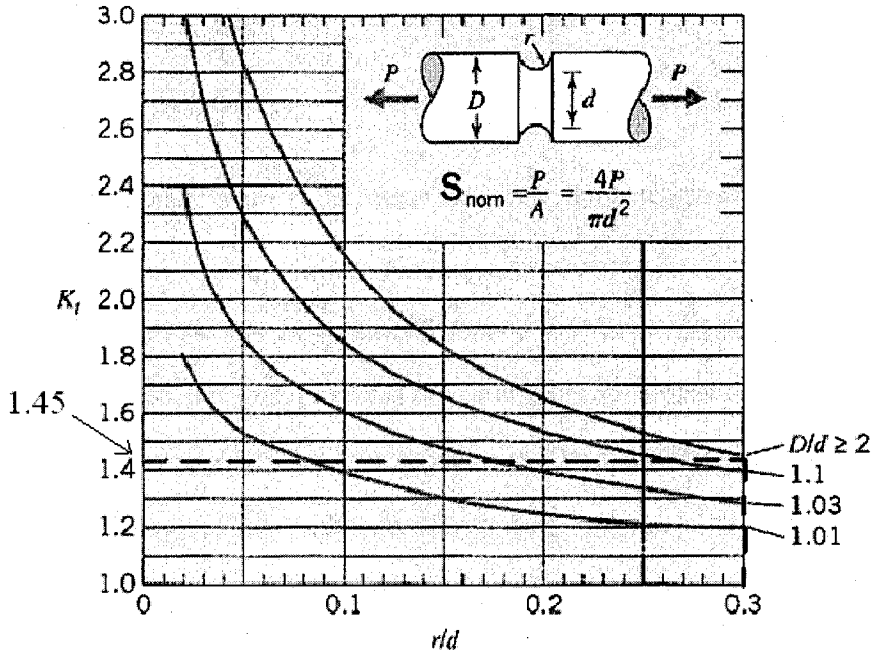

Figure 2.3. Stress Concentration Factors for Grooved Shafts [59]

A limited number of SCC test was also performed involving self-loaded specimens (C-ring and U-bend) contained in a corrosion-resistant C-276 vessel to evaluate crack initiation and growth on the outer and inner surfaces of these specimens in an aggressive environment. The configurations of both C-ring and U-bend specimens are shown in Figures 2.4 and 2.5, respectively. The C-ring and U-bend specimens were machined according to the ASTM designations G 38 (2001) [60] and G 30 (1997) [61], respectively, in such a way that the resultant tensile stress on the convex surface was parallel to the longitudinal rolling direction.

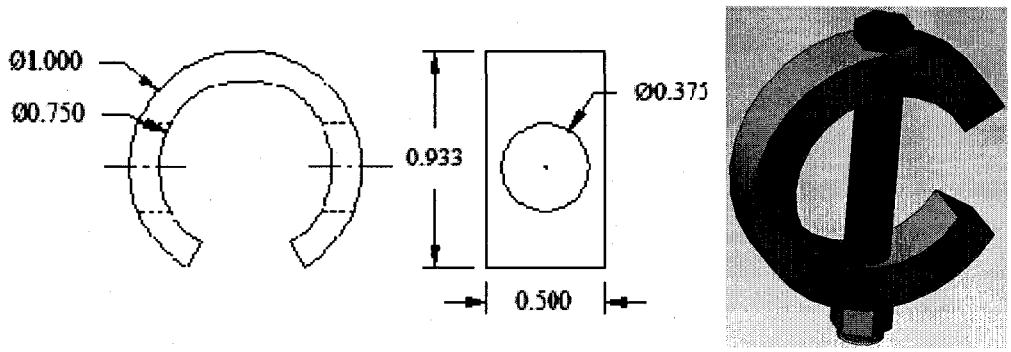

Figure 2.4. C-Ring Specimen

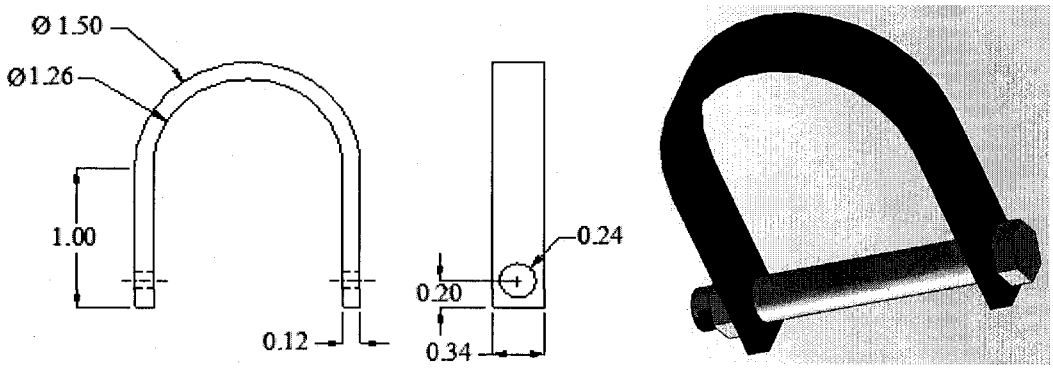

Figure 2.5. U-Bend Specimen

In order to study the localized corrosion behavior of Alloy 800H, small cylindrical specimens having 0.5-inch (12.7 mm) length and 0.375-inch (9.50 mm) diameter with a central hole of 0.3-inch (0.762 mm) diameter for holding the specimen were used. The specimens used in SCC testing under controlled potential (E_{cont}) were smooth cylindrical specimens having a conductive wire spot-welded close to their shoulder to enable the application of electrochemical potential using the slow-strain-rate (SSR) technique. The schematic views of the polarization and welded-tensile specimens are illustrated in Figures 2.6 and 2.7, respectively.

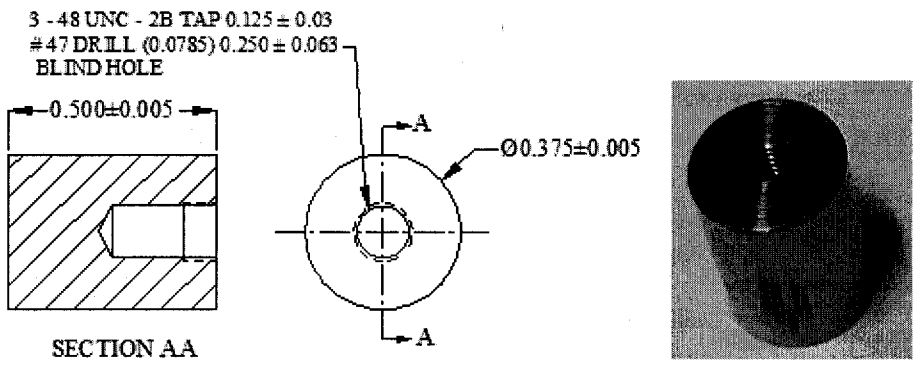

Figure 2.6. Polarization Specimen

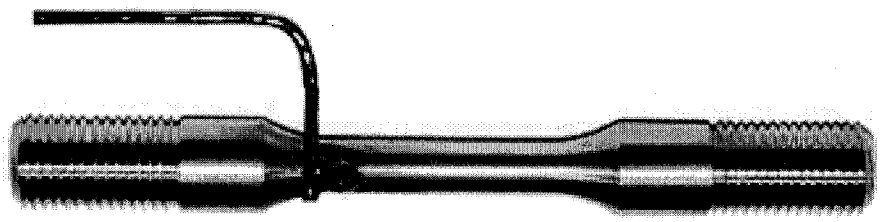

Figure 2.7. E_{cont} Specimen

2.3. Test Environment

As indicated earlier in this thesis, the structural materials for the heat exchangers will be exposed to hostile environments containing sulfuric acid (H_2SO_4) and hydrogen iodide (HI). Even though the H_2SO_4 decomposition is envisioned at temperatures in the vicinity of 950°C, SCC testing could not be accommodated at this temperature due to the limitation of infrastructure at Material Performance Laboratory. Rather, the SCC testing was performed at a maximum temperature of 90°C at constant-load and under SSR condition in the presence of an acidic aqueous solution. This acidic solution contained 10 gm/liter of sodium iodide, deionized water and H_2SO_4. The H_2SO_4 was added to achieve

the desired pH of approximately 1. For immersion testing using self-loaded specimens, an aqueous solution containing H_2SO_4 only was used. The pH of this acidic solution was also maintained at around 1.

CHAPTER 3

EXPERIMENTAL PROCEDURES

The structural materials to be used for hydrogen (H_2) generation through utilization of sulfuric acid (H_2SO_4) decomposition process must possess high tensile strength, sufficient resistance to plastic deformation and excellent corrosion resistance while exposed to the acidic environment at unusually high operating temperature. Since a maximum temperature of 950°C has been proposed for successful and efficient production of H_2 using the sulfur-iodine (S-I) cycle, efforts have been made in this investigation to determine the tensile properties of Alloy 800H in the temperature regime of ambient to 1000°C.

As to the determination of the cracking susceptibility of this alloy, stress-corrosion-cracking (SCC) tests has been performed under both constant-load (CL) and slow-strain-rate (SSR) condition in an acidic solution at temperatures up to 90°C. The localized corrosion (pitting and crevice) behavior of this alloy was also studied in an identical environment using an electrochemical method known as cyclic potentiodynamic polarization (CPP). The role of applied potential was also explored by applying anodic and cathodic controlled potentials (E_{cont}) to the test specimen while exposed to an identical environment under a strained condition. A limited number of immersion testing was also performed using C-ring and U-bend specimens to study the initiation and

growth of cracking on the specimen surface. Further, the optical microscopy (OM) and scanning electron microscopy (SEM) were used to analyze the metallurgical microstructure and morphology of failure of the tested specimens, respectively. The experimental procedures for different types of testing are presented in the next sub-sections.

3.1. Mechanical Properties Evaluation

The majority of the tensile testing was performed in a model 319.25 materials testing system (MTS) using both smooth and notched cylindrical specimens. The strain rate used in this testing was maintained at 10^{-3} sec^{-1} according to the ASTM designation E 08 (2004) [57]. This machine had a maximum axial load capability of 250 KN (55 kip) and a torsional load transducer with a maximum capacity of 2200 N-m (20,000 lbf-in). The test specimen was loaded using a heavy-duty load-frame connected to an adjustable crosshead on the upper part. A movable hydraulic actuator connected to a wedge grip enabled the fixing of the specimen. The test specimen fixed between the two wedge grips was pulled by this actuator. The crosshead movement enabled the application of load to the specimen.

The MTS unit containing the strain gauges, extensometer and temperature sensors were controlled by an 8-channel signal-conditioning box. The software interface managed all corresponding signals during testing. The test data were acquired at the rate of 100 points/sec. In order to accommodate tensile testing at elevated temperatures, the MTS unit contained a furnace with a ceramic-lined chamber that maintained a constant temperature during straining of the specimen. A thermocouple was used to measure the

temperature inside the chamber. A maximum temperature of 600°C was attained due to the utilization of this chamber, which was de-aerated by flowing nitrogen throughout the entire testing period to avoid contamination of the specimen surface. The time-temperature relationship for furnace calibration is given in Table 3.1. The MTS unit used in this investigation is illustrated in Figure 3.1.

Table 3.1. Calibration Data for the Furnace

Target temperature (°C)	Chamber set point temperature (°C)	Time to reach target temperature (min)
100	143	60
200	253	60
300	363	60
400	467	55
500	563	50
600	658	50

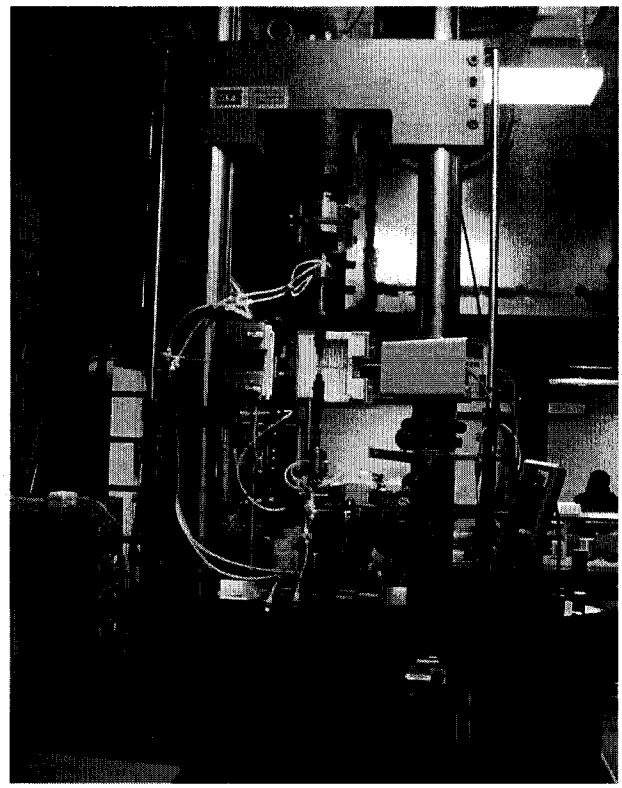

Figure 3.1. MTS Test Setup (Model 319.25)

The tensile properties including yield strength (YS), ultimate tensile strength (UTS), percent elongation (%El) and percent reduction in area (%RA) were determined using the engineering stress versus strain (s-e) diagram, and the specimen dimensions (before and after testing) as a function of the testing temperature. The magnitude of YS was determined by drawing a line parallel to the linear portion of the s-e diagram at an offset value corresponding to 0.2% strain. The magnitude of %El and %RA were determined according to the equations 3.1 through 3.4 given below. A minimum of two tests were performed to ensure the accuracy of the data and to determine an average value of each tensile parameter. Testing was also performed in newly installed model 8862 Instron equipment (Figure 3.2) to verify the results obtained from the MTS unit. The Instron

equipment was capable of evaluating the tensile properties of the test material at temperatures above 1000°C. However, the load capacity to this unit was significantly less compared to that of the MTS unit (100 versus 250 KN).

$$\% \text{ El} = \left(\frac{L_f - L_i}{L_i} \right) \times 100 \qquad L_f > L_i \qquad (3.1)$$

$$\%\text{RA} = \left(\frac{A_i - A_f}{A_i} \right) \times 100 \qquad A_i > A_f \qquad (3.2)$$

$$A_i = \left(\frac{\pi \times D_i^2}{4} \right) \qquad (3.3)$$

$$A_f = \left(\frac{\pi \times D_f^2}{4} \right) \qquad (3.4)$$

Where,

A_i = Initial cross-sectional area of the gage section

A_f = Cross-sectional area of the gage section at Failure

L_i = Initial gage length

L_f = Final gage length

D_i = Initial gage diameter

D_f = Final gage diameter

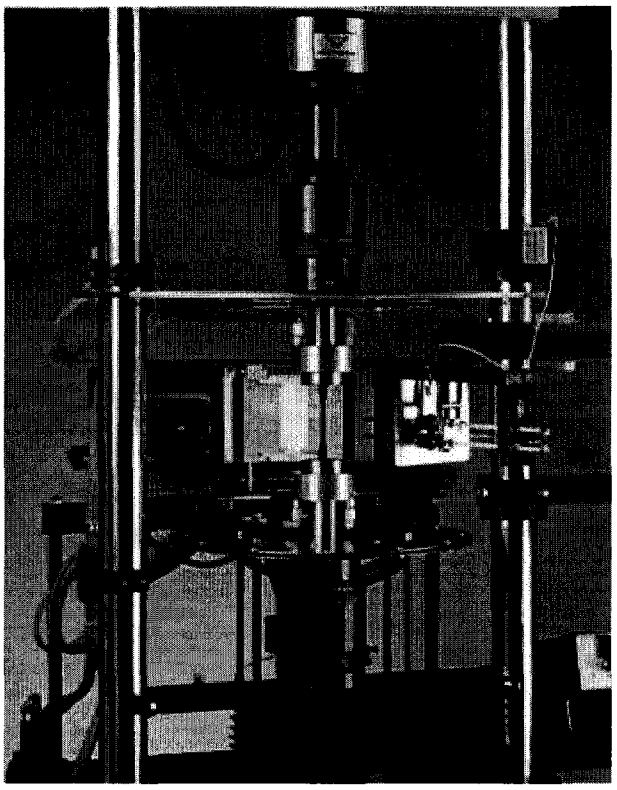

Figure 3.2. Instron Test Setup (Model 8862)

3.2. Stress-Corrosion-Cracking Evaluation

3.2.1. Constant-Load Testing

The susceptibility of Alloy 800H to SCC at CL was determined using smooth cylindrical specimens according to the National Association of Corrosion Engineers (NACE) standard TM-01-77 [62]. A calibrated proof ring was used to load the test specimens at the desired load levels. A calibration curve (load versus deflection) for each proof ring was provided by the manufacturer, which is shown in Figure 3.3. The specimen was loaded inside a test chamber made of highly corrosion-resistant Alloy C-276 that contained the simulated test solution. For elevated temperature testing, heating cartridges were inserted at the bottom cover of the chamber to achieve the desired

temperature. Further, a condenser was placed on the top lid of the test chamber to prevent any loss of liquid resulting from evaporation of the test solution at elevated temperatures. The setup used in CL testing is illustrated in Figure 3.4.

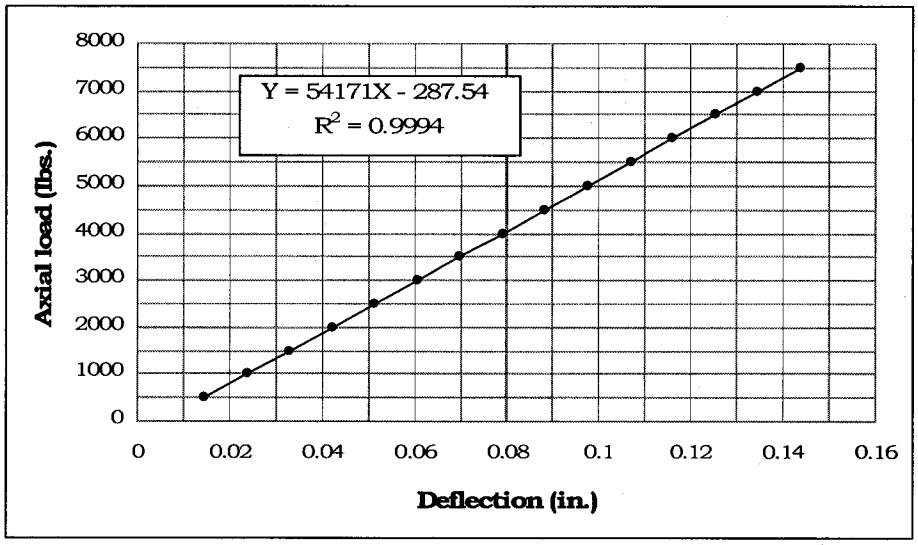

Figure 3.3. Proof Ring Calibration Curve

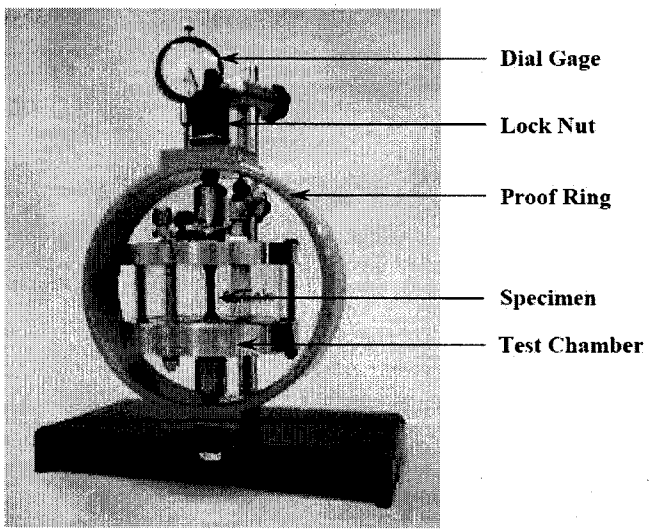

Figure 3.4. Constant-Load Test Setup

The magnitude of the applied stress was based on the room temperature YS of the test material. The specimen was loaded at stress values corresponding to different percentages of the material's YS value, and the corresponding time-to-failure (TTF) was recorded. The CL testing was performed for a maximum duration of 720 hours. A timer attached to the inner top surface of the proof ring was used to record the TTF. The cracking susceptibility of Alloy 800H using this technique was determined in terms of a threshold stress (σ_{th}), below which no failure occurred in 720 hours [63].

3.2.2. Slow-Strain-Rate Testing

SSR testing, also known as constant extension rate testing (CERT), consisted of pulling a cylindrical specimen at a constant strain rate according to the ASTM designation G 129 [64]. During conventional tensile testing, a specimen is subjected to plastic deformation at relatively high strain rate, causing its failure. A similar accelerated rate of straining cannot be used in SCC evaluation, since the environment could not contribute to the cracking process due to fast failure resulting from the application of high strain rate. On a similar logic, a specimen cannot be strained at an unusually slower strain rate since the mechanical load would exert no significant contribution to cause failure while the specimen is exposed to a deleterious environment. In such case, the specimen would simply degrade due to the environmental interaction with the test material. Thus, in order to achieve a maximum contribution from both the mechanical and environmental parameters simultaneously, one has to optimize both effects [65]. In view of this rationale, a strain rate of 3.3×10^{-6} sec^{-1} was used in this investigation to maximize the role of both the testing environment and the applied load. During SSR testing, the

selection of this strain rate was based on prior research results obtained at the Lawrence Livermore National Laboratory [66-68].

The SSR test setup, shown in Figure 3.5, consisted of a top-loaded actuator with a maximum loading capacity of 7500 lbs. The top-loaded actuator was used to prevent any damage to it resulting from the spilled solution during straining of the specimen. A hand-wheel located at the bottom end of the test frame was used to preload the test specimen. A linear-voltage-displacement-transducer (LVDT) was used to measure the displacement of the gage section during straining. For elevated temperature testing, heating cartridges were inserted onto the bottom lid of the test chamber. A thermocouple was used to measure the temperature inside the test chamber.

The computer interface recorded the load values and the corresponding displacement of the LVDT using the four-frame software. The load frames were subjected to load compliance test prior to the actual testing to determine the load-frame-compliance-factor (LFCF-error function). This test was conducted using threaded specimens made of ferritic Type 430 stainless steel. The LFCF graphs for the three load frames used in this investigation were obtained during the load compliance test, which are shown in Figure 3.6. The cracking susceptibility of the test specimen under the SSR condition could not be expressed in terms of σ_{th} for a specific environment, since the magnitude of the stress was gradually changed due to the reduction in its gage diameter, while being strained at a constant rate. Instead, the cracking tendency of the test material was characterized by the TTF, %El, %RA and true failure stress (σ_f).

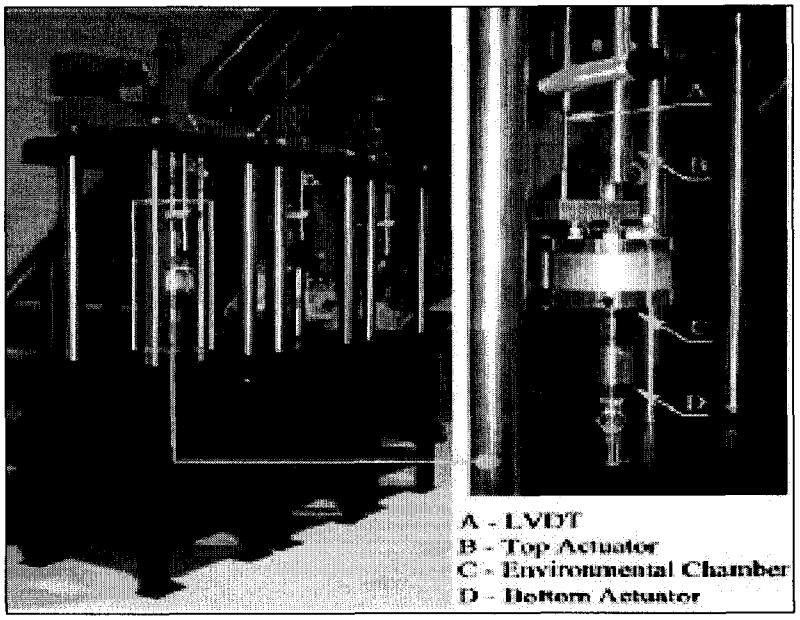

Figure 3.5. Slow-Strain-Rate Test Setup

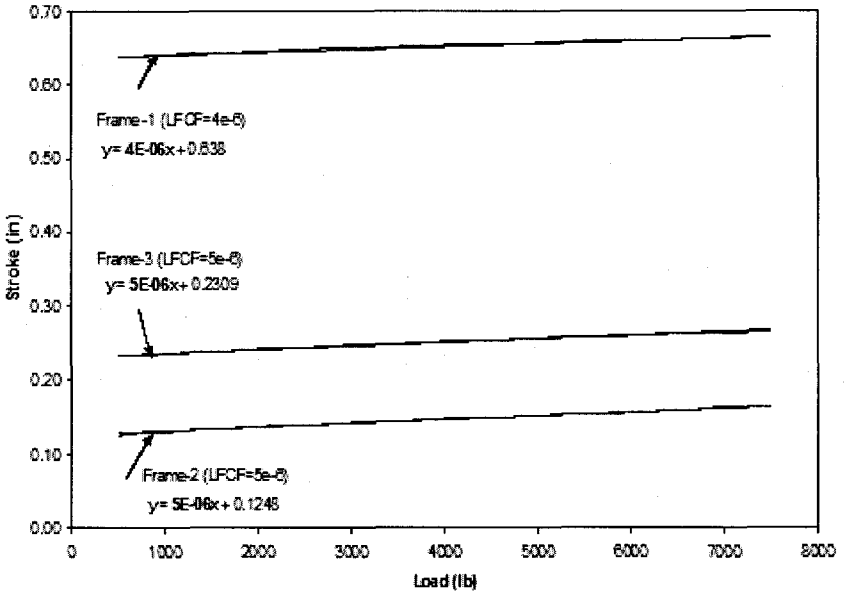

Figure 3.6. Load Frame Compliance Test Graphs

3.3. Electrochemical Testing

Electrochemical factors can significantly influence the degradations experienced by structural materials while exposed to an aggressive electrolyte. Under an equilibrium condition, the rate of anodic reaction is balanced by the rate of cathodic reaction. The potential at which this equilibrium occurs is known as corrosion or open-circuit potential (E_{corr}). However, such condition may be difficult to achieve in real life due to the interaction of many external environmental factors. For example, the equilibrium condition may be disturbed by the application of an external potential or current resulting from environmental conditions existing during the operation of a structure/component. This deviation from the equilibrium to a non-equilibrium condition is commonly referred to as polarization. Thus, the polarization experiments of Alloy 800H by an electrochemical technique can provide significant information as to its corrosion rate, cracking susceptibility and the degradation mechanism as a function of different metallurgical and environmental variables.

The difference in potential resulting from polarization is commonly measured by an over voltage (η), which is a measure of the polarized potential (E_p) with respect to the E_{corr}. The magnitude of η can be either positive or negative depending on the applied electrochemical potential during the polarization experiment, and can be given by the following equation.

$$\eta = E_p - E_{corr} \qquad (3.5)$$

Polarization can be performed either potentiodynamically or galvanostatically. The basic difference lies in applying potential or current at a specified rate and recording the resultant current and potential, respectively. Alloy 800H was polarized in this investigation using a technique known as CPP. During CPP testing, the test specimen was polarized cathodically and anodically using a three-electrode technique. This technique involved the use of Alloy 800H as working electrode, two graphite rods as counter electrodes and silver/silver chloride (Ag/AgCl) contained inside a Luggin probe as reference electrode. The CPP testing was performed using a Gamry potentiostat, which was calibrated according to the ASTM designation G 05 [69]. This calibration experiment consisted of potentiodynamic polarization of Type 430 ferritic stainless steel in a 1N H_2SO_4 solution at 30°C, and a scan rate of 0.17 mV/sec. A standard calibration curve taken from the ASTM designation G 05 is illustrated in Figure 3.7 [69]. If the potentiodynamic polarization diagram developed prior to the experimental work using this calibration technique matched the shape of the standard curve, the potentiostat was deemed to be performing accurately. During polarization experiment, the tip of the Luggin probe was placed within 2-3 mm of the cylindrical test specimen, as shown in Figure 3.8. An initial delay of 30 minutes was given prior to the performance of the CPP testing to achieve a stable E_{corr} value. The experimental setup used in the CPP testing is illustrated in Figure 3.9.

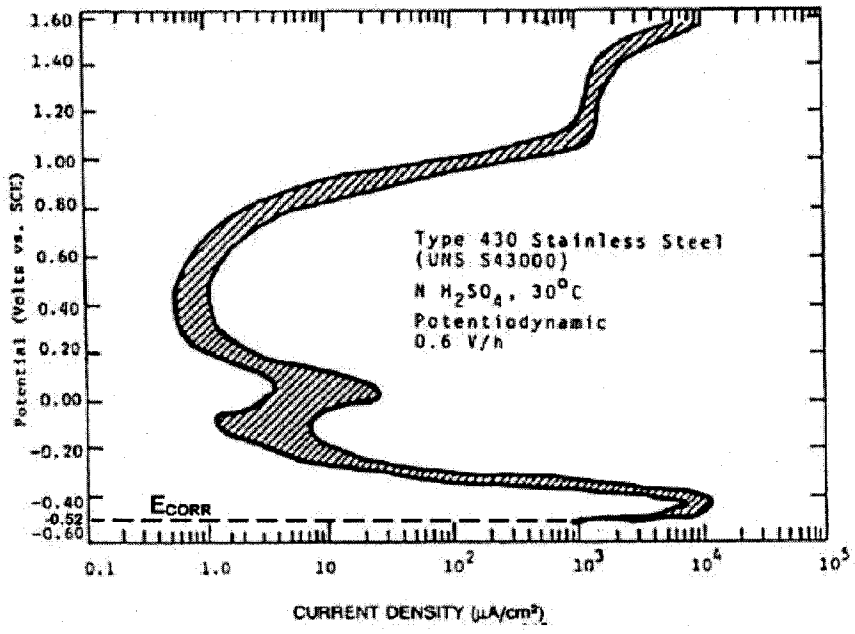

Figure 3.7. ASTM G 05 Standard Calibration Curve

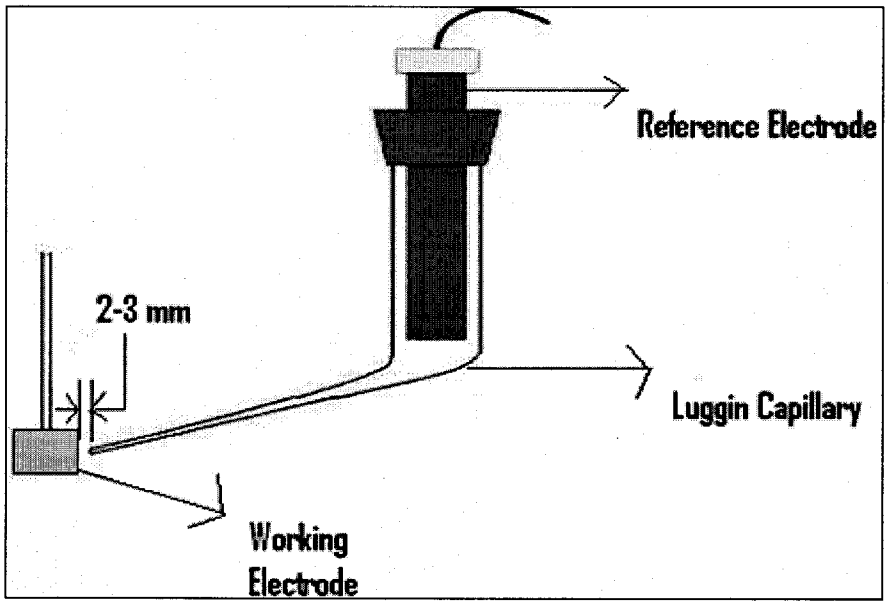

Figure 3.8. Luggin Probe Arrangement

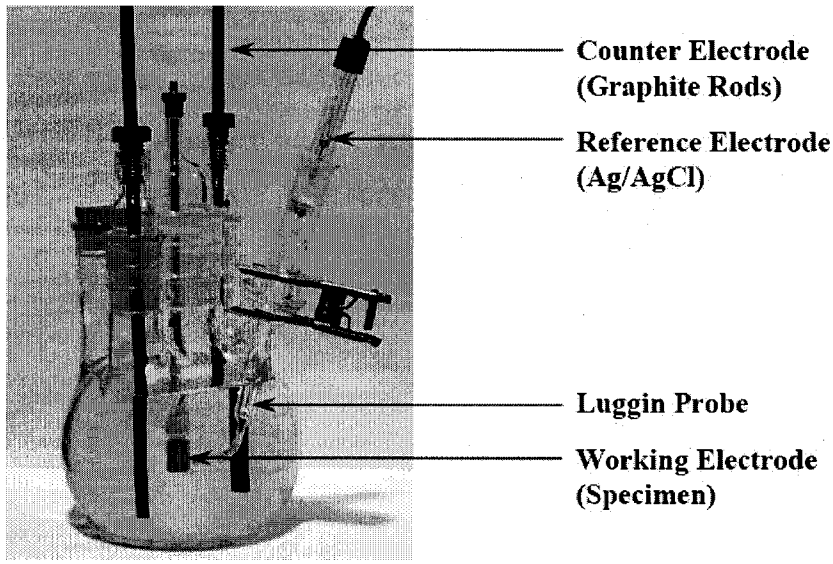

Figure 3.9. Cyclic Potentiodynamic Polarization Test Setup

3.4. SCC Testing under Applied Potential

It has been well established that the application of an external potential or current can influence the cracking susceptibility of a structural material while subjected to the simultaneous effect of applied load and a hostile environment. In view of this rationale, efforts were made to explore the role of either anodic or a cathodic applied potential on the cracking susceptibility of Alloy 800H when tested in an identical solution under an SSR condition. For SCC testing under an anodic E_{cont}, the magnitude of E_{pit} was taken into consideration to select the E_{cont} value. On the other hand, the magnitude of the cathodic E_{cont} was based on the E_{corr} value. The rationalization for the selection of the E_{cont} value was based on the electrochemical principles related to either anodic dissolution or formation of atomic H_2 during cathodic reaction in the presence of an aqueous solution.

As mentioned earlier, the smooth cylindrical specimen was spot-welded with a conductive wire to apply potential to its gage section, which was subsequently coated with a lacquer to prevent its direct contact with the test solution. The application of E_{cont} was achieved through use of three-electrode polarization technique described earlier. The resultant data during this potentiostatic polarization was recorded in terms of current versus time. The cracking susceptibility was once again determined in terms of ductility parameters (%El and %RA), σ_f and TTF in a similar manner as in conventional SSR testing. The experimental setup used in SSR testing under E_{cont} is illustrated in Figure 3.10.

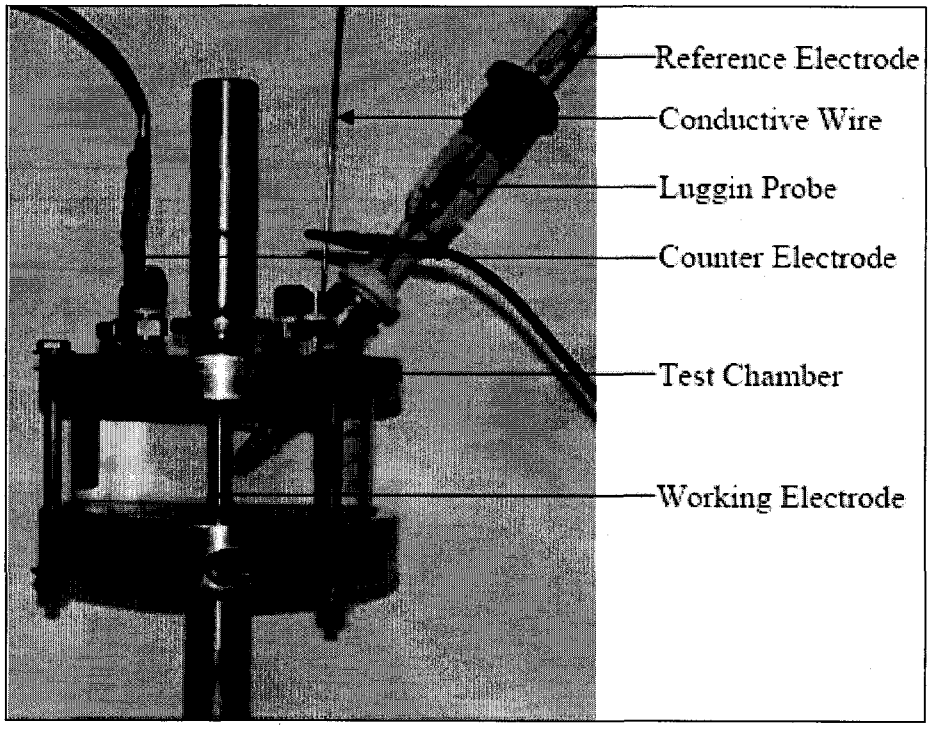

Figure 3.10. Controlled Potential Test Setup

3.5. SCC testing with self-loaded specimens

C-ring specimens of Alloy 800H were tested using Alloy C-276 chamber in a 90°C aqueous solution (H_2SO_4 only) to evaluate the effect of circumferential stress on the cracking susceptibility as a function of different test durations (7, 14, 21, 35, and 58 days). Limited number of testing was performed on U-bend specimens for time periods of 7 and 14 days. The C-ring specimens were loaded at a stress corresponding to 98% of the material's room temperature YS value according to the ASTM designations G 38 and 30, respectively [60, 61]. The displacement (Δ) of the outer diameter of the C-ring specimen was determined using the equation 3.6. A correction factor (Z) for curved beam was determined from Figure 3.11 based on the ratio of the mean diameter to the wall thickness of the C-ring specimen. The C-ring specimens were visually examined for the initiation of cracking at the convex surface, which is expected to undergo sustained tensile loading. The test setup used is shown in Figure 3.12.

$$OD_f = OD - \Delta \qquad (3.6)$$

and,

$$\Delta = \frac{f\pi D^2}{4EtZ}$$

Where,

OD = outside diameter of C-ring before stressing

OD_f = outside diameter of stressed C-ring

f = desired stress, psi (98% of YS value)

Δ = change of OD giving desired stress

D = mean diameter (OD-t)

t = wall thickness

E = modulus of elasticity

Z = a correction factor for curved beams

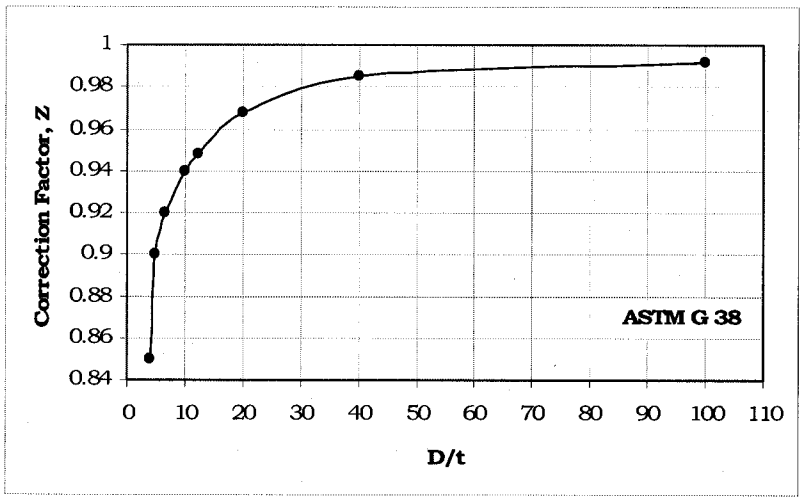

Figure 3.11. Correction Factor for Curved Beams

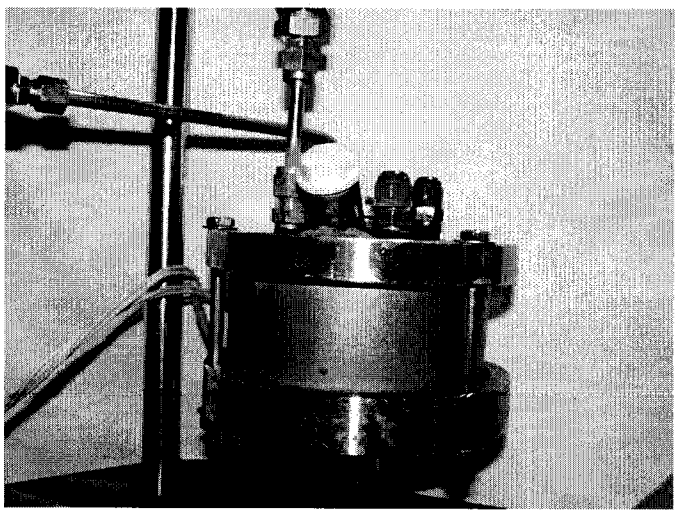

Figure 3.12. Immersion Test Setup

3.6. Microstructural Evaluation

An inverted OM, with a maximum resolution of 1000X was used to characterize the metallurgical microstructure of Alloy 800H. The metallographic evaluation was based on the impingement of high-energy light rays onto the specimen surface and transmitting them through a number of condensing lenses and shutters into a half-penetrating mirror. This technique enables the transmitted light to pass through an objective lens that forms a primary image, which is magnified through the eyepiece. A digital camera with a resolution of 1 mega pixel enabled the capture of image on a computer screen through utilization of special software. The different components of the microscopic evaluation setup are shown in Figure 3.13.

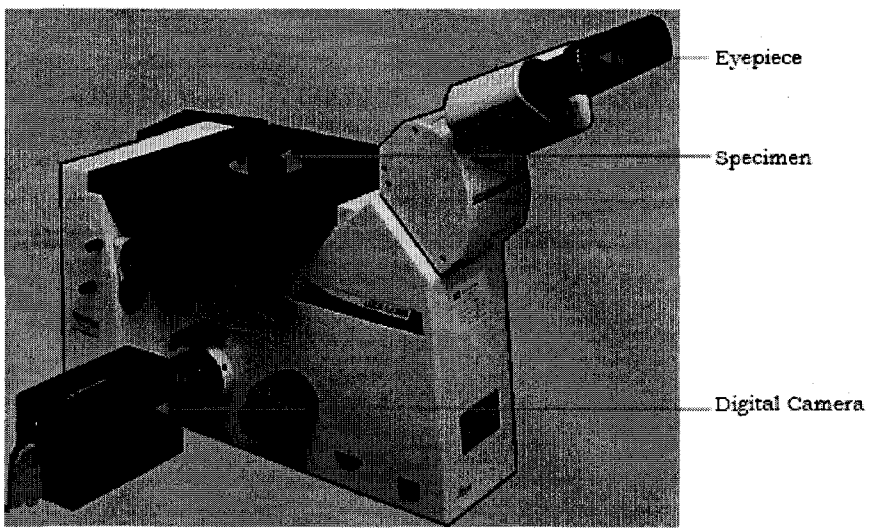

Figure 3.13. Inverted Optical Microscope

The test specimen was mounted in an epoxy resin followed by polishing and etching as shown in Figure 3.14 according to the conventional metallographic technique. The

chemical composition of the etchant used for microstructural evaluation consisted of 15 ml of hydrochloric acid, 10 ml of acetic acid and 10 ml of nitric acid [70].

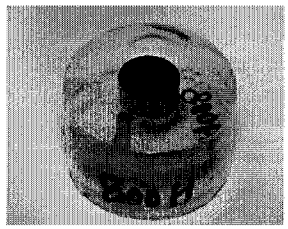

Figure 3.14. Test Sample for OM

3.7. Fractographic Evaluation

The extent and morphology of failure at the primary fracture surface of the cylindrical specimens used in both tensile and corrosion testing were determined using a JEOL model 5600 SEM (Figure 3.15) having a maximum magnification of up to 100,000X and a resolution of up to 50 nm. During SEM study, electrons from a metal filament are collected and focused, similar to light waves, into a narrow beam. This beam can then scan across the subject, synchronized with a spot on a computer screen. The electrons scattered from the subject are detected creating a current that can make the spot on the computer brighter or darker. This creates a photograph-like image with an exceptional depth of field. Magnifications of several thousand can be achieved by SEM. Normally SEM provides black and white micrographs. The sectioned cylindrical specimens, cut to specified lengths, were placed on a sample holder to accommodate multiple specimens for fractographic evaluations.

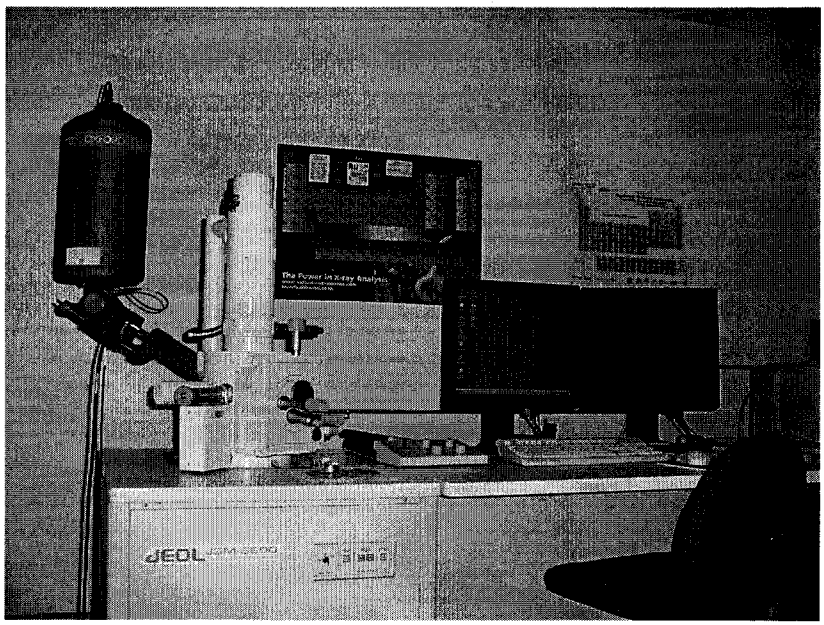

Figure 3.15. Scanning Electron Microscopy

CHAPTER 4

RESULTS

This section presents the tensile properties of Alloy 800H at different temperature using smooth cylindrical specimens. Tensile properties at ambient temperature using notched cylindrical specimens are also included. The results of stress-corrosion-cracking (SCC) testing using different state-of-the-art experimental techniques are also provided. The results of general and localized studies are also presented. Further, the metallographic and fractographic evaluations using optical microscopy (OM) and scanning electron microscopy (SEM), respectively, are included. The test results obtained from the specific types of testing are discussed in the following subsections.

4.1. Metallographic Evaluations

The metallurgical microstructures of the cylindrical specimens of Alloy 800H in the as-received and tested conditions are illustrated in Figures 4.1, and 4.2, respectively. An examination of the microstructure shown in Figure 4.1 revealed classical austenitic grains and annealing twins resulting from solution annealing, which are common in alloys containing nickel [71, 72]. The optical micrograph involving a specimen used in SSR testing, shown in Figure 4.2, revealed a similar microstructural feature except for the fact that the grains were oriented in the direction of the applied stress. The elemental analysis by energy dispersive spectroscopy showed the presence of precipitates consisting of

titanium nitrides, titanium carbides and chromium carbides, which are consistent with the open literature [16].

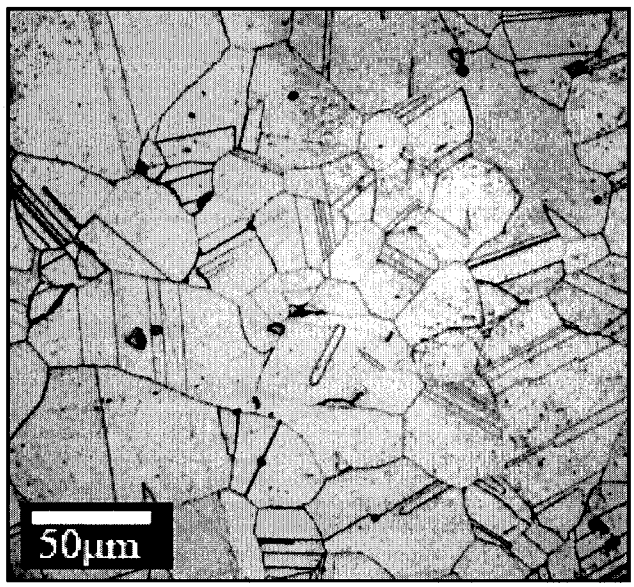

Figure 4.1. Optical Micrograph, Etched, 200X

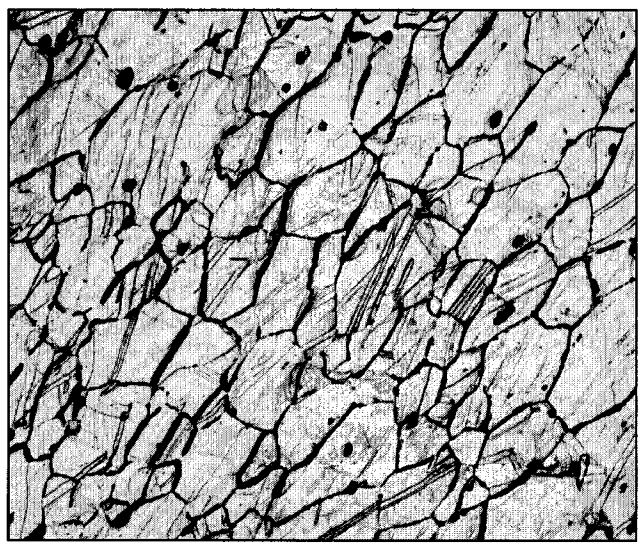

Figure 4.2. Optical Micrograph after Testing, Etched, 100X

4.2. Tensile Properties Evaluations

The results of tensile testing involving smooth cylindrical specimens of Alloy 800H are shown in Figure 4.3 in the form of engineering stress versus strain (s-e) diagrams at different temperature (ambient to 1000°C). The s-e diagrams were superimposed to compare the tensile behavior of this alloy as a function of the testing temperature. In general, the magnitudes of the yield strength (YS) and ultimate tensile strength (UTS) were gradually reduced with increasing temperature, as expected. The average values of different tensile parameters including YS, UTS, percent elongation (%El) and percent reduction in area (%RA) derived from the s-e diagrams and the specimen dimensions before and after testing are given in Table 4.1.

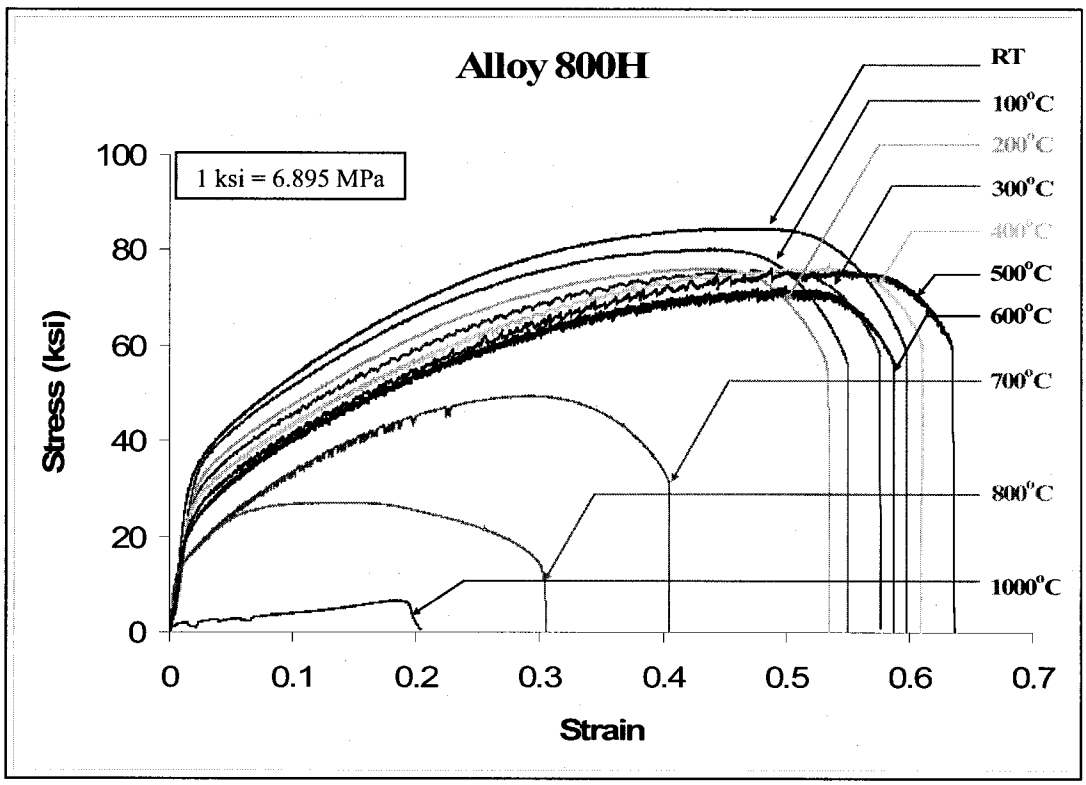

Figure 4.3. s-e Diagrams vs. Temperature

Table 4.1. Tensile Properties vs. Temperature (Smooth Specimen)

Temperature, °C	YS, ksi	UTS, ksi	%El	%RA
Ambient	37.8	86.2	58.5	67.5
100	35.6	78.8	53.9	66.3
200	33.1	75.8	52.6	64.0
300	30.9	76.8	55.0	61.2
400	27.5	76.5	60.2	58.9
500	24.6	76.3	60.4	57.5
600	21.9	71.9	57.6	62.0
700	14.9	49.6	39.1	61.6
800	14.6	26.7	31.4	60.3
1000	1.1	6.6	21.0	10.0

The variations of YS and UTS with temperature are illustrated in Figures 4.4 and 4.5, respectively. The reduced values of YS and UTS with increasing temperature were due to the enhanced plasticity at elevated temperatures. These data also reveal that Alloy 800H was capable of maintaining relatively high tensile strength even at elevated temperatures. These results suggest that Alloy 800H may provide significant structural strength at temperatures up to 600°C, followed by a drop in YS and UTS at temperatures approaching 1000°C, which is the operating temperature for sulfuric acid (H_2SO_4) decomposition by the sulfur-iodine (S-I) process. It is interesting to note that the magnitude of UTS was drastically reduced between 600 and 1000°C.

An examination of the s-e diagrams shown in Figure 4.3 reveals that the failure strain (e_f) was gradually reduced between ambient temperature and 200°C, followed by its enhancement at temperatures up to 500°C. However, beyond 500°C, the magnitude of e_f was once again reduced. For some engineering alloys, such reduction in e_f has been

attributed to a phenomenon known as dynamic strain aging (DSA) that occurs due to the diffusion of solute elements such as carbon and nitrogen into the metal matrix, thus inhibiting the movement of dislocations past grain boundaries at some critical temperature. Beyond this critical temperature, the material can undergo enhanced plastic deformation, showing increased e_f values. While no efforts have yet been made to analyze defects in Alloy 800H, it is possible that the reduced e_f values may be the results of DSA at relatively lower temperatures (up to 200°C). This phenomenon is also illustrated in Figure 4.6, showing reduced %El up to 200°C. As to the ductility in terms of %RA, its value was also gradually reduced up to 500°C, followed by some enhancement of this parameter as shown in Figure 4.7.

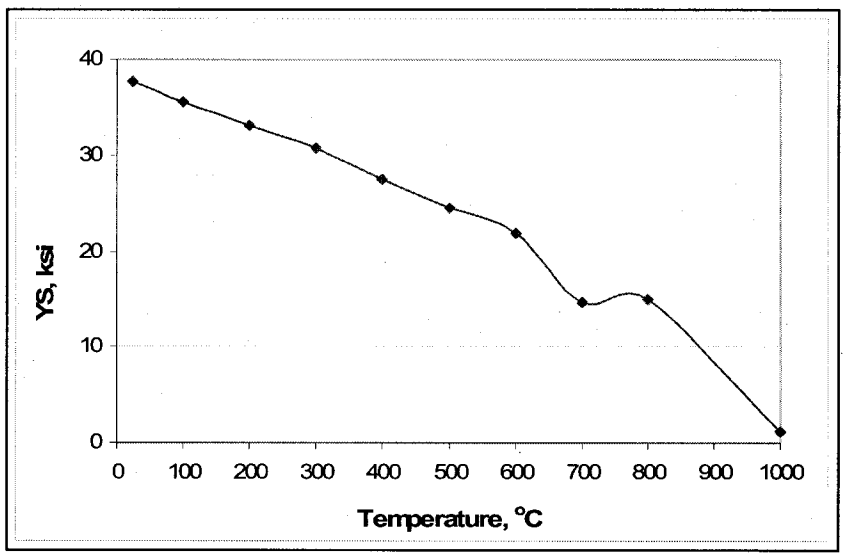

Figure 4.4. Variation of YS vs. Temperature

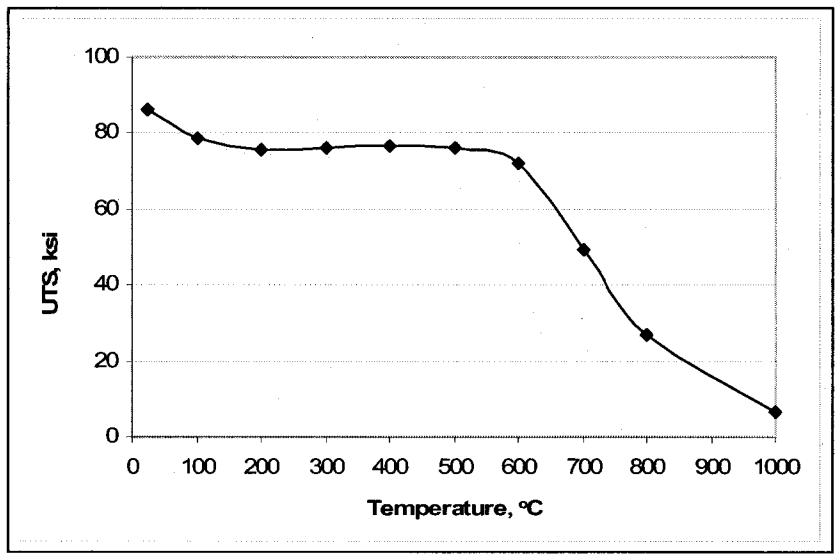

Figure 4.5. Variation of UTS vs. Temperature

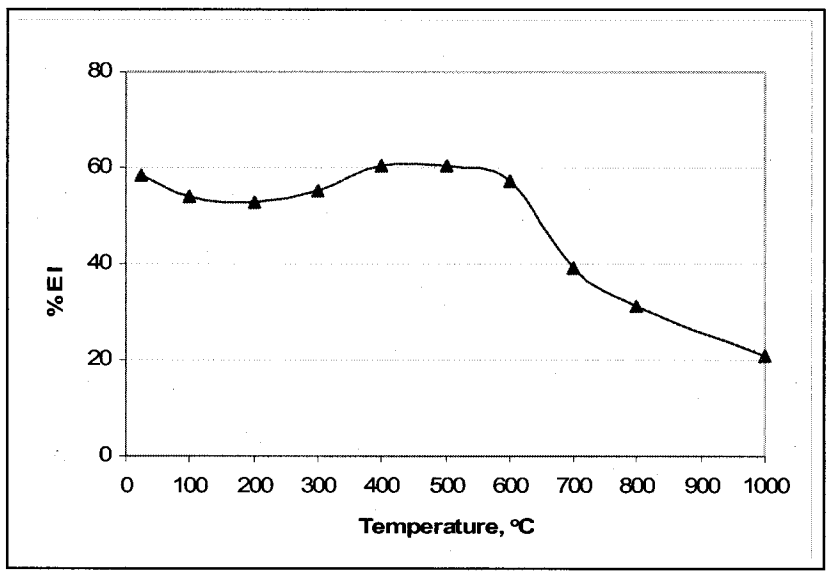

Figure 4.6. Variation of %El vs. Temperature

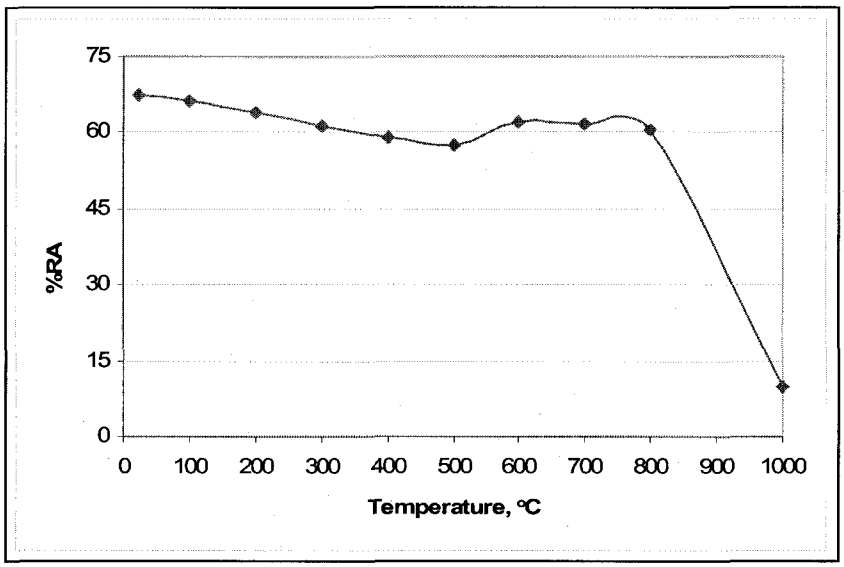

Figure 4.7. Variation of %RA vs. Temperature

The effect of stress concentration (K_t) on the tensile properties of Alloy 800H was determined by conducting tensile testing of notched cylindrical specimen at ambient temperature. The K_t of the notched specimen was approximately 1.45, as indicated in Chapter 2. A comparison of the tensile properties using smooth and notched specimen is shown in Table 4.2. The s-e diagrams obtained by using smooth and notched cylindrical specimens are illustrated in Figure 4.8. As expected, the notched specimens showed higher strength resulting from K_t due to the triaxial stress condition at the root of the notch. However, its ductility in terms of e_f, %El and %RA was significantly reduced compared to the smooth specimen, as shown in Figure 4.8 and Table 4.2, respectively. A similar behavior on the effect of stress raiser has been cited elsewhere [15, 73-74].

Table 4.2. Tensile Properties of Smooth vs. Notched Specimen at RT

Specimen	YS, ksi	UTS, ksi	%El	%RA
Smooth	37.8	86.2	58.5	67.5
Notch	73.9	125.3	10.1	22.0

RT: Room Temperature

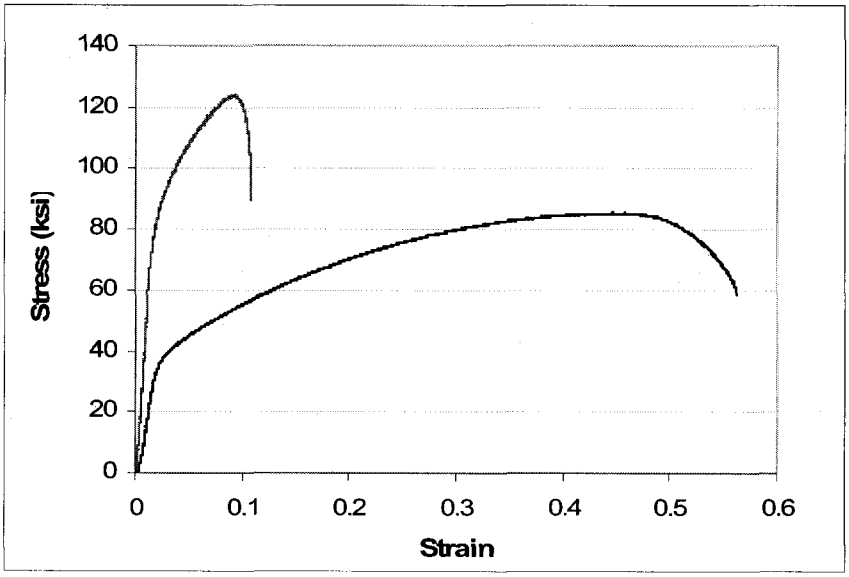

Figure 4.8. Comparison of s-e Diagrams at RT (Smooth vs. Notched)

4.3. SCC Testing under Constant-Load

The results of SCC testing at constant-load (CL) involving smooth cylindrical specimens of Alloy 800H in an aqueous solution containing H_2SO_4 and sodium iodide at ambient temperature and 90°C are shown in Table 4.3. These results indicate that Alloy 800H did not exhibit any failure even at an applied stress corresponding to 98% of the material's room temperature YS value while exposed to the testing solution. Thus, the magnitude of the threshold stress (σ_{th}) for cracking in this environment may lie in the

vicinity of 98% of the YS value of Alloy 800H. Since no failure was observed based on repeated testing at this applied stress level, no additional SCC tests were performed.

Table 4.3. Constant-Load SCC Test Results

Environment/ Temperature (°C)	% Yield Stress/ Load Applied (lbs)	Time-to-Failure
Acidic / RT	98/1818.4	NF
Acidic / 90°C	98/1818.4	NF

RT: Room Temperature, NF: No Failure, Acidic: H_2SO_4 + NaI +H_2O

4.4. SCC Testing under SSR condition

The results of SCC tests involving smooth and notched cylindrical specimens of Alloy 800H using the slow-strain-rate (SSR) technique are shown in Figures 4.9 and 4.10, respectively in the form of s-e diagrams, superimposed as a function of the testing temperature. The s-e diagrams obtained in air are also included in these figures for comparison purpose. Table 4.4 shows the magnitude of %El, %RA, time-to-failure (TTF) and true failure stress (σ_f) determined from the s-e diagrams shown in Figure 4.9 and the dimensions of the smooth specimens before and after testing. An evaluation of these data indicates that Alloy 800H exhibited significant resistance to SCC in terms of %El, %RA and TTF, showing very little changes in these parameters even under the combined effect of applied stress and the testing environment. It is, however, interesting to note that the magnitude of σ_f was reduced at 90°C in the presence of the acidic solution. The reduced σ_f at 90°C may be attributed to the reduction in load-bearing capability of Alloy 800H

resulting from the synergistic effect of the applied stress, acidic species and temperature. It is well-known that the protective film on the metal surface may be damaged at elevated temperature due to its reduced adherence to the metal substrate. The detrimental effect of aggressive chemical species at elevated temperatures under different loading conditions has been reported by other investigators [75, 76].

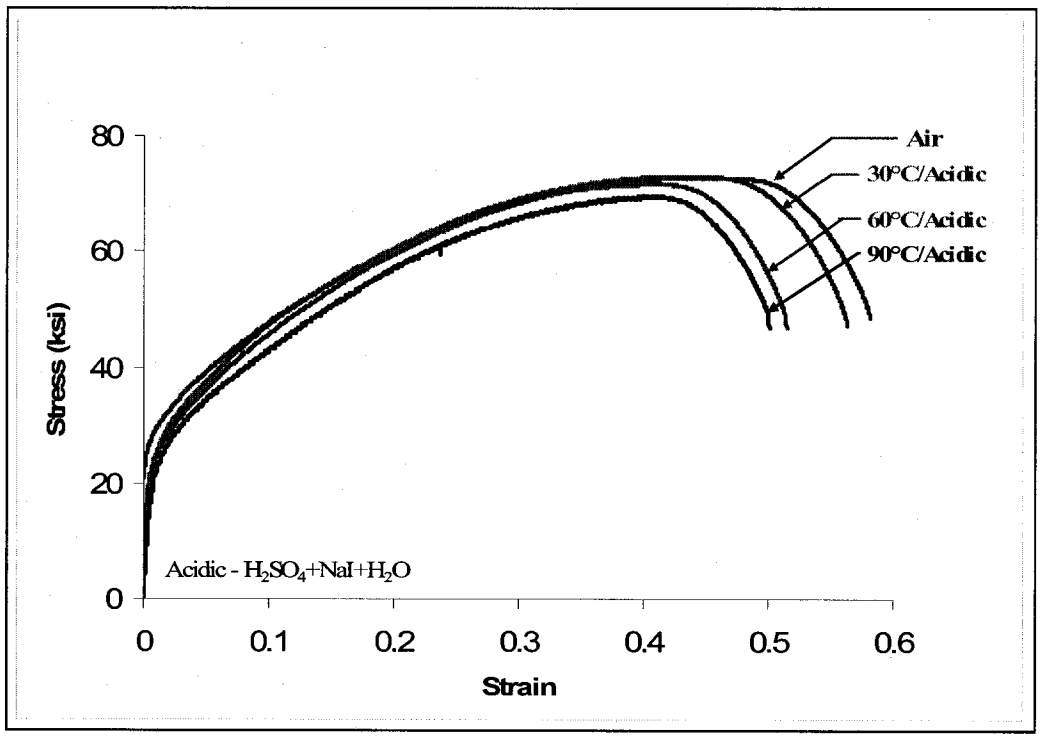

Figure 4.9. s-e Diagrams using Smooth Specimens in SSR Testing

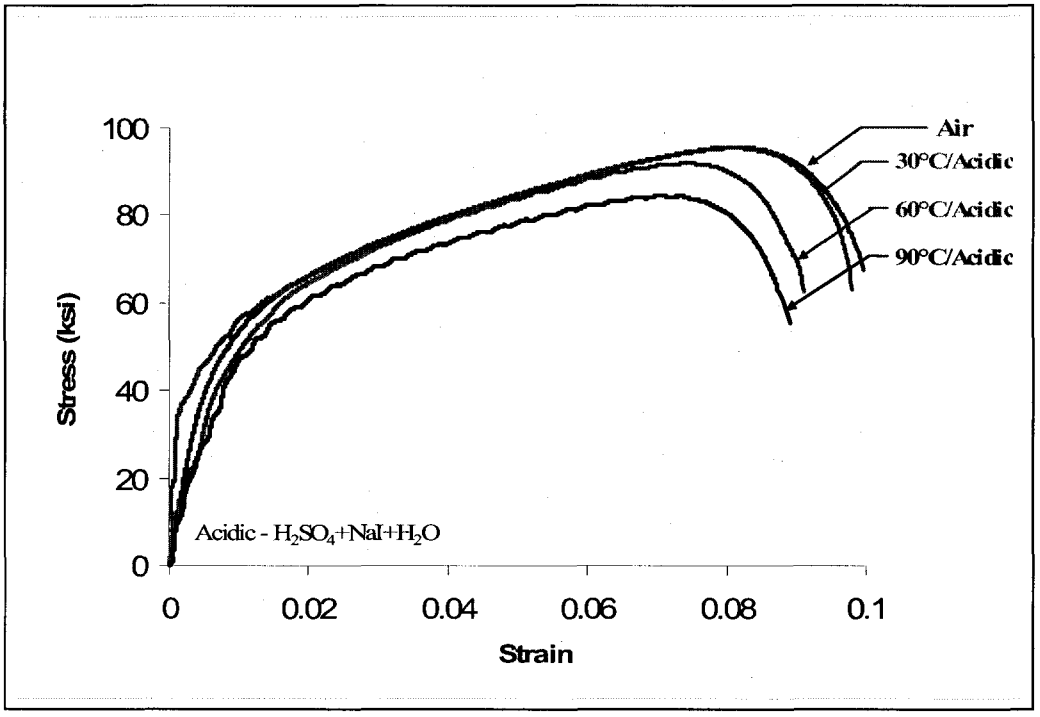

Figure 4.10. s-e Diagrams using Notched Specimens in SSR Testing

Table 4.4. SSR Test Results using Smooth Specimens

Environment / Temperature, °C	σ_f, ksi	%El	%RA	TTF, hrs
Air	149.6	57.3	67.4	49.9
Acidic / RT	142.9	56.7	66.1	49.2
Acidic / 60	134.2	55.0	65.6	47.7
Acidic / 90	132.1	51.4	64.2	47.4

RT: Room Temperature, Acidic: H_2SO_4 + NaI +H_2O

The SCC data obtained in SSR testing using notched specimens are given in Table 4.5, showing significantly reduced TTF compared to that of the smooth specimens tested under identical conditions. This table also shows the magnitudes of engineering failure

stress (s_f), %El and e_f. Since s_f and %El cannot be used to compare the cracking susceptibility of notched versus smooth specimens, the magnitude of e_f was considered to be useful in differentiating their cracking behavior. As anticipated, the magnitude of e_f was significantly less for the notched specimen due to limited plasticity associated with the failure mechanism.

Table 4.5. SSR Test Results using Notched Specimens

Environment / Temperature, °C	s_f, ksi	%El	TTF, hrs	e_f
Air	67.5	10.1	9.4	0.099
Acidic / RT	62.9	10.5	9.5	0.098
Acidic / 60	62.6	10.4	9.3	0.087
Acidic / 90	55.9	10.1	9.1	0.091

RT: Room Temperature, Acidic: H_2SO_4 + NaI +H_2O

4.5. CPP Test Results

The potentiodynamic polarization diagram obtained from the calibration experiment according to ASTM designation G 05 [69] is illustrated in Figure 4.11, showing a characteristic similar to that of the standard plot. The conventional cyclic potentiodynamic polarization (CPP) diagram of an active-passive material is usually characterized by three critical potentials including corrosion potential (E_{corr}), pitting potential (E_{pit}) and protection potential (E_{prot}), as shown in Figure 4.12. At E_{corr}, the rate of anodic reaction equals that of the cathodic reaction. The magnitude of E_{pit} is determined by the change in slope in the forward polarization curve, showing a transition

from passive to a transpassive region. At this potential, the test material may undergo localized breakdown of protective surface film causing the initiation of pits. The magnitude of E_{prot}, if any, is determined by the intersection of the reverse polarization curve with the passive region, as shown in Figure 4.12. The occurrence of positive hysteresis loop, shown in this figure, is very common with many corrosion-resistant engineering metals and alloys.

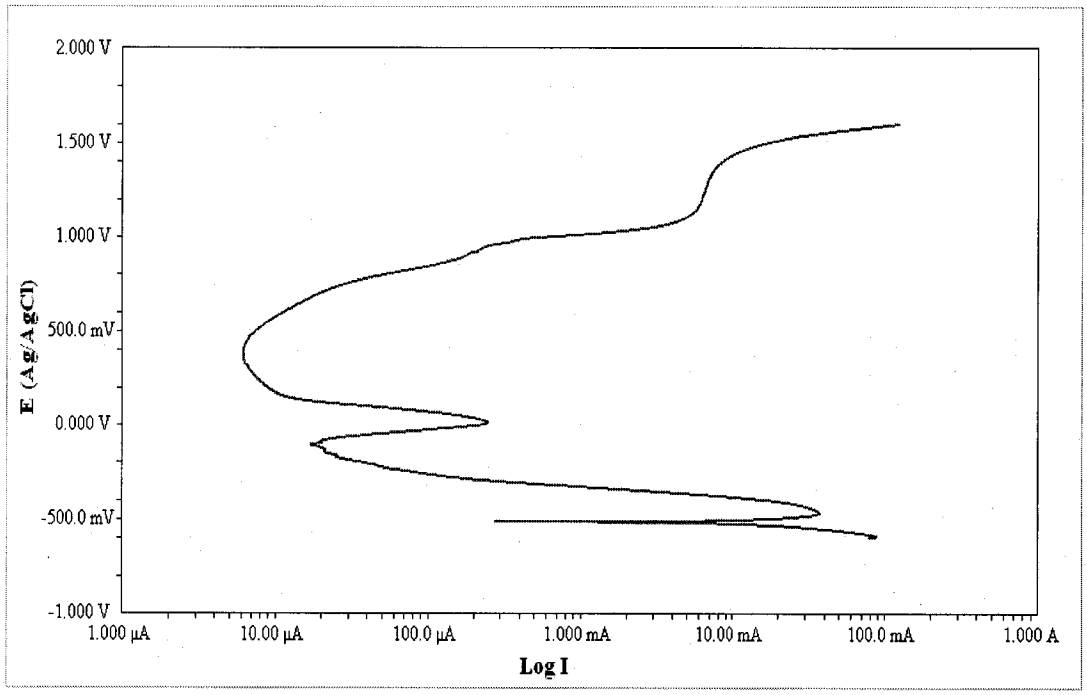

Figure 4.11. ASTM G 05 Calibration Curve

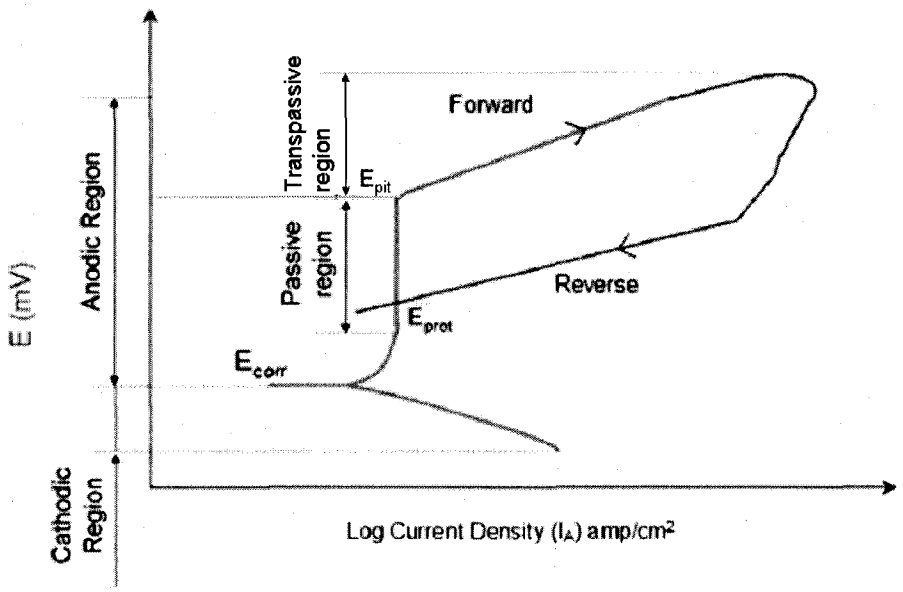

Figure 4.12. Typical CPP Curve for an Active-Passive Material

The results of CPP testing involving Alloy 800H in an identical solution (pH~1) at 30, 60 and 90°C are illustrated in Figures 4.13, through 4.15, respectively, showing an active-passive behavior irrespective of the testing temperature. However, a negative hysteresis loop was formed in the CPP diagram during the reverse polarization scan at all three temperatures, indicating enhanced corrosion resistance possibly due to the formation of fresh protective oxide films on the specimen surface. The formation of these protective films could be the result of dissociation of water by electrolysis at high current densities, thus generating oxygen that could combine with corrosion-resistant alloying elements such as chromium to form chromium oxide (Cr_2O_3). The occurrence of negative hysteresis loop during CPP has also been reported for nickel-base and titanium alloys [77]. It is interesting to note that none of these CPP diagrams did exhibit any E_{prot}, due to the lack of positive hysteresis loop.

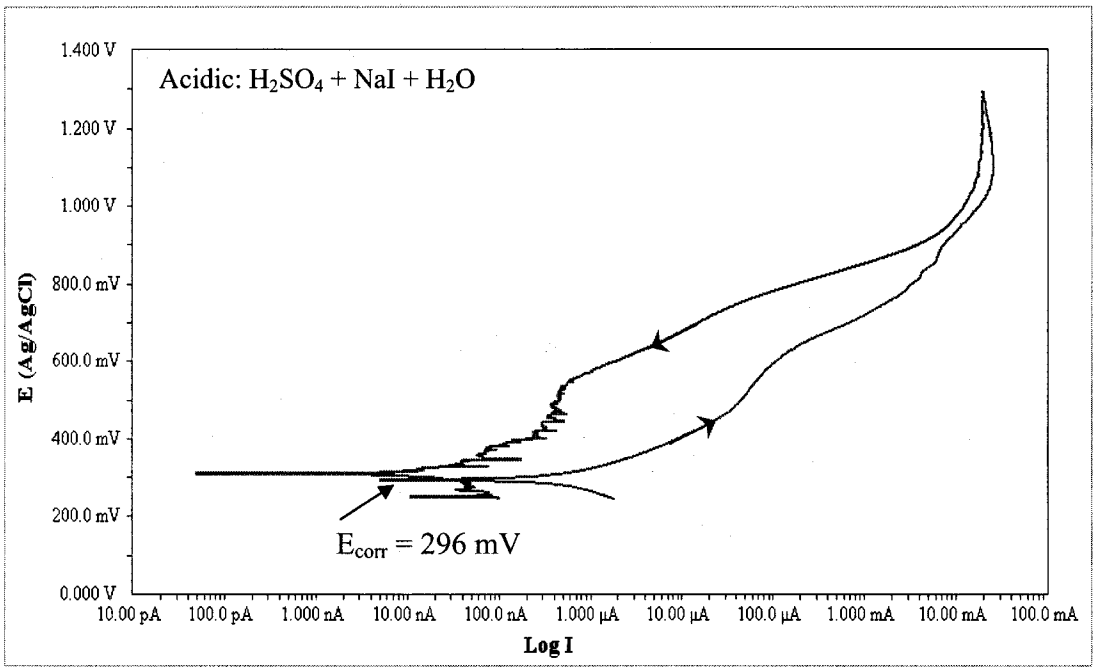

Figure 4.13. CPP Diagram at 30°C

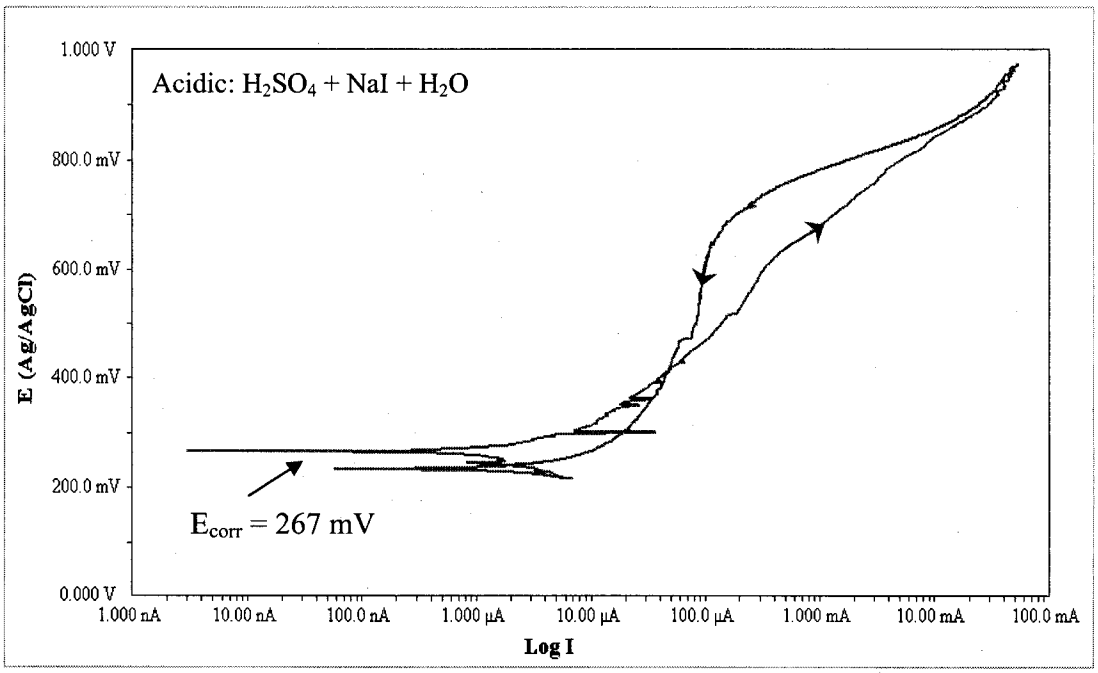

Figure 4.14. CPP Diagram at 60°C

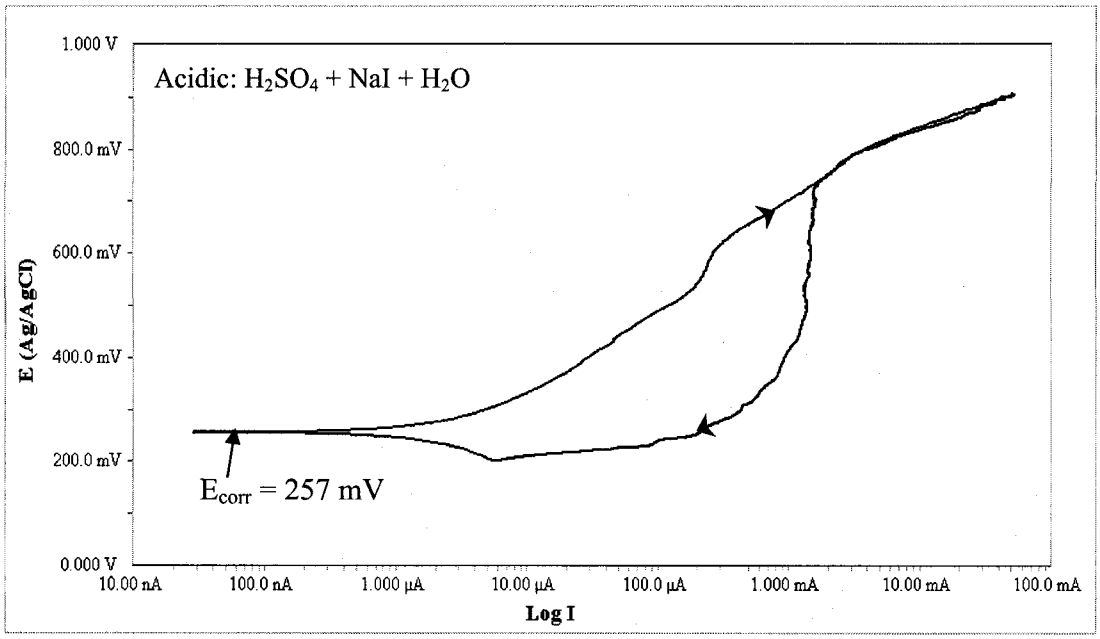

Figure 4.15. CPP Diagram at 90°C

The magnitudes of E_{corr} and E_{pit}, determined from these CPP diagrams, are given in Table 4.6. These data indicate that both E_{corr} and E_{pit} became more active (negative) with increasing temperature. The variations of E_{corr} and E_{pit} with temperature are illustrated in Figure 4.16. The results of CPP testing are consistent with observations made by other investigators [66, 73-74, 78-80]. None of the polarized specimens showed any sign of pitting. However, crevice corrosion was observed on the top surface of the polarized specimens at 60 and 90°C, as shown in Figure 4.17. The extent of crevice corrosion was more pronounced at 90°C.

Table 4.6. Critical Potentials obtained during CPP Tests

Environment / Temperature, °C	E_{corr}, mV	E_{pit}, mV
Acidic / 30	300	620
Acidic / 60	271	611
Acidic / 90	261	598

RT: Room Temperature, Acidic: H_2SO_4 + NaI +H_2O

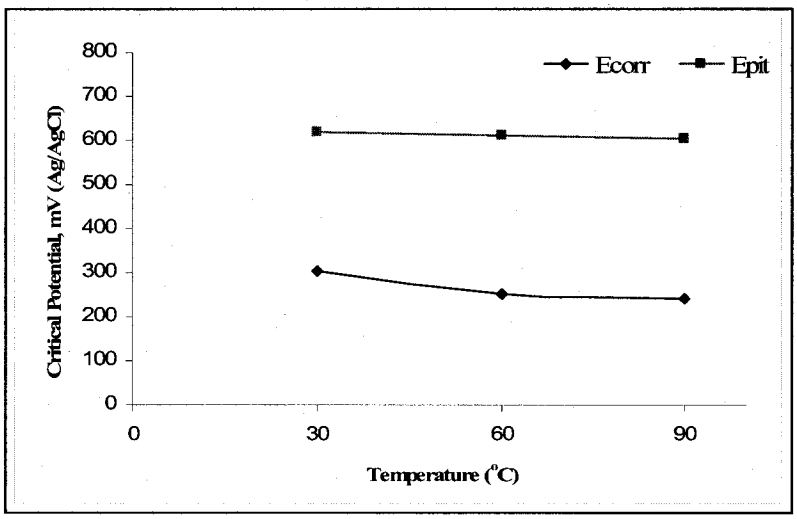

Figure 4.16. Variation of Critical Potentials vs. Temperature

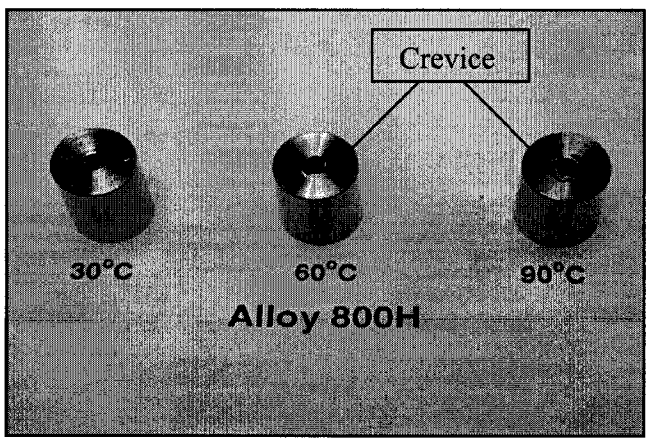

Figure 4.17. Appearances of the Polarized Specimen

4.6. Applied Potential Testing

It has been well documented in the open literature that the cracking susceptibility of engineering materials can be influenced by the externally applied potentials [66-68]. In view of this rationale, the cracking susceptibility of Alloy 800H was determined under the influence of either anodic or cathodic applied potentials while the smooth cylindrical specimen was strained at a rate of 3.3×10^{-6} sec^{-1}. The selection of these controlled potentials (E_{cont}) was based on either the E_{corr} or E_{pit} value measured by the CPP technique in an identical environment. For cathodic E_{cont} testing, the applied potentials (-300 and -500 mV) were active with respect to E_{corr} value. On the contrary, potentials more noble to the E_{pit} value were applied in anodic E_{cont} testing. E_{cont} values of +700, +900, +1000 and +1200 mV were used in anodic potentiostatic polarization tests.

The s-e diagrams of Alloy 800H, superimposed as a function of the testing temperature obtained under cathodic and anodic E_{cont} are illustrated in Figures 4.18, and 4.19, respectively. The s-e diagram obtained without E_{cont} is also superimposed in both figures for comparison purpose. The magnitudes of SCC parameters including %El, %RA, TTF and σ_f under both experimental conditions are given in Tables 4.7, and 4.8, respectively. An evaluation of these data clearly indicates that Alloy 800H did not exhibit any detrimental effect with respect to the cracking susceptibility irrespective of the extent and the nature of potentials applied during straining of the test specimens. It should, however be mentioned that some damaging effect of anodic E_{cont} of +1200 mV was noted in terms of reduced σ_f, ductility and TTF, as shown in Table 4.8.

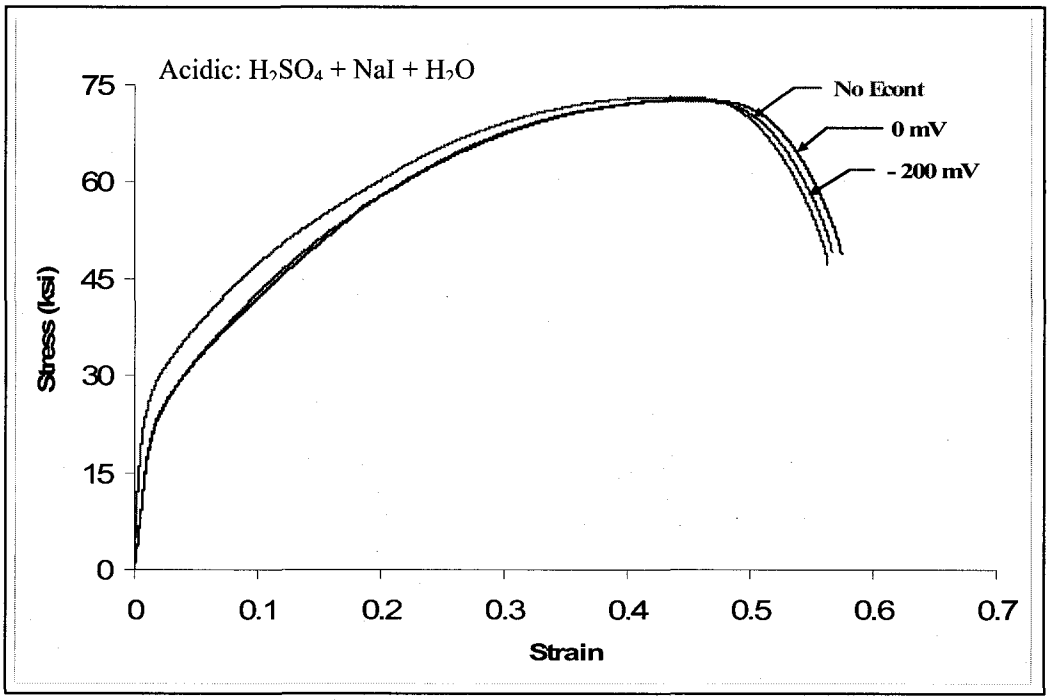

Figure 4.18. s-e Diagrams under Cathodic E_{cont}

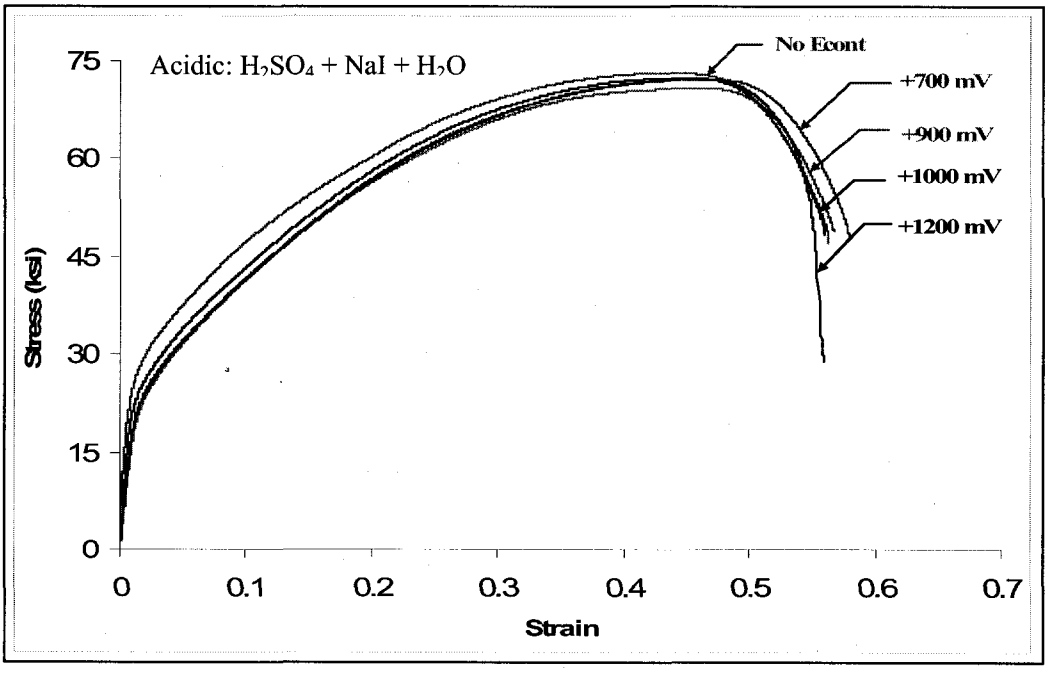

Figure 4.19. s-e Diagrams under Anodic E_{cont}

Table 4.7. SSR Results under Cathodic E_{cont}

Environment / Temperature	E_{cont}, mV	σ_f, ksi	%El	%RA	TTF, hrs
Acidic / RT	No E_{cont}	142.9	56.7	66.1	49.2
	0	142.8	55.9	65.6	48.8
	-200	141.7	56.0	65.9	48.9

RT: Room Temperature, Acidic: H_2SO_4 + NaI +H_2O

Table 4.8. SSR Results under Anodic E_{cont}

Environment / Temperature	E_{cont}, mV	σ_f, ksi	%El	%RA	TTF, hrs
Acidic / RT	No E_{cont}	142.9	56.7	66.1	49.2
	700	151.4	56.9	68.5	49.1
	900	144.7	55.6	66.8	48.4
	1000	134.6	56.0	66.1	48.2
	1200	76.2	54.5	61.9	46.7

RT: Room Temperature, Acidic: H_2SO_4 + NaI +H_2O

4.7. SCC Testing involving Self-Loaded Specimens

Efforts were made to evaluate the cracking susceptibility of self-loaded C-ring and U-bend specimens at temperatures above boiling using an autoclave made of corrosion-resistant Alloy C-276. However, the autoclave was leaking at elevated temperatures due to gasket failure. Therefore, C-ring and U-bend specimens were tested inside corrosion-resistant chambers containing acidic solution (H_2SO_4 only) at 90°C. The C-ring specimens were loaded at 98% of the room temperature YS value of Alloy 800H to reduce the inner diameter. While the C-ring specimens were tested for a maximum duration of 58 days, the U-bend specimens were exposed to the test solution for only 14

days. The use of C-ring and U-bend specimen enabled the evaluation of cracking susceptibility of Alloy 800H due to circumferential stress, which is tensile in nature.

The results indicate that no cracking was experienced by either type of specimens, irrespective of the testing duration. However, significant dissolution of surface film was observed with the C-ring specimens, as illustrated in Figure 4.20. The corresponding weight-loss of the C-ring specimens as a function of the test durations are also illustrated in Figure 4.21, showing gradual increase in weight-loss at 90°C.

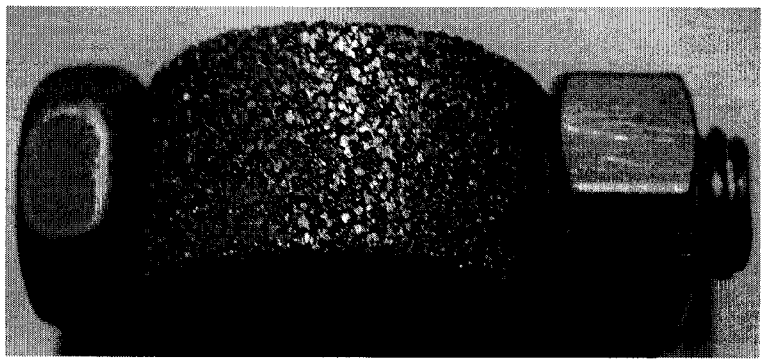

Figure 4.20. C-ring Specimen after 58 days

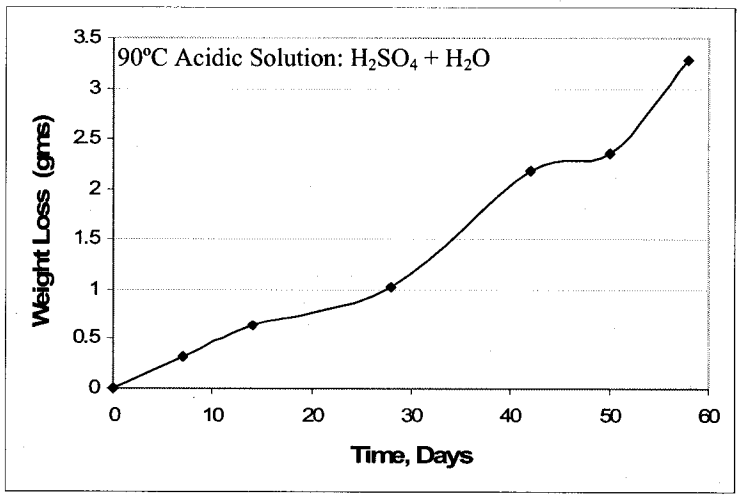

Figure 4.21. Weight-loss in C-ring Specimen after 58 days

4.8. Scanning Electron Microscopy

The results of fractographic evaluations of cylindrical specimens used in tensile, and SCC (with and without E_{cont}) testing are illustrated in Figures 4.22 through 4.26, showing the extent and morphology of failure. An evaluation of the SEM micrographs of the tensile specimens revealed ductile failure with some tiny grain boundary cracks at temperatures up to 200°C, possibly due to the strain-hardening effect. However, beyond this temperature, the tensile specimens showed classical dimpled microstructure up to 800°C, indicating ductile failures. The notched cylindrical specimen did not exhibit any cracking when tested at room temperature in air.

The results of SEM study involving smooth and notched cylindrical specimens in SSR testing with and without environment are illustrated in Figures 4.24 and 4.25, respectively. The SEM micrographs shown in Figure 4.24 revealed the presence of micro-cracks in smooth cylindrical specimens when tested in the acidic solution at temperatures ranging between ambient and 90°C. It is interesting to note that cracks were also observed in Alloy 800H when tested without any environment at ambient temperature under a strain rate of $3.3x10^{-3}$ sec^{-1}. The SEM micrographs involving notched cylindrical specimens revealed predominantly ductile failures characterized by dimples. These results suggest that the occurrence of cracking in smooth specimens may be the results of longer failure times compared to that of the notched specimens, which resulted in premature failure due to K_t. The application of E_{cont} (cathodic and anodic) to the smooth cylindrical specimens during SSR testing also produced cracks, as illustrated in Figure 4.26. It should however be noted that the extent of cracking was more pronounced in cathodic E_{cont} as shown in Figure 4.26 (a).

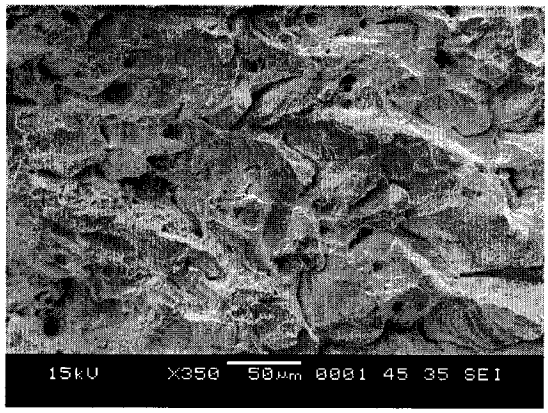

(a) Ambient Temperature

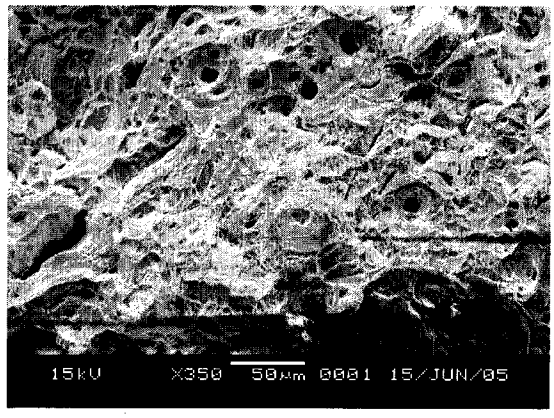

(b) 100°C

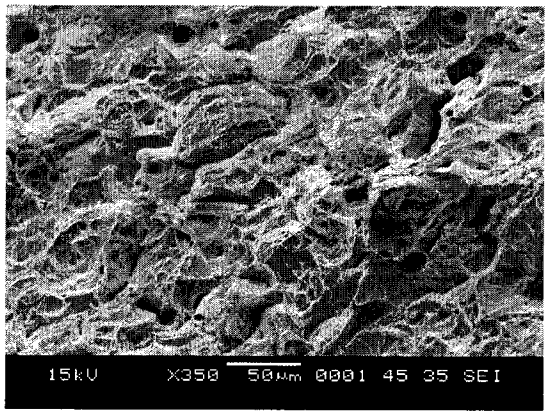

(c) 200°C

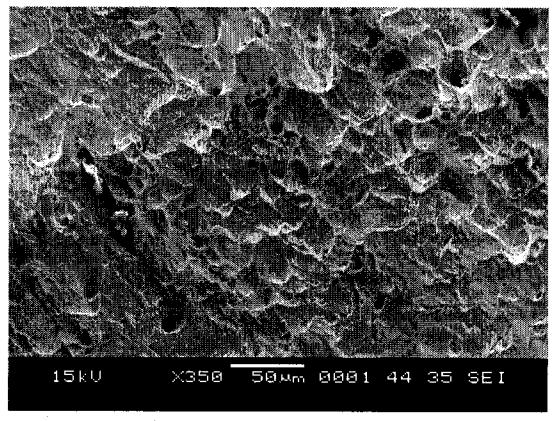

(d) 300°C

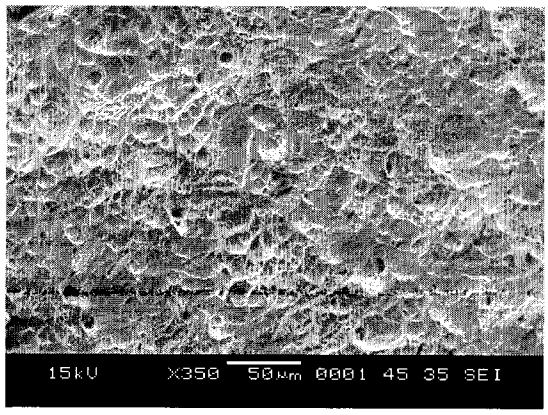

(e) 400°C

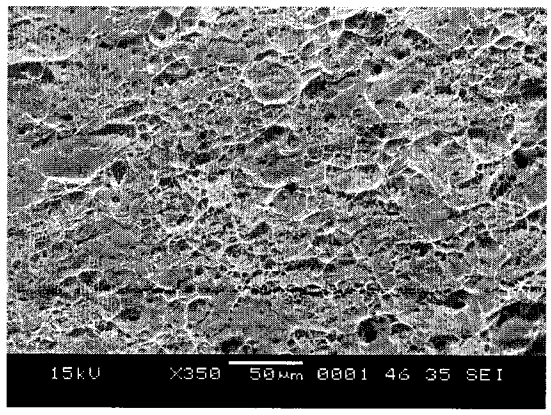

(f) 500°C

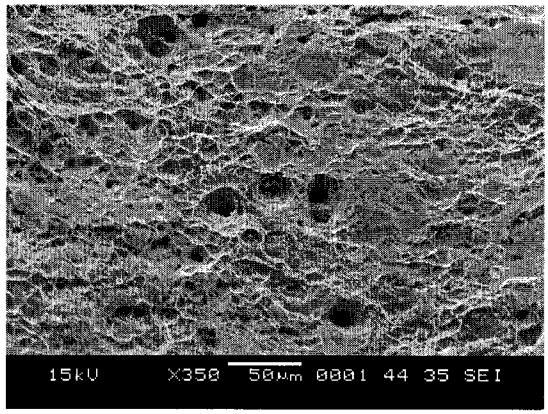

(g) 600°C

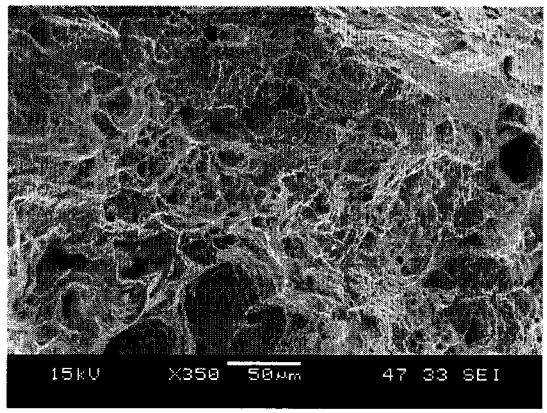

(h) 700°C

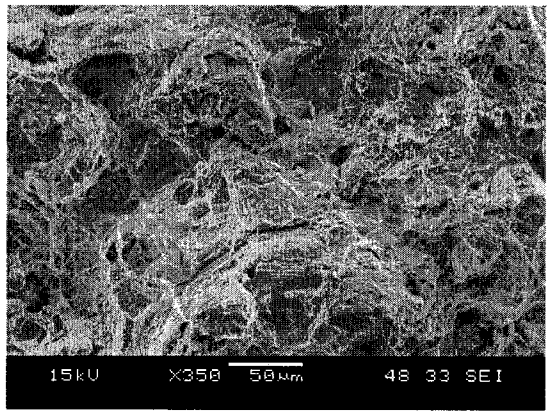

(i) 800°C

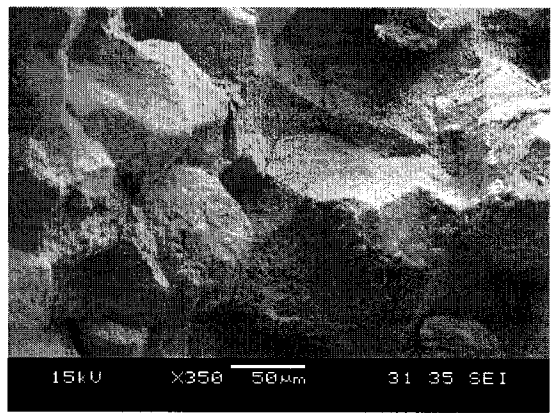

(j) 1000°C

Figure 4.22. SEM Micrographs of Smooth Specimen (Tensile Testing)

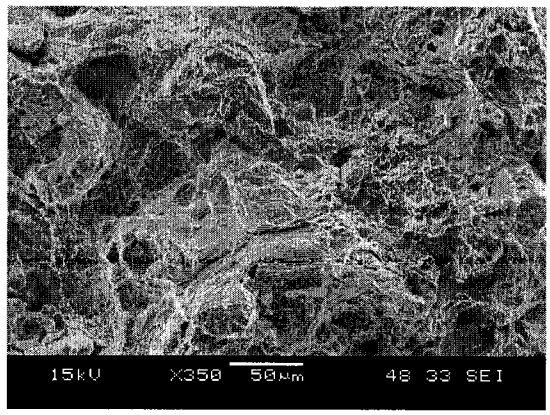

Figure 4.23. SEM Micrographs of Notched Specimen (Tensile Testing)

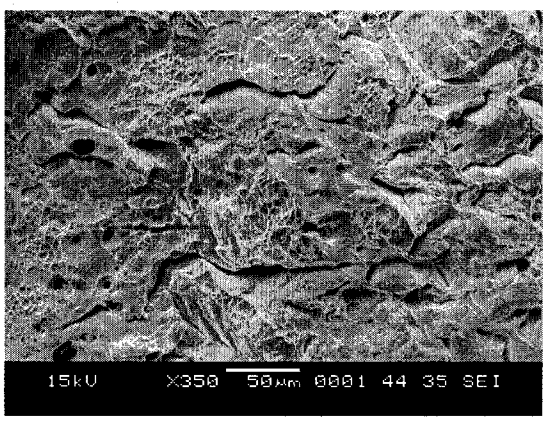

(a) Air

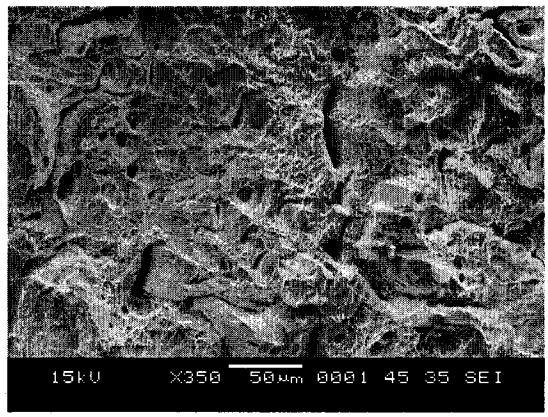

(b) Ambient Temperature, Acidic

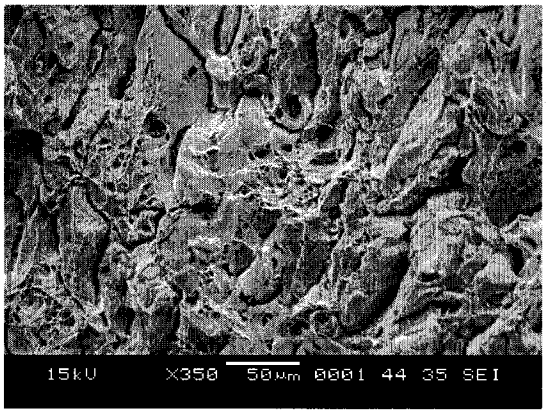

(c) 60°C, Acidic

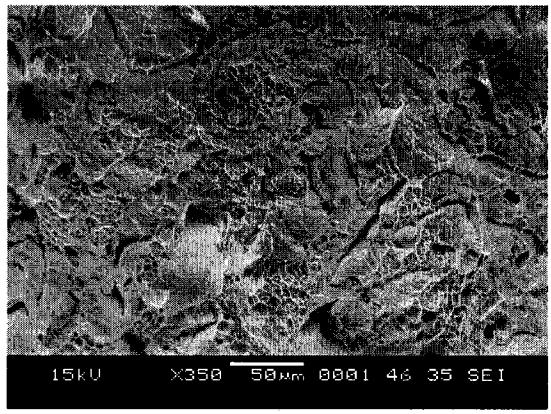

(d) 90°C, Acidic

Figure 4.24. SEM Micrographs of Smooth Specimen (SSR Testing)

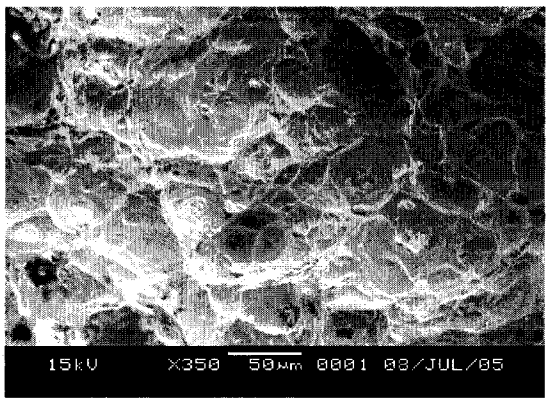

(a) Air

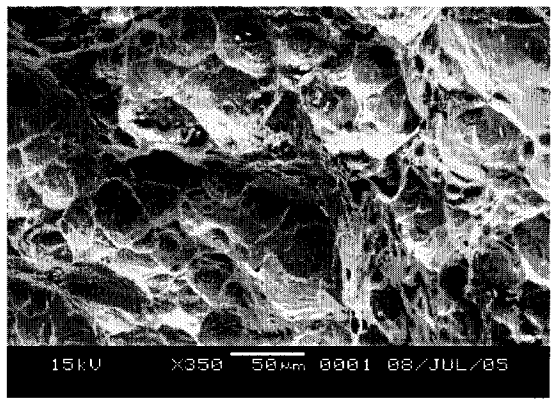

(b) Ambient Temperature, Acidic

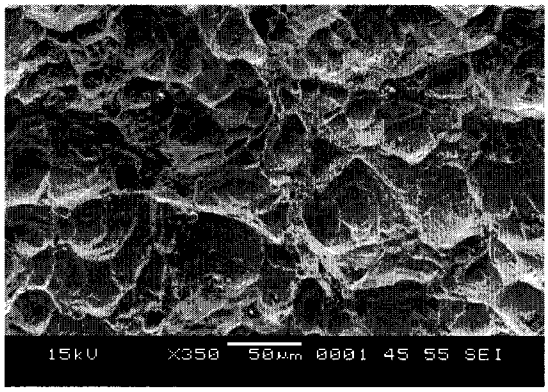

(c) 60°C, Acidic

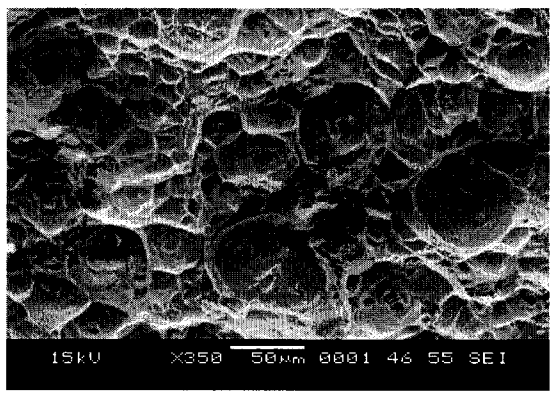

(d) 90°C, Acidic

Figure 4.25. SEM Micrographs of Notched Specimen (SSR Testing)

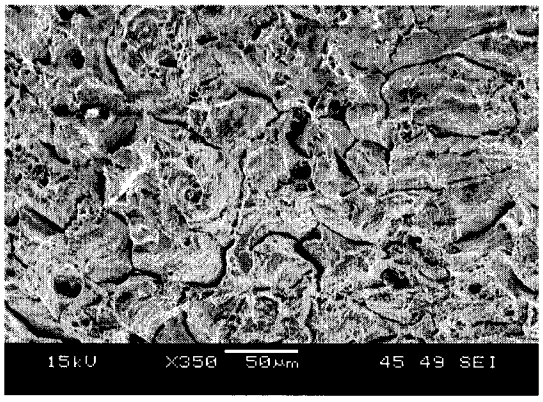

(a) E_{cont} = -200 mV

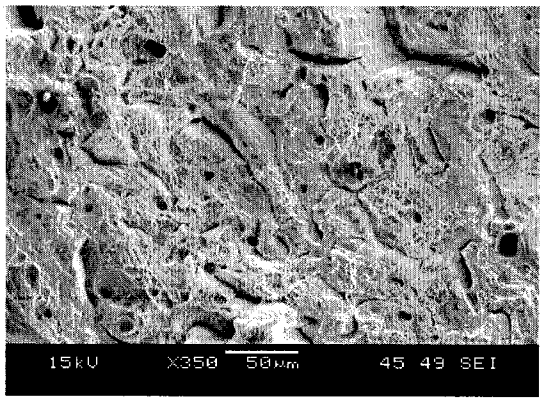

(b) E_{cont} = +900 mV

Figure 4.26. SEM Micrographs of SSR Testing under E_{cont}

CHAPTER 5

DISCUSSION

As mentioned earlier in this thesis, this investigation was focused on characterizing the metallurgical and corrosion behavior of an iron-nickel-chromium (Fe-Ni-Cr) alloy known as Alloy 800H for prospective applications as a structural material in heat exchangers to be used for nuclear hydrogen generation. A discussion on the resultant tensile data will be presented in this section followed by corrosion data generated on this alloy. The results of tensile testing indicate that both the yield strength (YS) and ultimate tensile strength (UTS) were gradually reduced with increasing temperature due to reduced load-bearing capability at higher temperatures. It is, however, interesting to note that Alloy 800H was also capable of maintaining relatively high failure strength up to 600°C. Beyond this temperature, the magnitudes of YS, UTS and the failure strength were significantly reduced.

As to the failure strain of Alloy 800H at different temperatures, an interesting phenomenon was noticed that it was gradually reduced between ambient temperature and 200°C followed by a gradual enhancement above this temperature. The reduced failure strain in this temperature regime signifies work-hardening of Alloy 800H, a phenomenon which is often referred to as dynamic strain aging (DSA) of engineering materials at some critical temperatures [81-86]. The phenomenon of DSA has often been attributed to the diffusion of solute elements such as carbon and nitrogen into the metal matrix, thus

inhibiting the movement of dislocation past the grain boundaries. It is possible that there was no significant driving force in Alloy 800H to activate the movement of dislocations to cause plastic deformation at temperatures up to 200°C. Since the plastic deformation could be significantly enhanced at higher temperatures, the increased failure strain beyond 200°C could be the result of enhanced plastic flow due to higher driving force for movement of dislocations [87-90].

It has been suggested that DSA can occur over a wide temperature range and that the temperature interval in which it is observed depends on the strain rates [91]. However, the DSA phenomenon experienced by the cylindrical specimens tested in this investigation occurred at a strain rate of 10^{-3} sec^{-1} only. Thus, the effect of strain rate on DSA cannot be rationalized in this case. The concept of DSA can easily be characterized in terms of dislocation density determined by transmission electron microscopy. The occurrence of reduced failure strain in the temperature regime of 500 to 1000°C also needs further investigation. Therefore, it is suggested that future effort be focused on characterizing the dislocation density at temperatures at, above and below the critical temperature of 200 and 500°C. Simultaneously, it may be worthwhile to investigate the role to strain rate on DSA in future investigations. The occurrence of DSA within a certain temperature range, as seen in this investigation, is consistent with observations made by other investigators on engineering materials [92-95].

With respect to the corrosion behavior of Alloy 800H, no failure was observed in a 90°C acidic solution at constant-load even at an applied stress of 0.98YS. Since autoclave testing could not be performed at elevated temperatures due to the gasket failure, it is recommended that stress-corrosion-cracking (SCC) testing involving self-loaded (C-ring

and U-bend) specimens be performed by future investigators to study the effect of temperature on the cracking susceptibility of Alloy 800H. Such testing would enable a comparison of SCC behavior as a function of loading condition and temperature. As to the cracking susceptibility under a slow-strain-rate (SSR) condition using smooth specimens, slight variations in percent elongation (%El), percent reduction in area (%RA) and time-to-failure (TTF) were noted when tested in an identical environment at different temperatures. However, the magnitude of the true failure stress (σ_f) was reduced by an appreciable amount at 90°C. In view of these results, it may be stated that ductility and TTF for Alloy 800H may not be influenced by the range in temperature used in this study. As to the cracking susceptibility of the notched specimen, the TTF was significantly reduced compared to that of the smooth specimen, possibly due to the tri-axial stress condition at the root of the notch.

None of the polarized specimens did exhibit any pitting. However, slight crevice corrosion tendency was noted in these specimens at 60 and 90°C. The magnitude of critical potentials (corrosion potential-E_{corr} and pitting potential-E_{pit}) determined from the cyclic potentiodynamic polarization experiments showed a consistent pattern in that these potentials became more active at elevated temperatures possibly due to the dissolution, and breakdown of surface films at relatively higher temperatures. A similar trend on the variation of E_{corr} and E_{pit} with temperature has been well documented in the open literature [78].

The results of SCC testing using the SSR technique did not exhibit any significant effect of cathodic controlled potential (E_{cont}) on the cracking susceptibility in terms of σ_f, %El, %RA and TTF. However, reduced σ_f values were observed under anodic E_{cont}, the

effect being more pronounced at an applied potential of +600mV with respect to the E_{pit} value. These data suggest that cracking tendency of Alloy 800H may be enhanced at relatively higher anodic E_{cont} values in an identical testing environment.

The metallographic evaluations by optical microscopy revealed conventional austenitic grains and annealing twins, as anticipated for a solution-annealed Fe-Ni-Cr steel [96]. Some secondary precipitates were also formed, which includes titanium nitrides, titanium carbides and chromium carbides, similar to the one cited in the open literature [16]. The morphology of failures determined by scanning electron microscope (SEM) was characterized by dimples with some tiny cracks along the grain boundaries of smooth tensile specimens that showed some signs of DSA behavior. The SEM micrographs of smooth specimens used in SSR testing also showed the presence of intergranular cracks irrespective of the testing temperature. However, classical dimpled microstructures were seen in the SEM micrographs of the notched specimen due to significantly less failure time. As to the cracking morphology of Alloy 800H under E_{cont}, the severity of cracking was more pronounced in smooth specimens tested under cathodic E_{cont}.

CHAPTER 6

SUMMARY AND CONCLUSIONS

The tensile properties of Alloy 800H have been evaluated at temperatures ranging from ambient to 1000°C. The cracking susceptibility of this alloy has been determined in an acidic solution under constant-load (CL) and slow-strain-rate (SSR) conditions. The localized corrosion behavior has been studied using a polarization technique. The effect of applied potential on the cracking tendency has also been investigated under anodic and cathodic controlled potentials (E_{cont}). Metallographic and fractographic evaluations have been performed by optical microscopy and scanning electron microscopy, respectively. The significant conclusions derived from this investigation are summarized below.

- Alloy 800H was capable of maintaining appreciably high tensile strength up to 600°C, followed by its gradual reduction beyond this temperature. The ductility in terms of failure strain, thus also percent elongation (%El) was reduced at temperatures up to 200°C and beyond 500°C up to 1000°C.
- Between 200 and 500°C, enhanced ductility in terms of %El was noted. However, the percent reduction in area (%RA) was gradually reduced between ambient temperature and 500°C.

- The reduced failure strain up to 200°C and beyond 500°C could be attributed to the dynamic strain aging effect that is normally related to the impeding movement of dislocations in these temperature regimes.
- Alloy 800H did not exhibit any failure in the acidic solution at CL indicating a threshold stress approaching 98% of its room temperature yield strength value.
- Slight reductions in the true failure stress (σ_f), %El, %RA, and time-to-failure (TTF) were observed in stress-corrosion-cracking testing using smooth specimens in an identical environment with increasing temperature, when tested under a SSR condition.
- For notched specimens, the TTF was significantly reduced due to the stress concentration effect associated with a triaxial stress condition.
- The localized corrosion study by the cyclic potentiodynamic polarization technique showed a negative hysteresis loop at all tested temperatures indicating reduced corrosion during the reverse potential scan. The magnitudes of critical potentials (corrosion potential-E_{corr} and pitting potential-E_{pit}), however became more active with increasing temperature.
- The effect of cathodic E_{cont} on the cracking susceptibility was insignificant. However, appreciable reductions in σ_f, %RA and TTF were observed in SSR testing performed under an anodic E_{cont} value of +600 mV with respect to E_{pit}.
- Neither C-ring nor U-bend specimens exhibited any cracking in the 90°C acidic solution when exposed for variable durations. However, a gradual increase in weight-loss was observed in C-ring specimens with increasing test duration.

- Metallographic evaluations revealed classical austenitic grains, annealing twins and precipitates. Fractographic evaluations showed a combination of dimples and tiny cracks in the vicinity of the grain boundaries in majority of the tested specimens.
- The specimens tested under cathodic E_{cont} exhibited severe intergranular cracks in SSR testing. Some tiny cracks were also observed in anodically polarized cylindrical specimens.

CHAPTER 7

SUGGESTED FUTURE WORK

Additional work is warranted to successfully characterize and select Alloy 800H for applications as a heat exchanger material for hydrogen generation using the sulfur-iodine cycle. The future work is suggested below.

- Characterization of defects (dislocations) by transmission electron microscopy to develop and understanding on dynamic strain aging behavior.
- Continuation of stress-corrosion-cracking evaluation using self-loaded specimens (C-ring, U-bend and double-cantilever-beam) at elevated temperatures in an autoclave.
- Duplication of tensile properties evaluations at 1000°C.
- Crack-growth studies in with and without a corrosive environment under static and dynamic loading.
- Fracture toughness evaluations as a function of temperature.
- Impact toughness evaluations using V-notched charpy specimens.

APPENDIX A

TENSILE TEST DATA

A.1. Tensile Test Data of Alloy 800H

A.1.1. Stress-Strain curves at ambient temperature

A.1.1.1. Tested in MTS

(A conversion factor of 6.895 can be used to convert ksi to MPa)

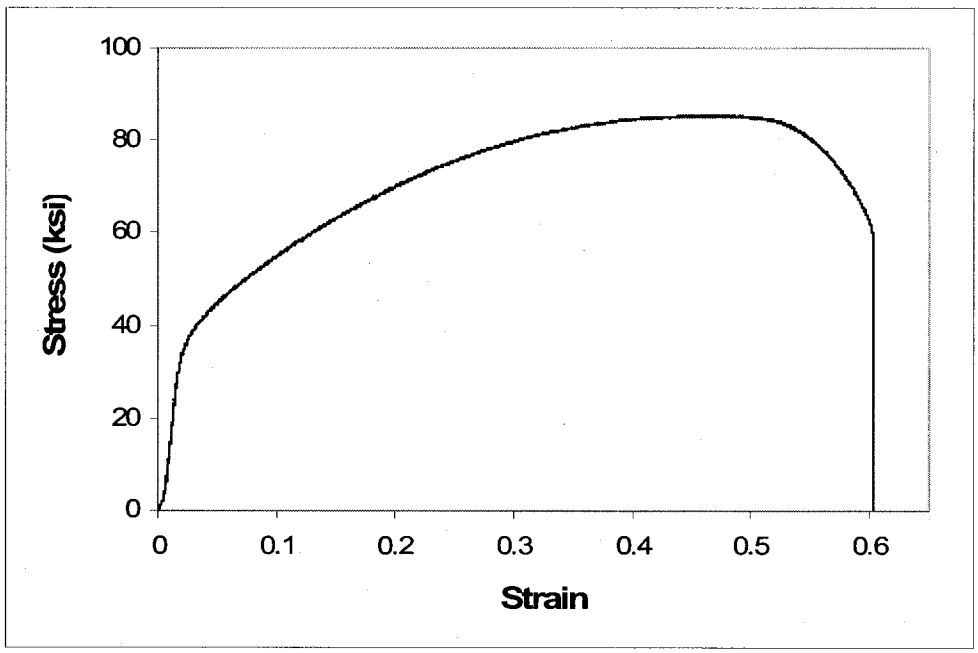

Sample 1

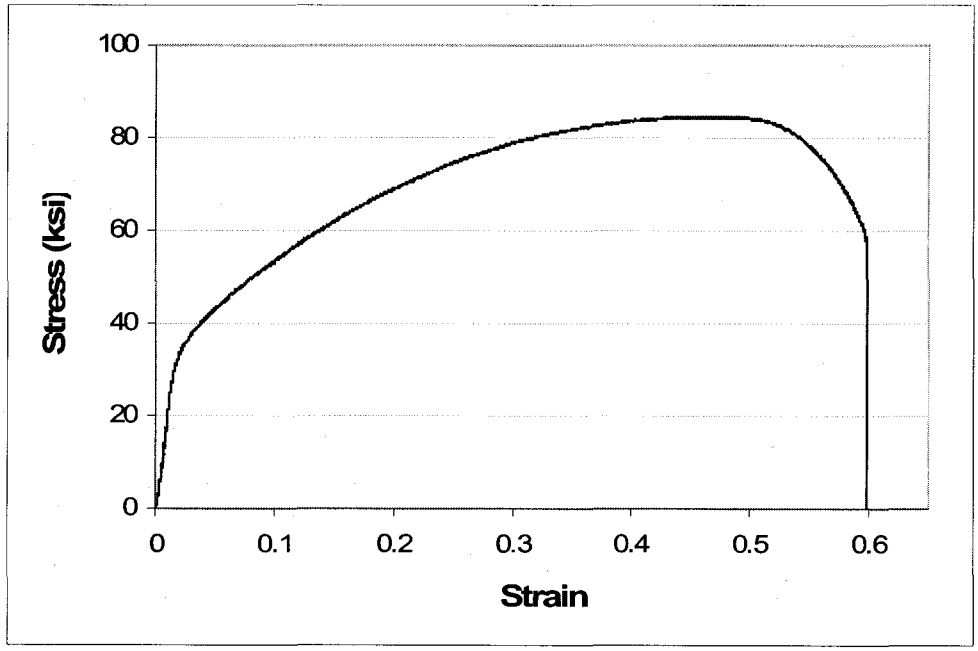

Sample 2

A.1.1.2. Tested in Instron

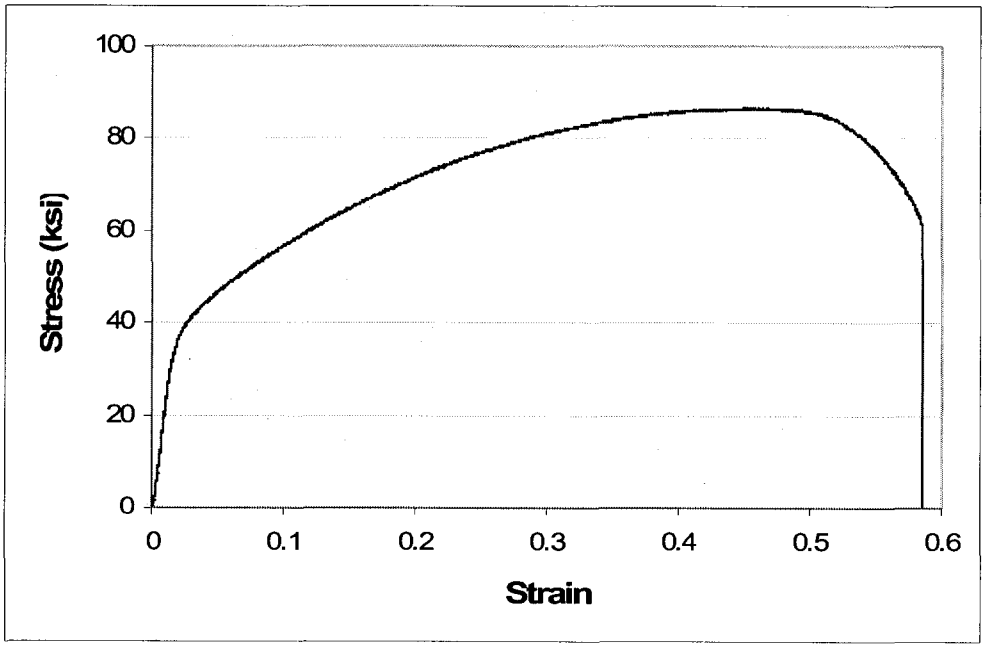

Sample 3

A.1.2. Stress-Strain curves at 100°C

A.1.2.1. Tested in MTS

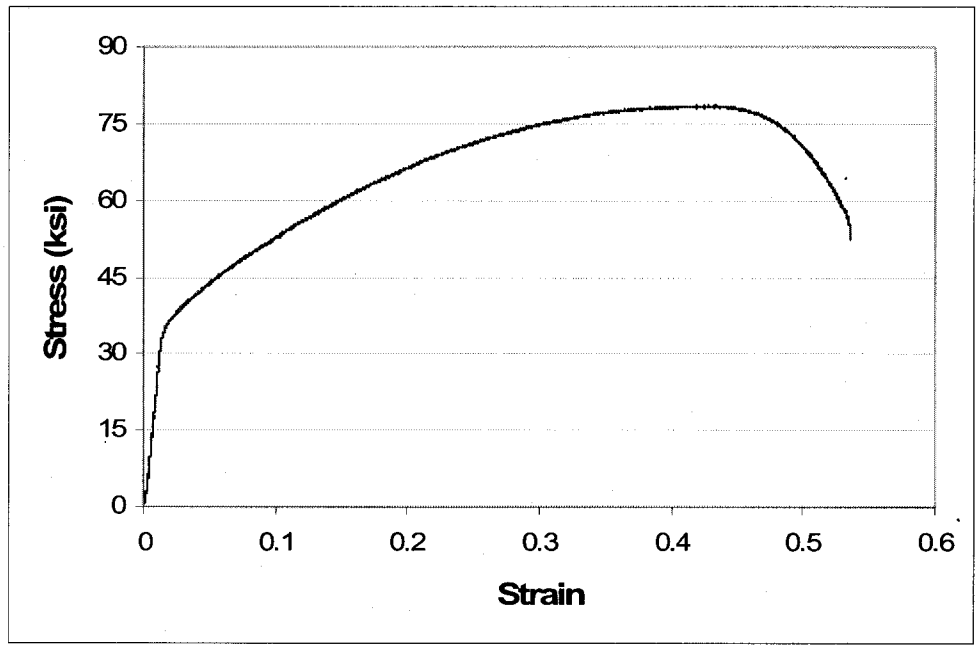

Sample 1

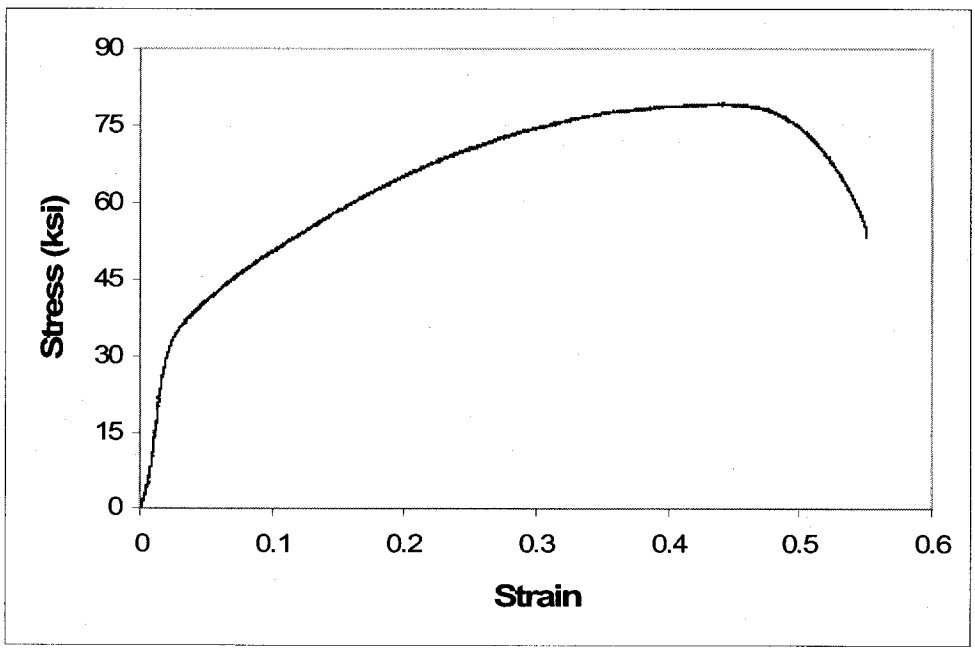

Sample 2

A.1.2.2. Tested in Instron

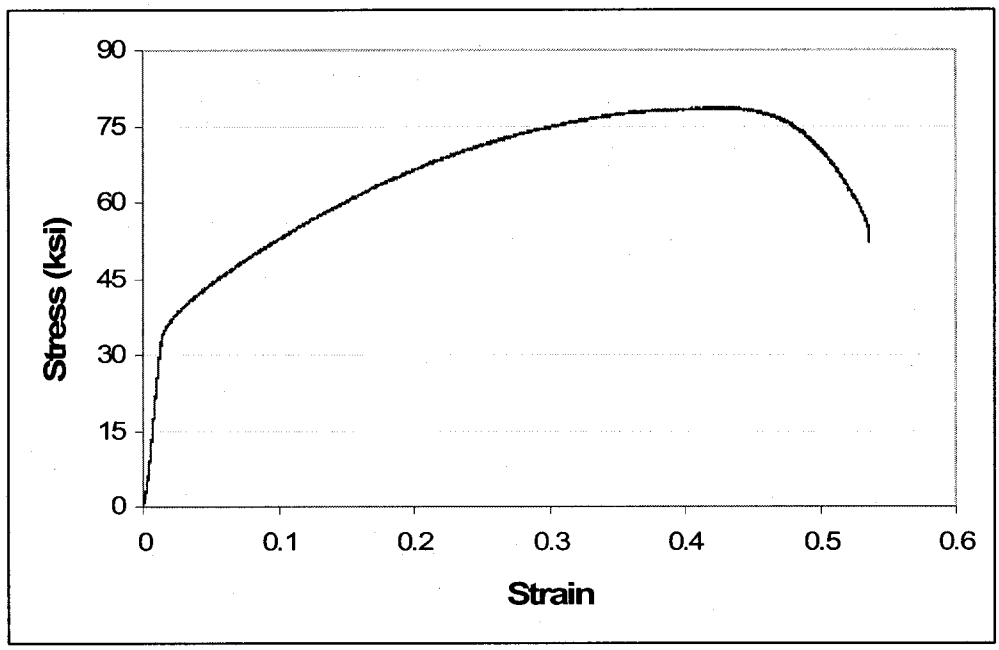

Sample 3

A.1.3. Stress-Strain curves at 200°C

A.1.3.1. Tested in MTS

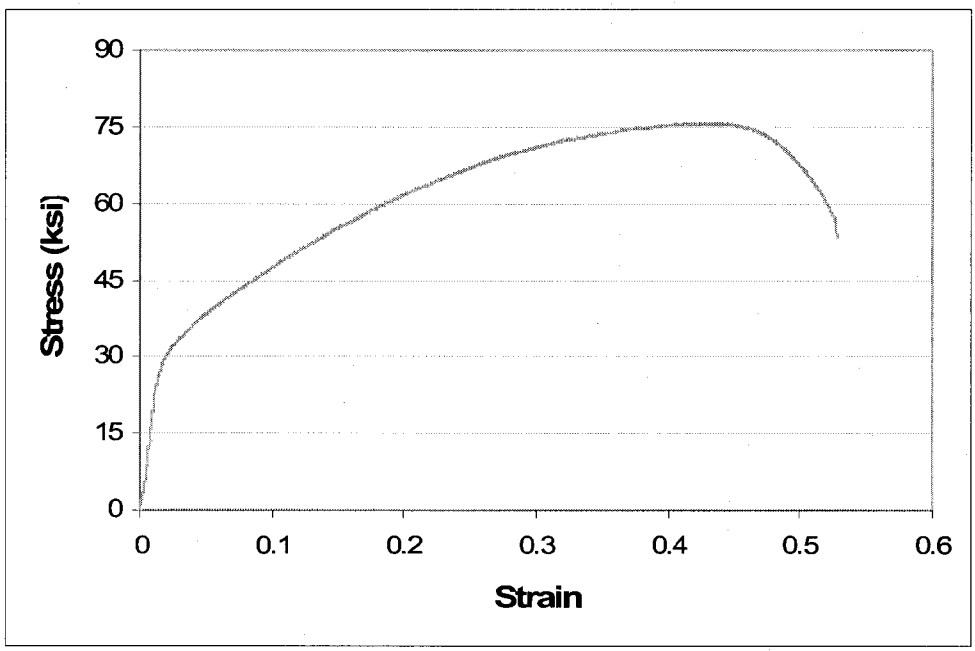

Sample 1

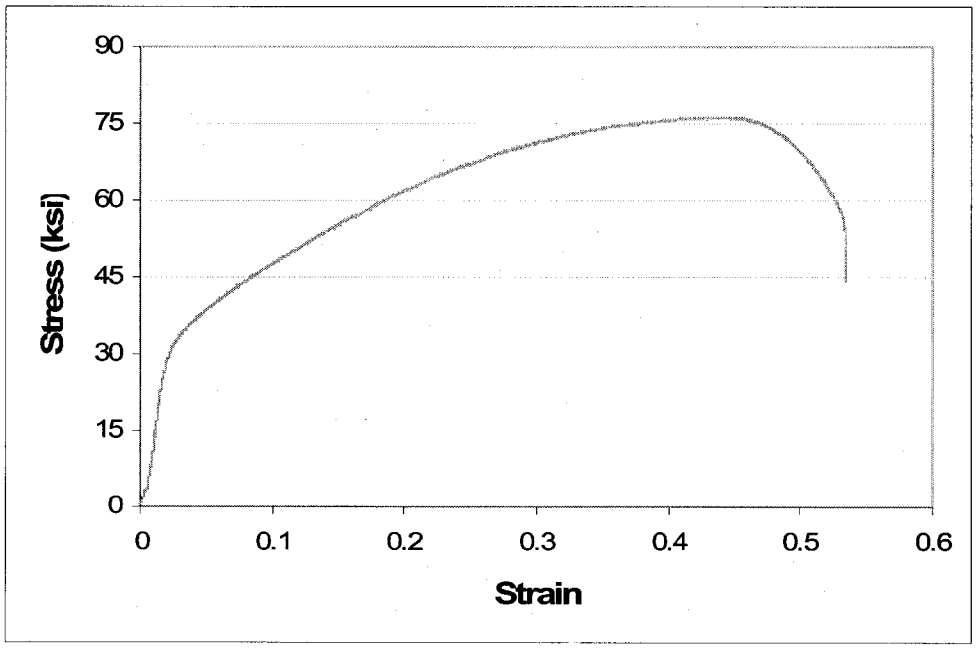

Sample 2

A.1.3.2. Tested in Instron

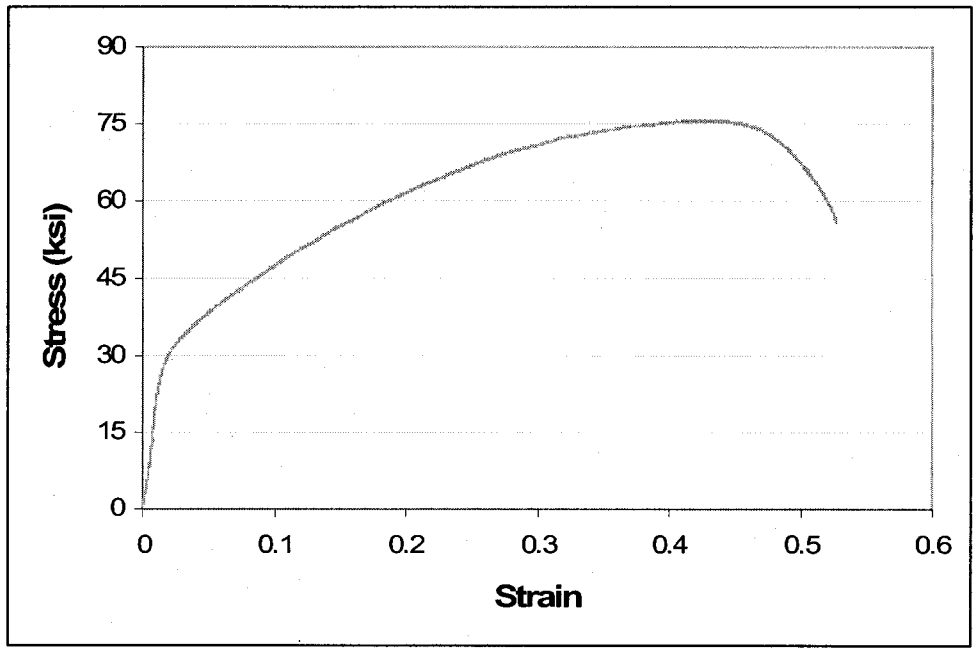

Sample 3

A.1.4. Stress-Strain curves at 300°C

A.1.4.1. Tested in MTS

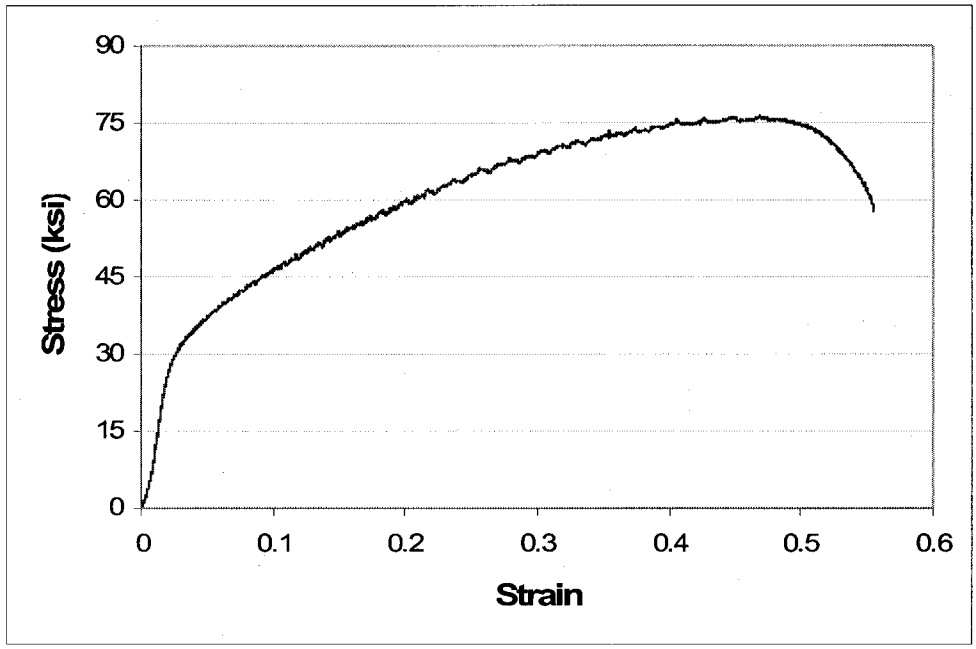

Sample 1

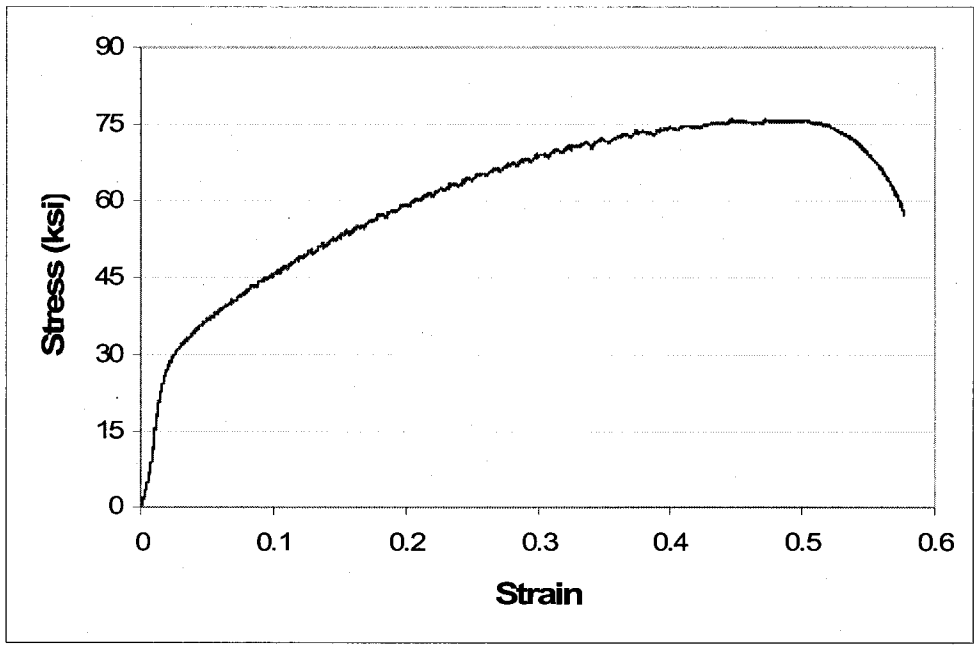

Sample 2

A.1.4.2. Tested in Instron

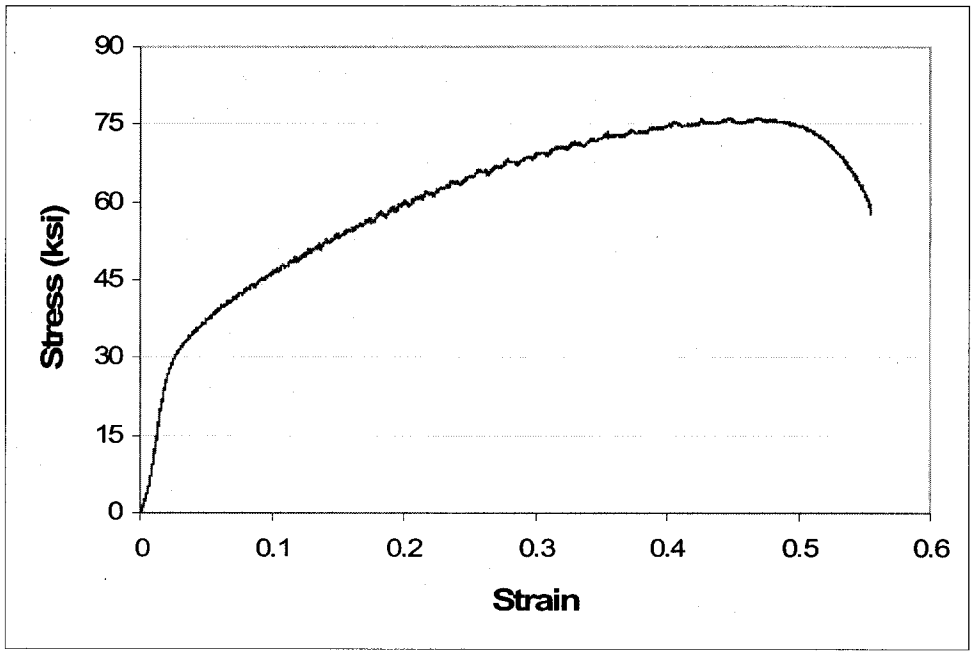

Sample 3

A.1.5. Stress-Strain curves at 400°C

A.1.5.1. Tested in MTS

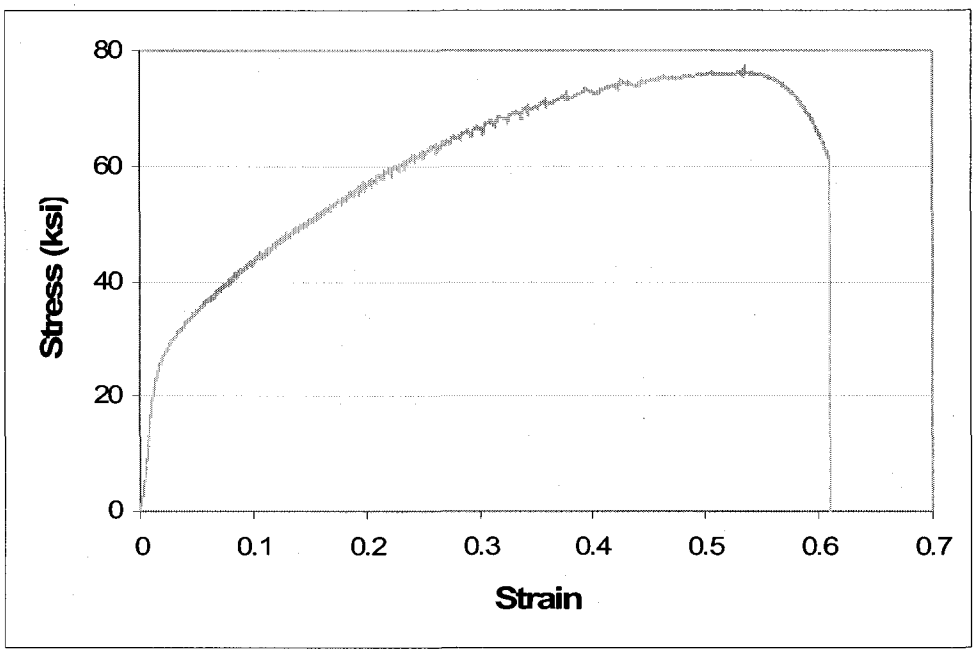

Sample 1

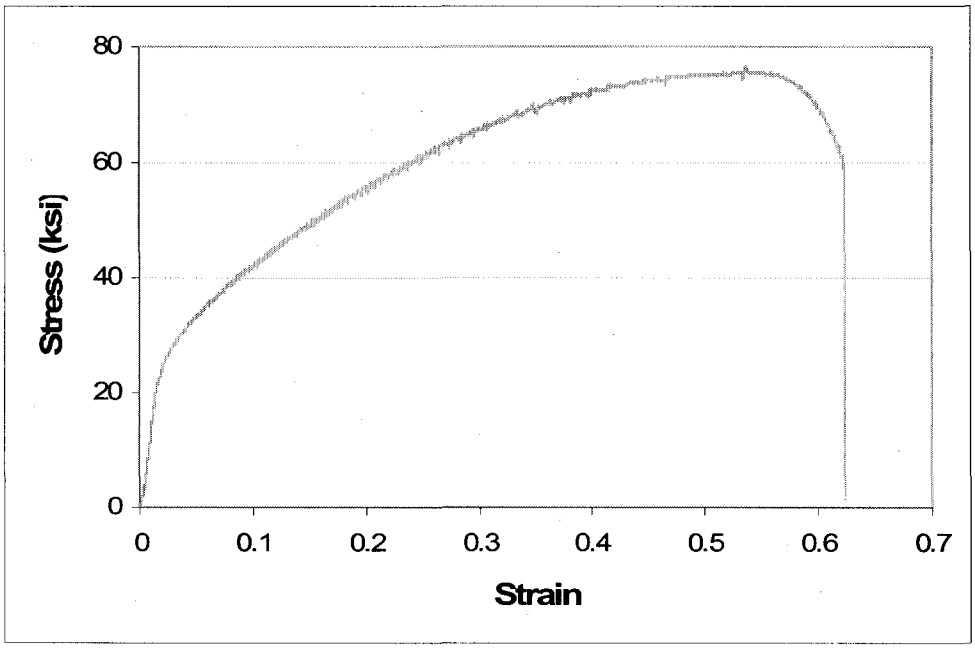

Sample 2

A.1.5.2. Tested in Instron

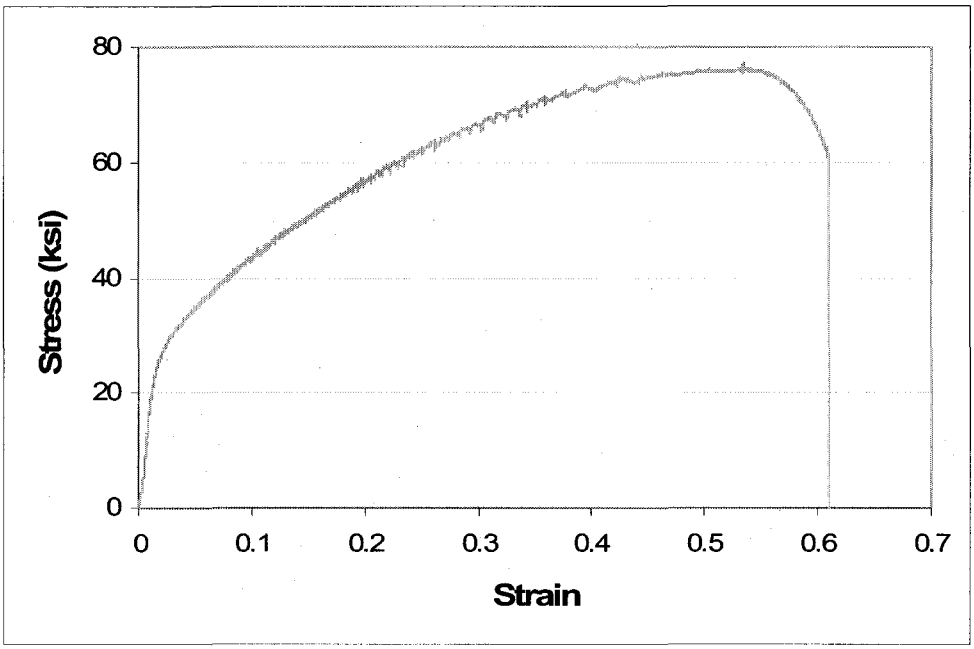

Sample 3

A.1.6. Stress-Strain curves at 500°C

A.1.6.1. Tested in MTS

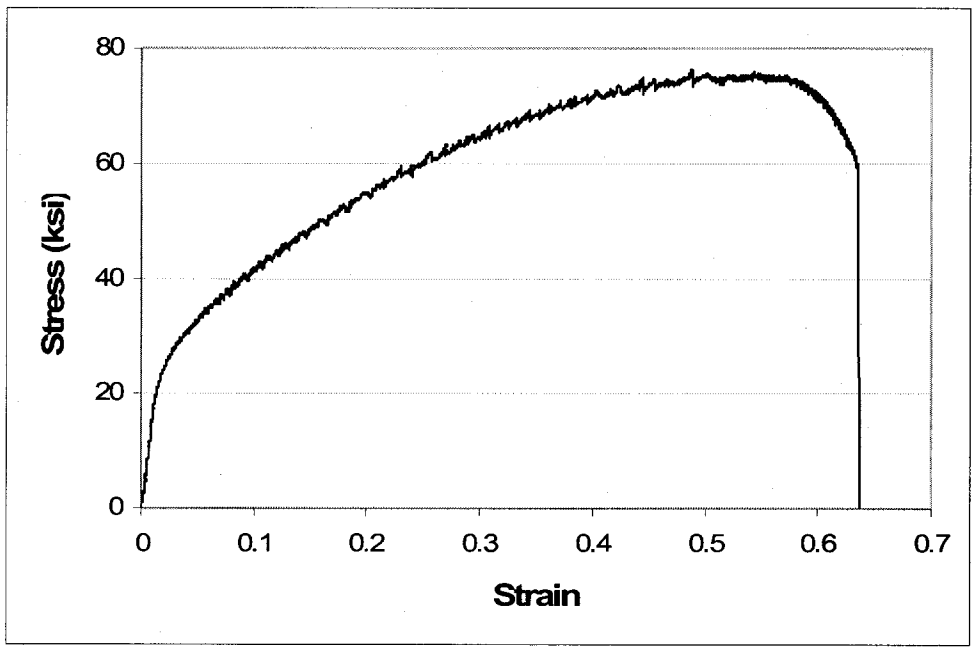

Sample 1

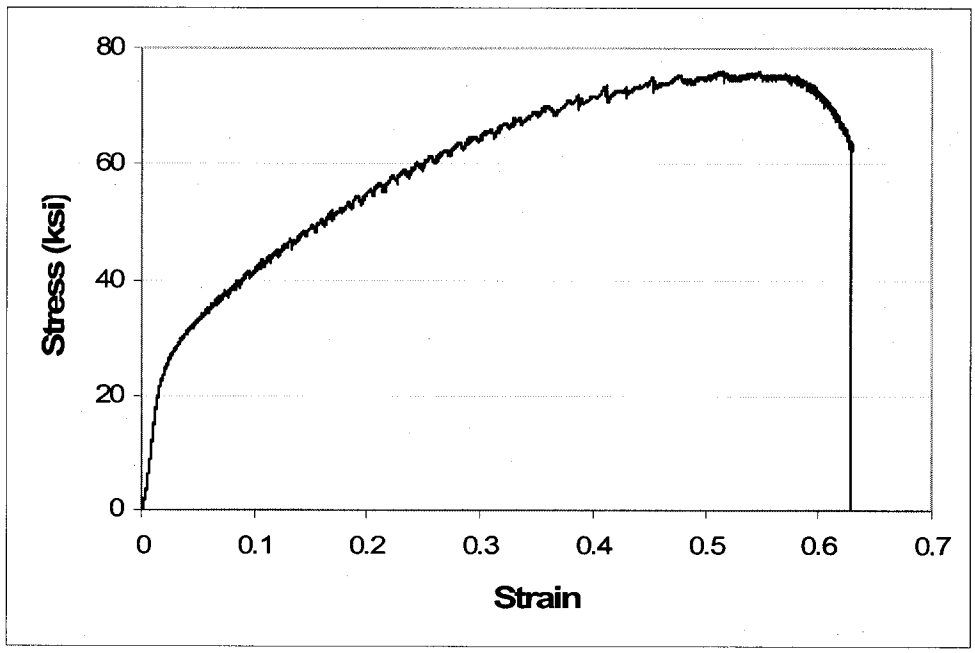

Sample 2

A.1.6.2. Tested in Instron

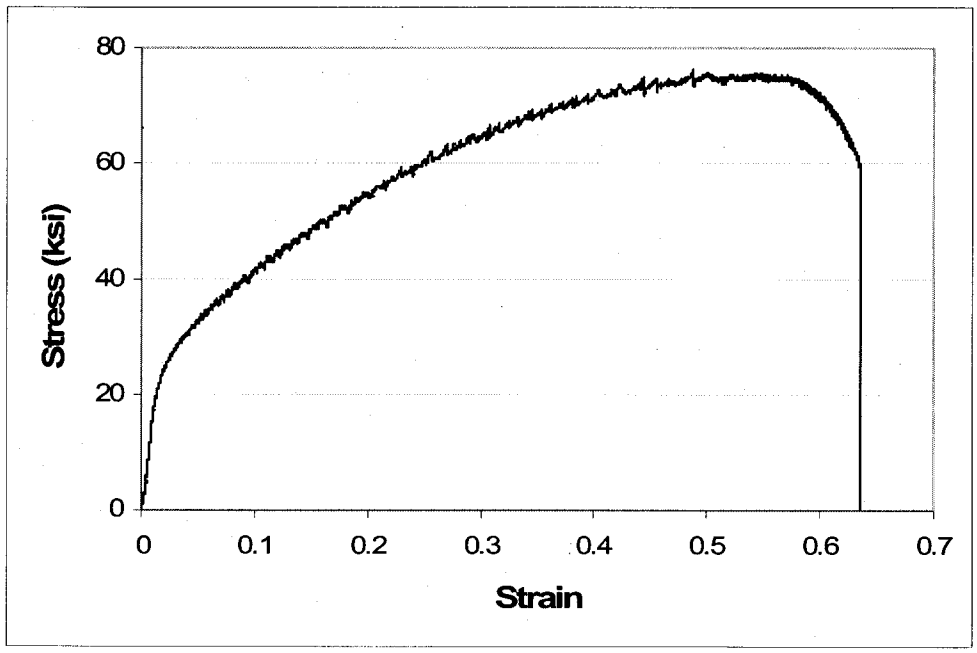

Sample 3

A.1.7. Stress-Strain curves at 600°C

A.1.7.1. Tested in MTS

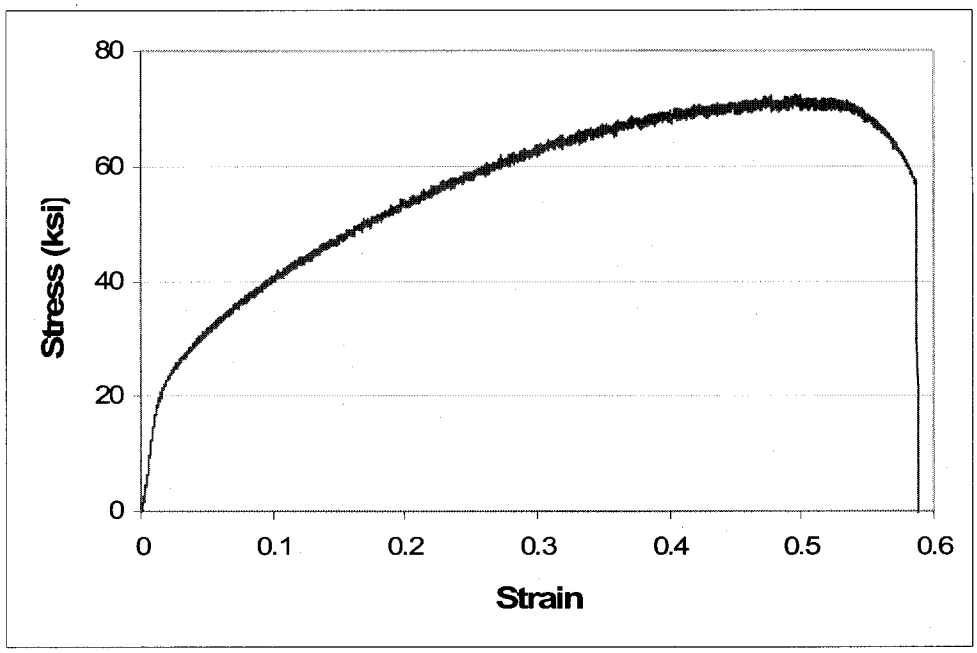

Sample 1

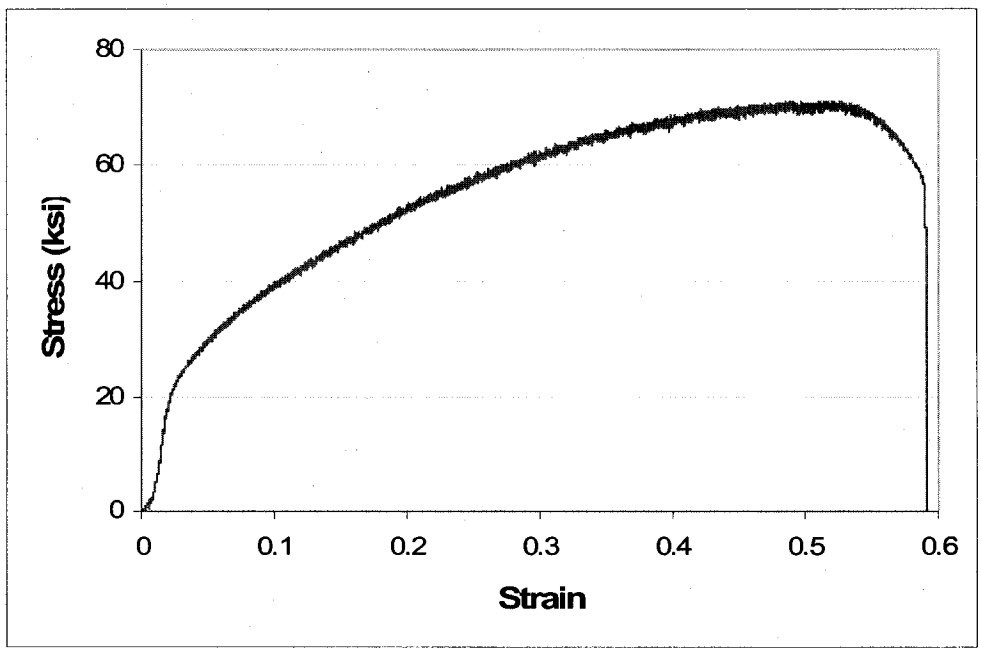

Sample 2

A.1.7.2. Tested in Instron

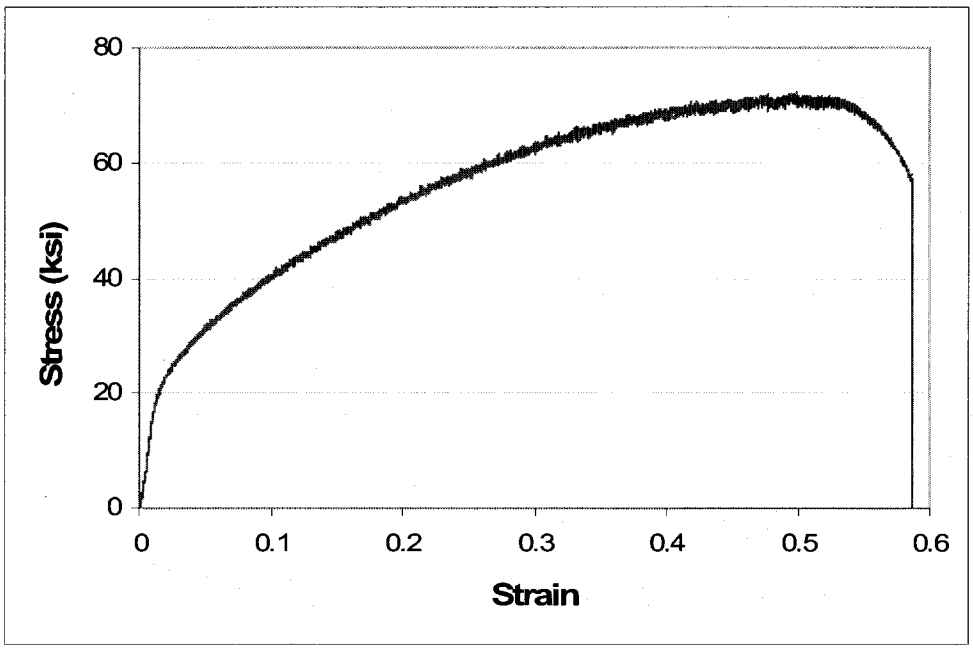

Sample 3

A.1.8. Stress-Strain curves at 700°C

A.1.8.1. Tested in Instron

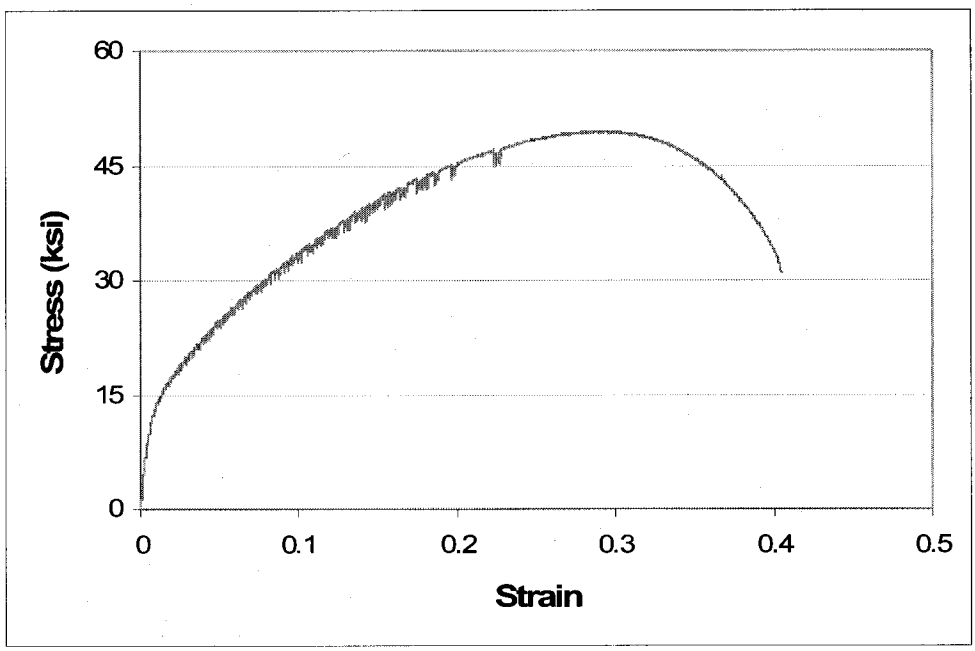

Sample 1

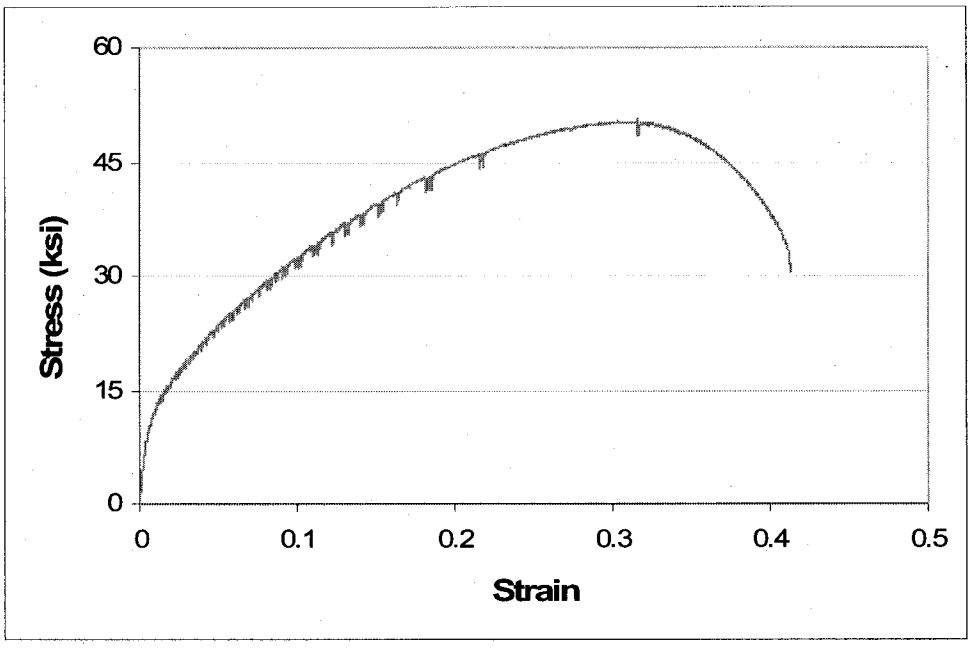

Sample 2

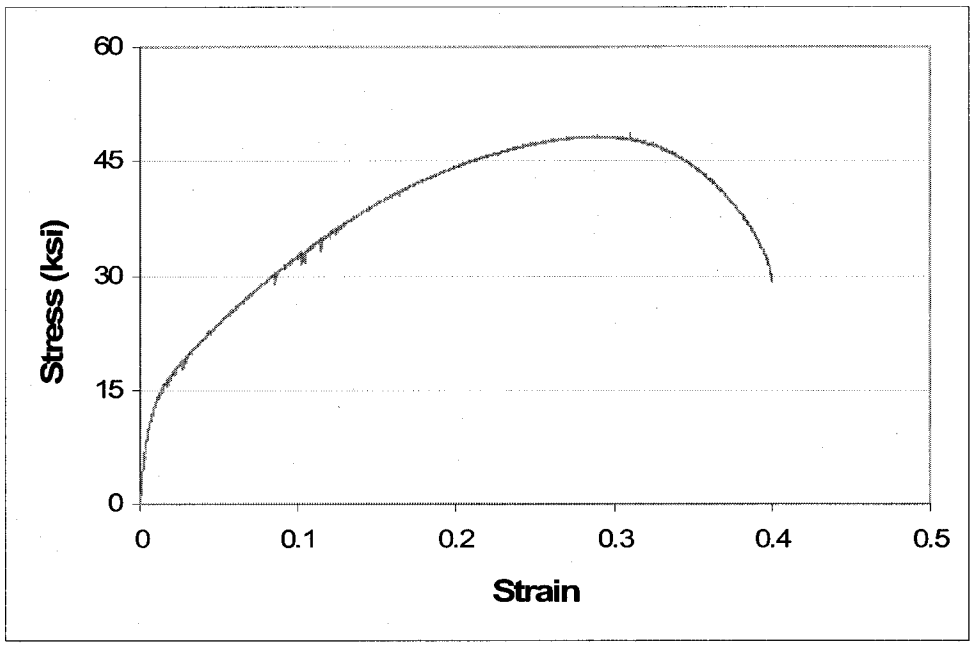

Sample 3

A.1.9. Stress-Strain curves at 800°C

A.1.9.1. Tested in Instron

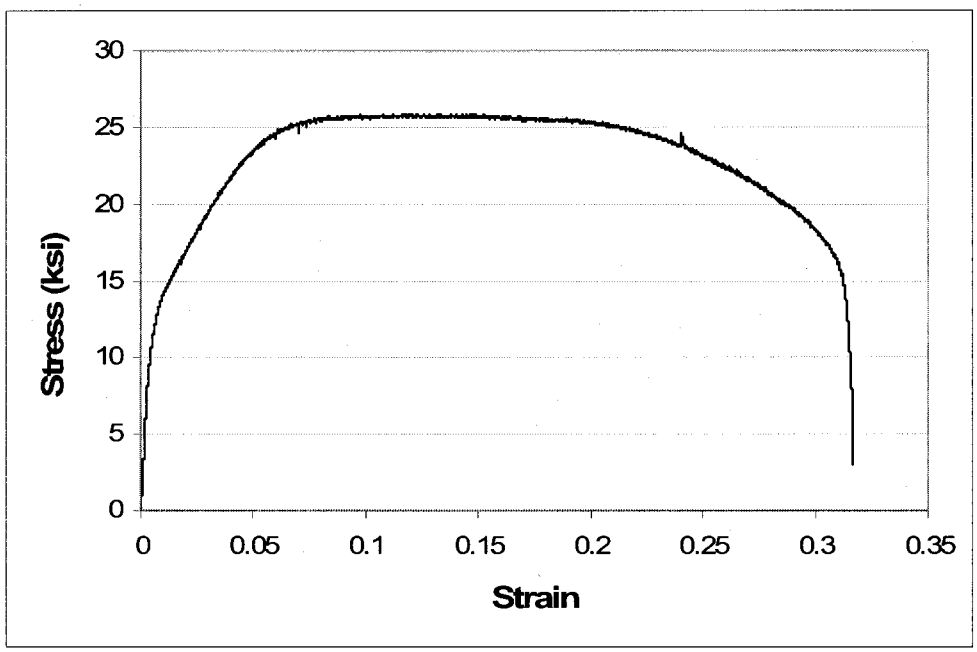

Sample 1

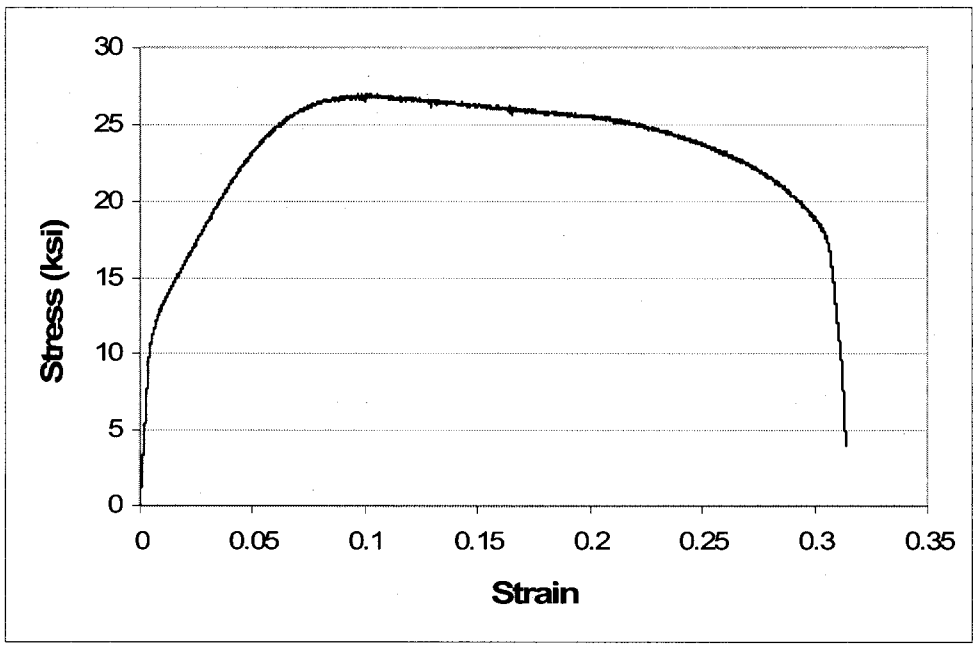

Sample 2

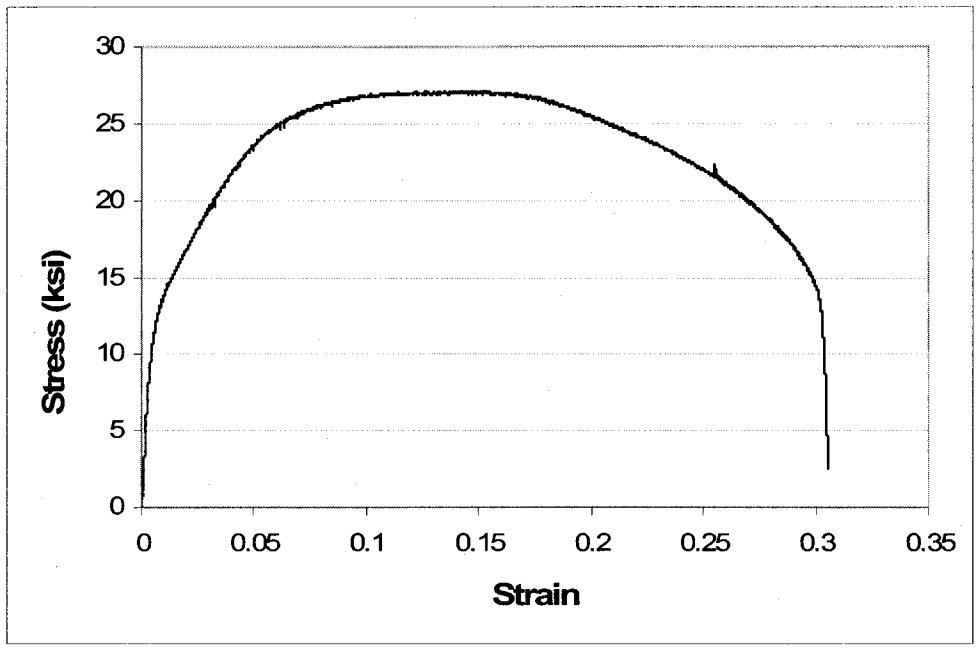

Sample 3

A.1.10. Stress-Strain curves at 1000°C

A.1.10.1. Tested in Instron

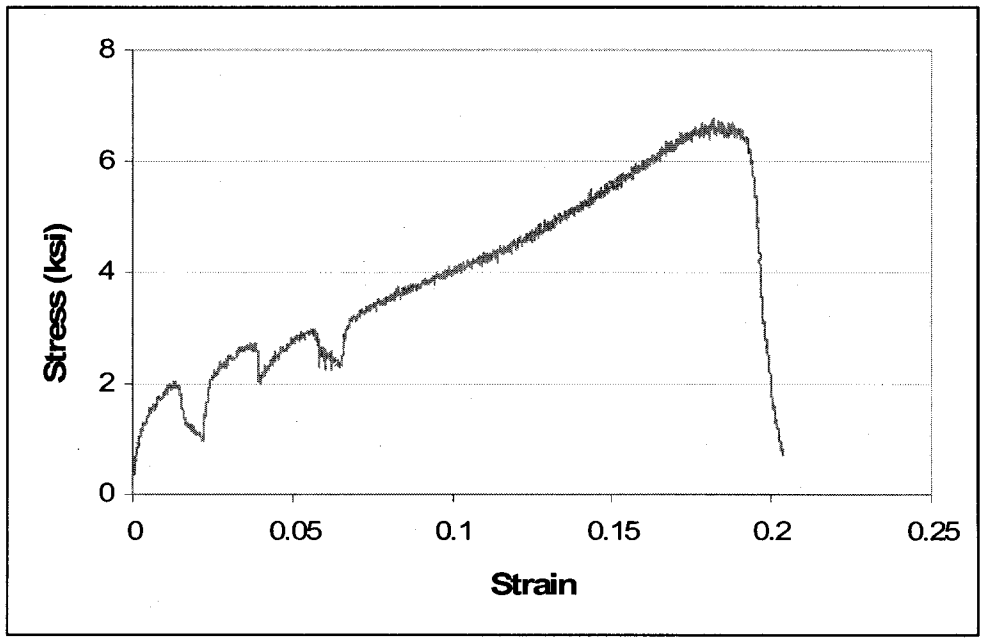

Sample 1

Table A.1. Combined Tensile Test Results for Alloy 800H

Test Temperature, °C	Sample #	YS, ksi	UTS, ksi	% El	% RA
Ambient	Sample 1	37.8	86.2	57.1	66.8
	Sample 2	38.5	85.9	59.2	66.8
	Sample 3	37.1	86.5	59.1	68.9
100	Sample 1	35.6	78.5	54.0	66.3
	Sample 2	35.3	79.4	53.8	66.5
	Sample 3	36.0	78.4	53.9	66.2
200	Sample 1	33.2	75.8	51.5	63.9
	Sample 2	32.9	76.0	53.2	64.0
	Sample 3	33.1	75.6	53.1	64.2
300	Sample 1	30.6	76.4	52.7	60.1
	Sample 2	31.0	76.9	56.8	62.4
	Sample 3	31.0	77.0	55.6	61.2
400	Sample 1	28.2	76.2	59.4	59.8
	Sample 2	26.9	76.5	60.3	58.1
	Sample 3	27.5	76.7	61.0	58.7
500	Sample 1	24.4	76.3	61.2	59.0
	Sample 2	24.6	76.2	59.9	56.1
	Sample 3	24.9	76.3	60.0	57.5
600	Sample 1	22.1	72.3	57.1	61.7
	Sample 2	22.2	71.2	56.9	61.9
	Sample 3	21.3	72.2	58.7	62.3
700	Sample 1	14.8	49.5	39.0	61.0
	Sample 2	14.7	50.8	39.5	61.7
	Sample 3	15.1	48.6	38.8	62.0
800	Sample 1	14.6	25.9	32.0	60.0
	Sample 2	14.3	27.0	31.8	60.7
	Sample 3	15.0	27.2	30.5	60.3
1000	Sample 1	1.5	6.85	21.0	10.0

APPENDIX B

SLOW-STRAIN-RATE TEST DATA

B.1. SSR Testing of Alloy 800H

B.1.1. SSR Testing in Air

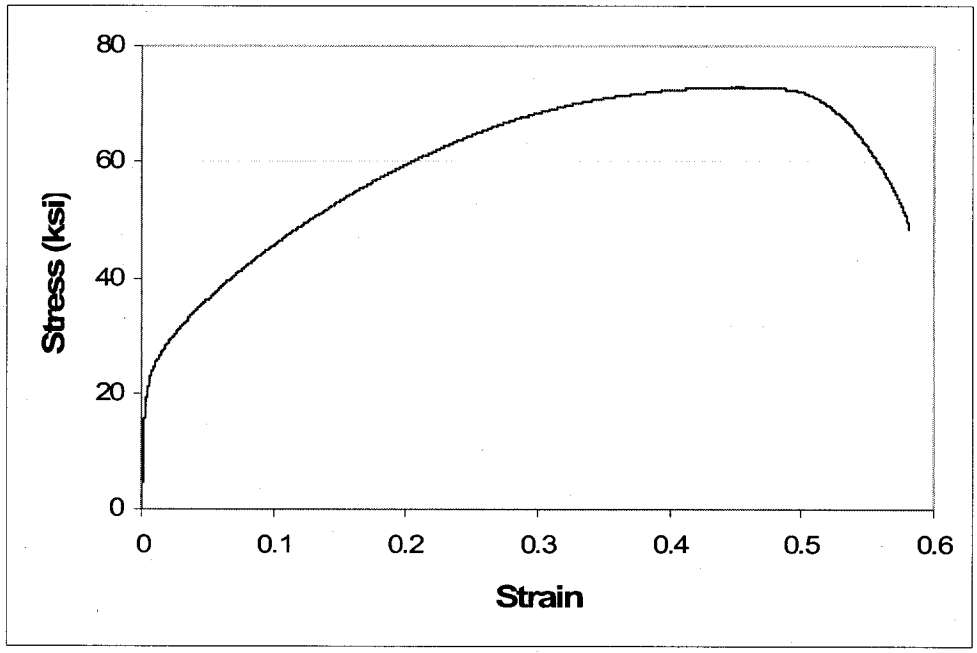

Sample 1

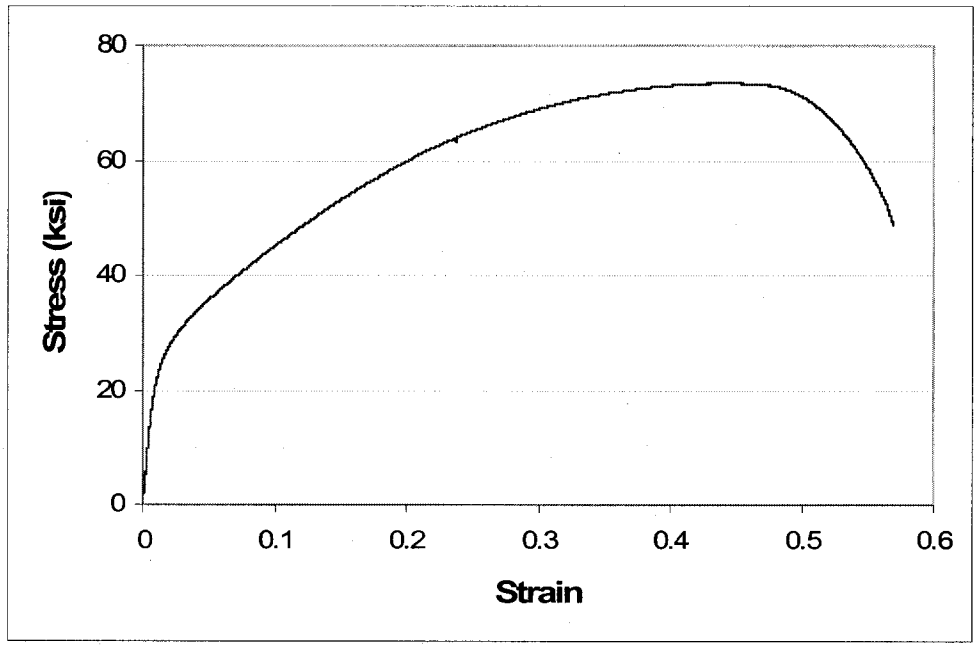

Sample 2

B.1.2. SSR Testing in Acidic solution at Ambient Temperature

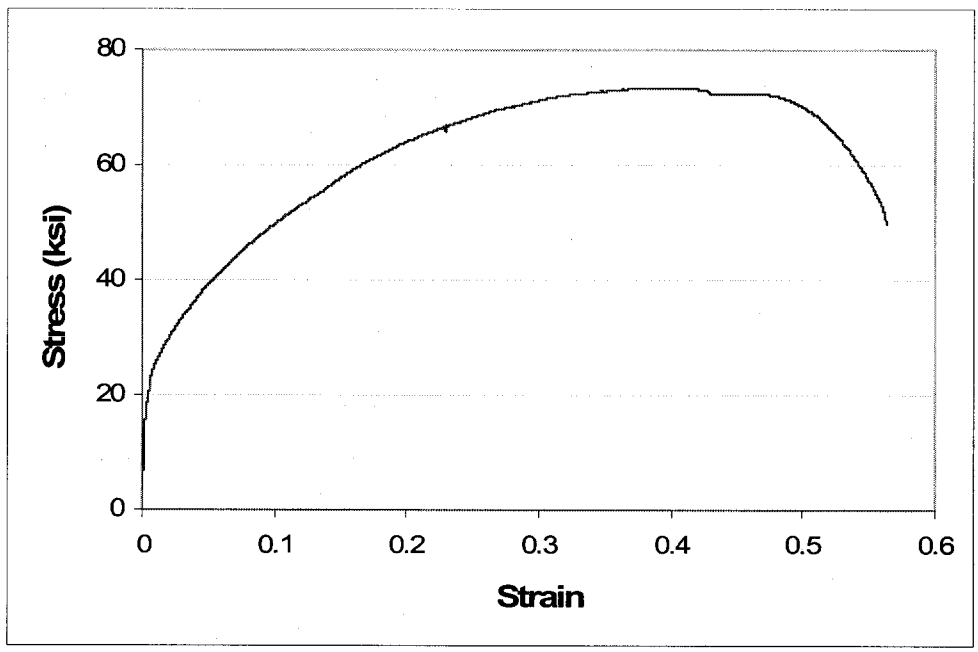

Sample 1

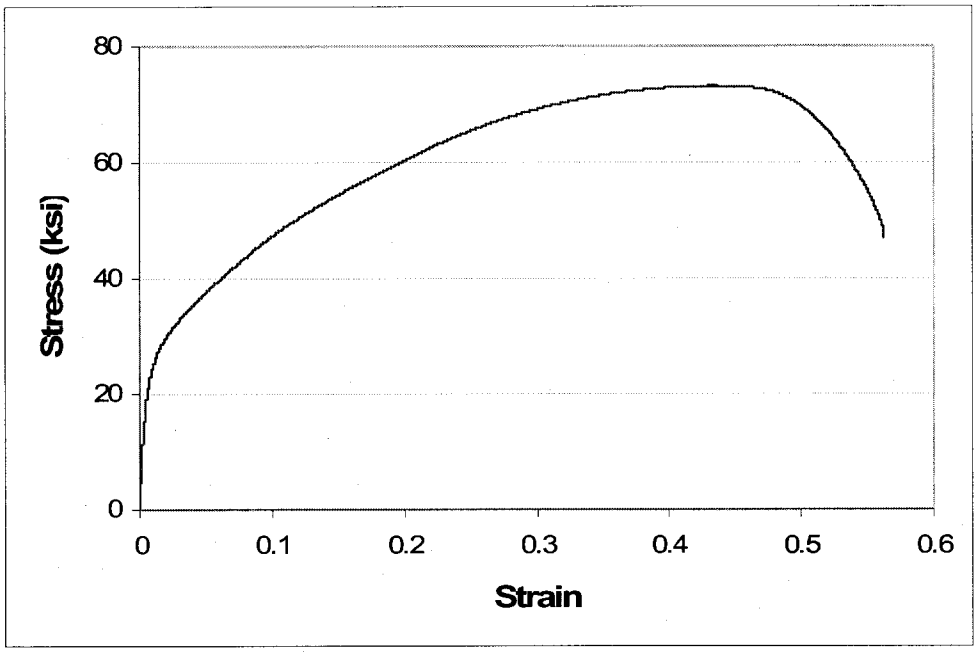

Sample 2

B.1.3. SSR Testing in Acidic solution at 60°C

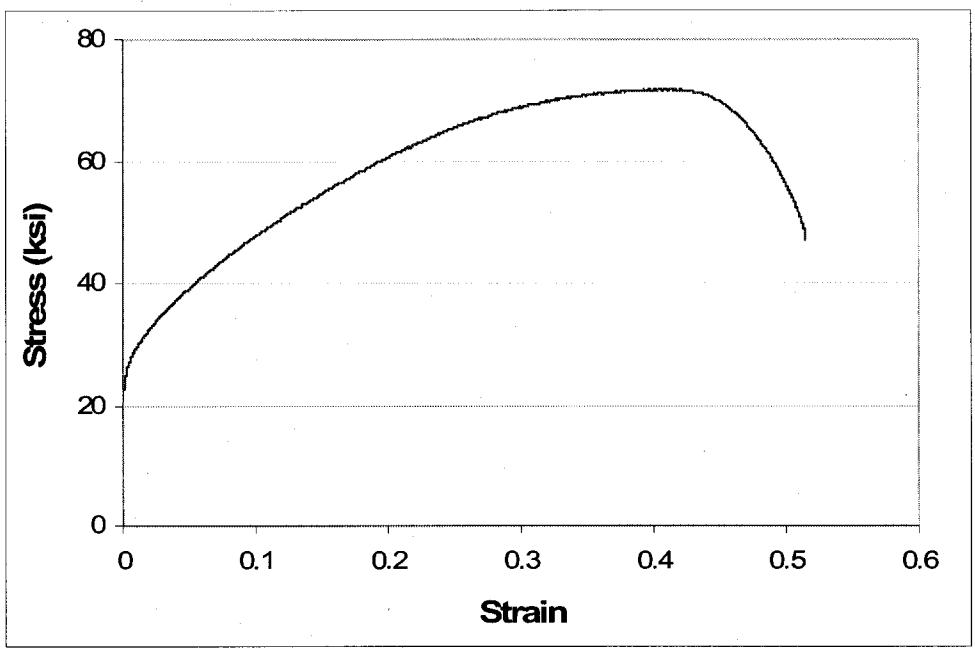

Sample 1

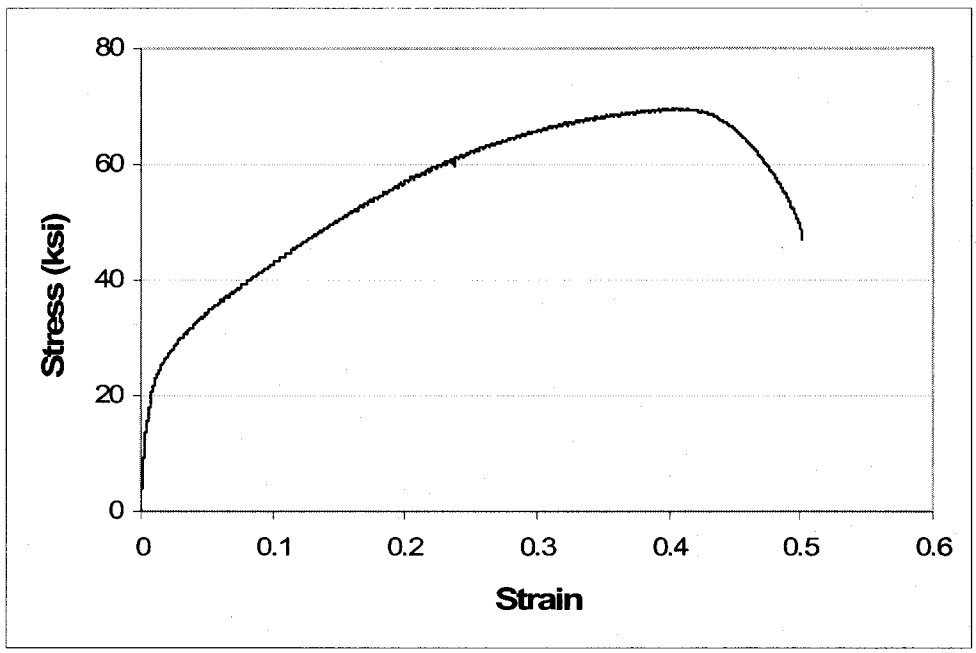

Sample 2

B.1.4. SSR Testing in Acidic solution at 90°C

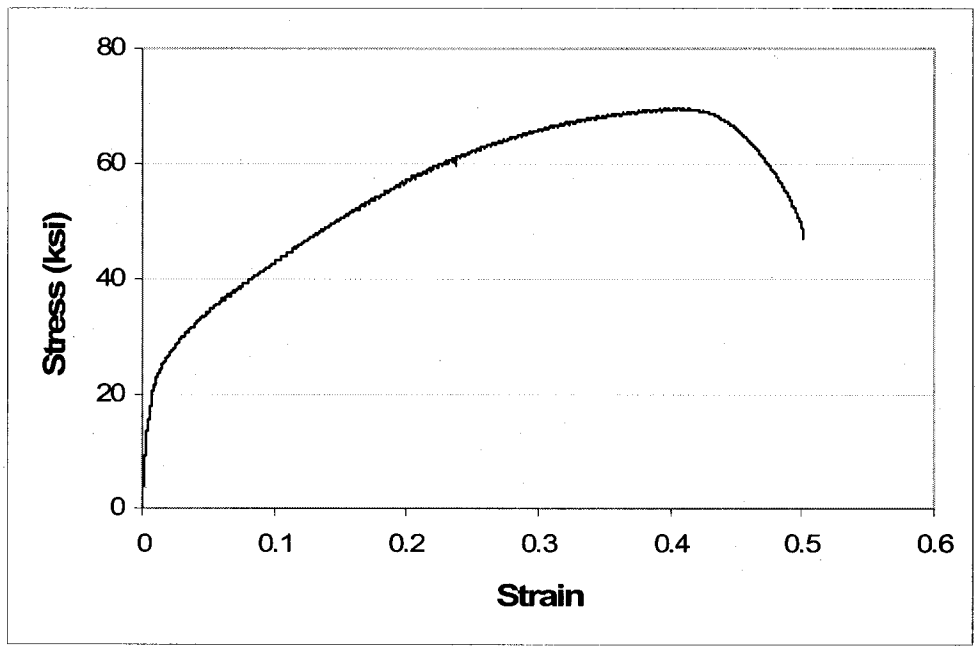

Sample 1

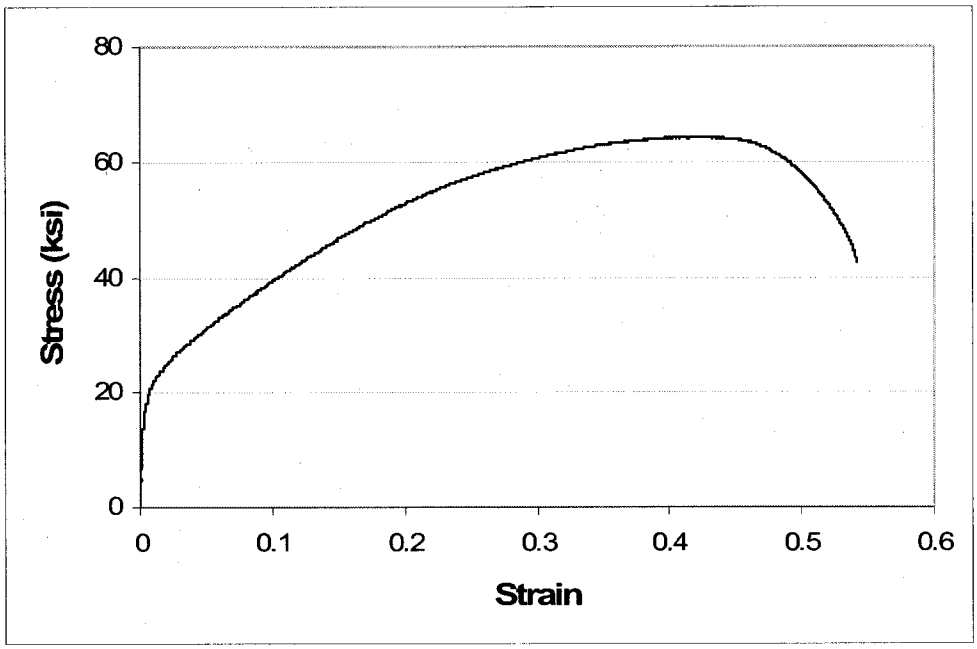

Sample 2

Table B.1. SSR Test Results of Alloy 800H (Smooth)

Environment / Temperature (°C)	Sample #	σ_f, ksi	% El	% RA	TTF, hrs
Air	Sample 1	154.0	58.4	68.4	50.6
	Sample 2	145.2	56.1	66.3	49.2
Acidic / RT	Sample 1	144.8	57.2	65.6	49.5
	Sample 2	141.0	56.2	66.5	48.8
Acidic / 60	Sample 1	130.4	55.1	65.8	47.6
	Sample 2	137.9	54.8	65.4	47.8
Acidic / 90	Sample 1	131.6	49.8	64.4	47.4
	Sample 2	132.6	54.0	64.0	47.4

RT: Room Temperature, Acidic: H_2SO_4 + NaI +H_2O

B.2. SSR Testing of Alloy 800H (Notched Specimen)

B.2.1. SSR Testing in Air

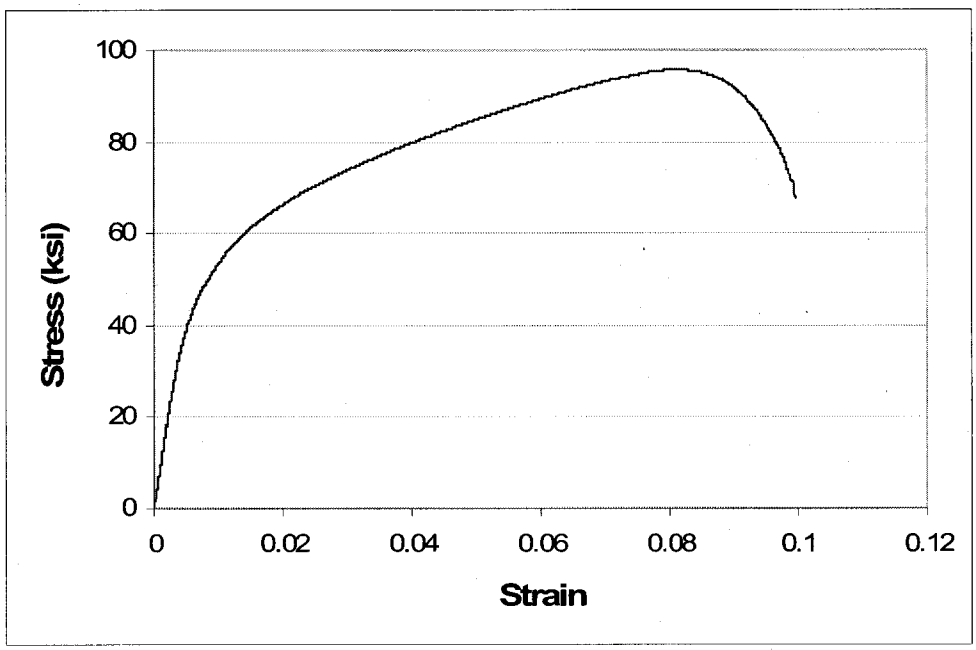

Sample 1

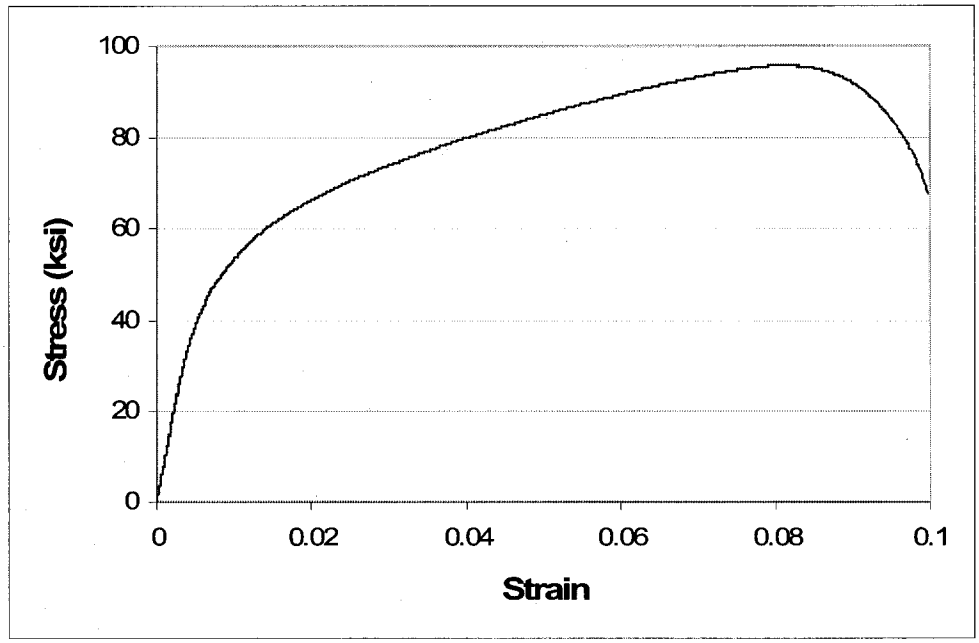

Sample 2

B.2.2. SSR Testing in Acidic solution at Ambient Temperature

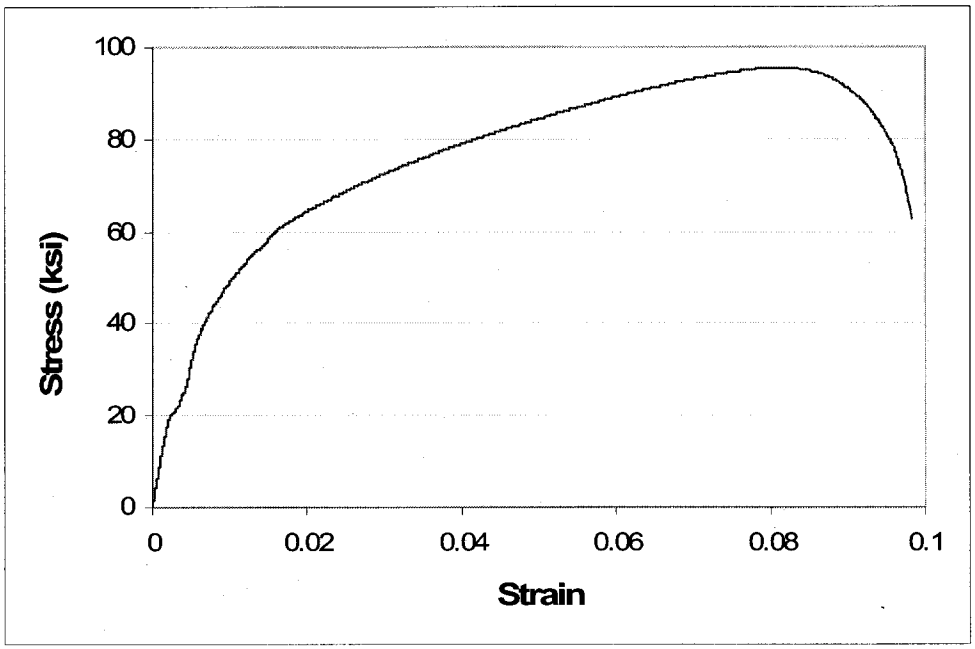

Sample 1

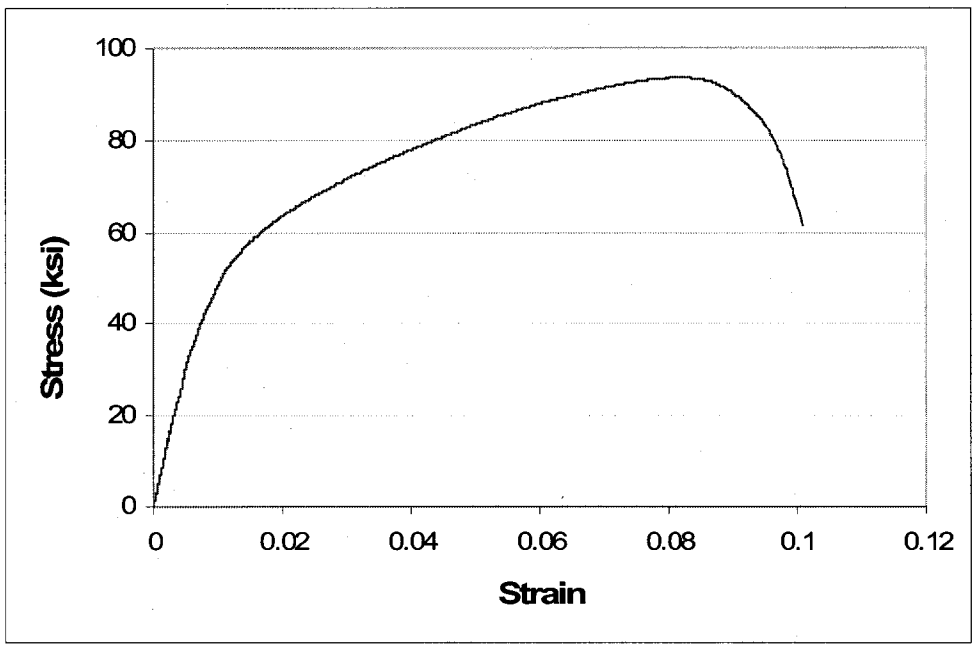

Sample 2

B.2.3. SSR Testing in Acidic solution at 60°C

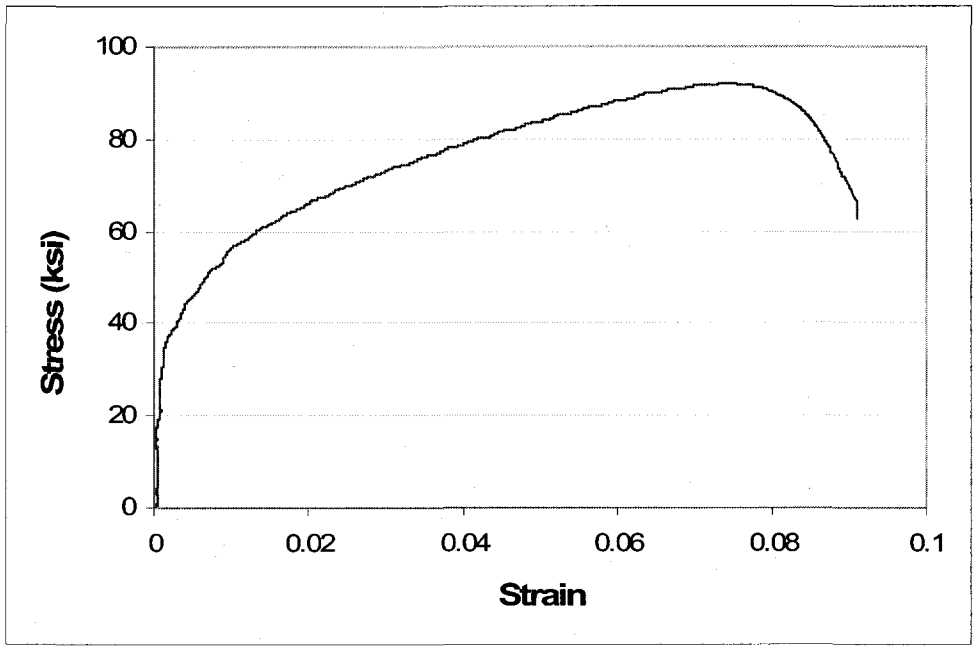

Sample 1

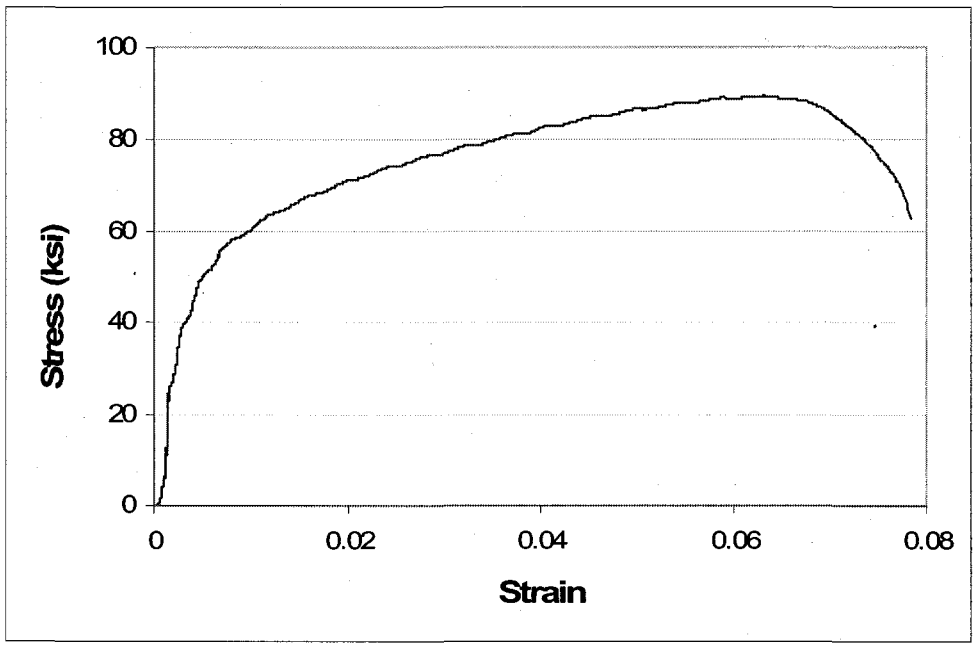

Sample 2

B.2.4. SSR Testing in Acidic solution at 90°C

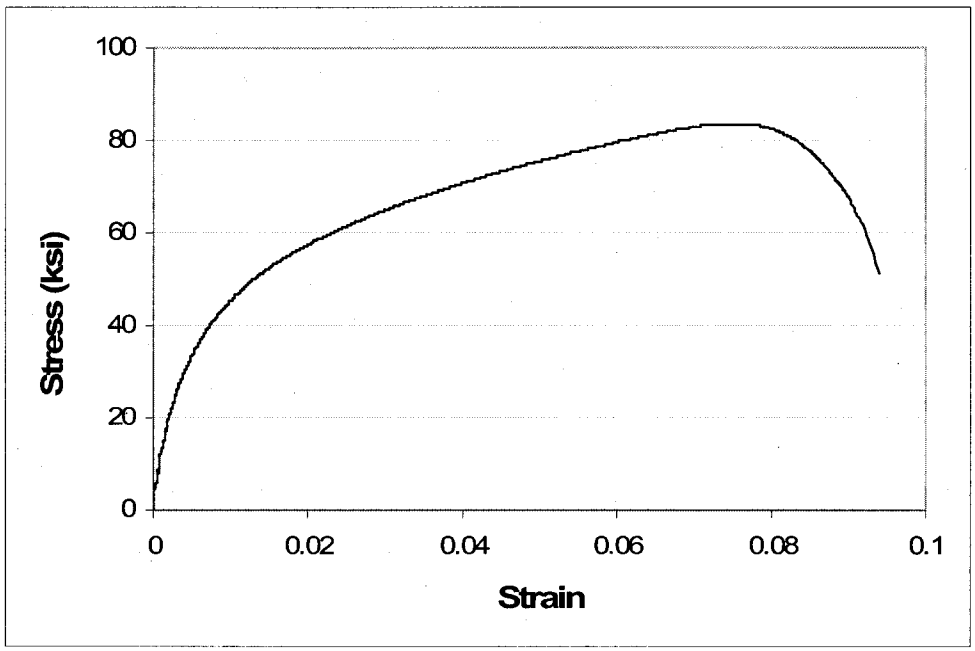

Sample 1

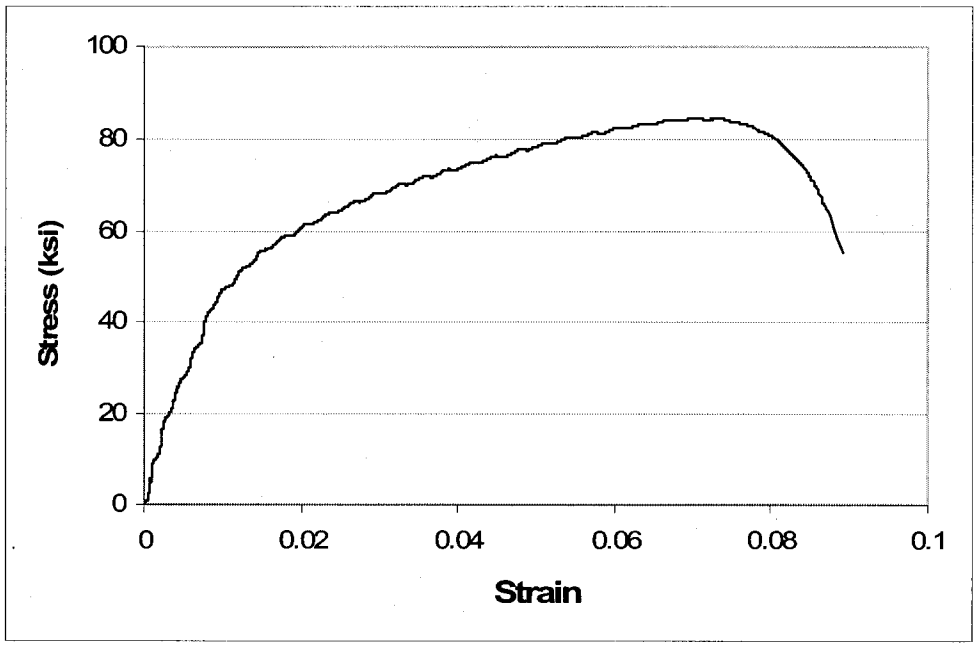

Sample 2

Table B.2. SSR Test Results of Alloy 800H (Notched)

Environment / Temperature (°C)	Sample #	s_f, ksi	% El	TTF, hrs	e_f
Air	Sample 1	67.6	9.9	9.4	0.099
	Sample 2	67.4	10.2	9.4	0.099
Acidic / RT	Sample 1	63.0	10.5	9.6	0.098
	Sample 2	62.8	10.5	9.4	0.098
Acidic / 60	Sample 1	63.0	10.4	9.3	0.094
	Sample 2	62.1	10.3	9.2	0.079
Acidic / 90	Sample 1	56.0	10.0	9.0	0.092
	Sample 2	55.7	10.1	9.2	0.089

RT: Room Temperature, Acidic: H_2SO_4 + NaI +H_2O

APPENDIX C

CYCLIC POTENTIODYNAMIC POLARIZATION TEST DATA

C.1. CPP curves for Alloy 800H

C.1.1. CPP diagrams at 30°C

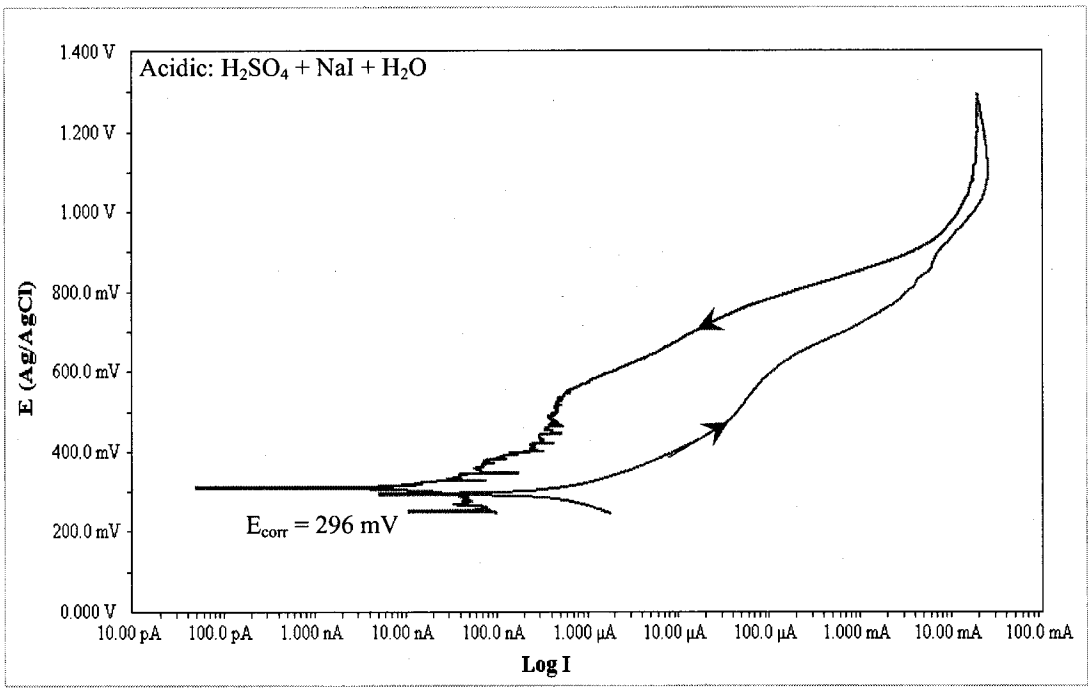

Sample 1

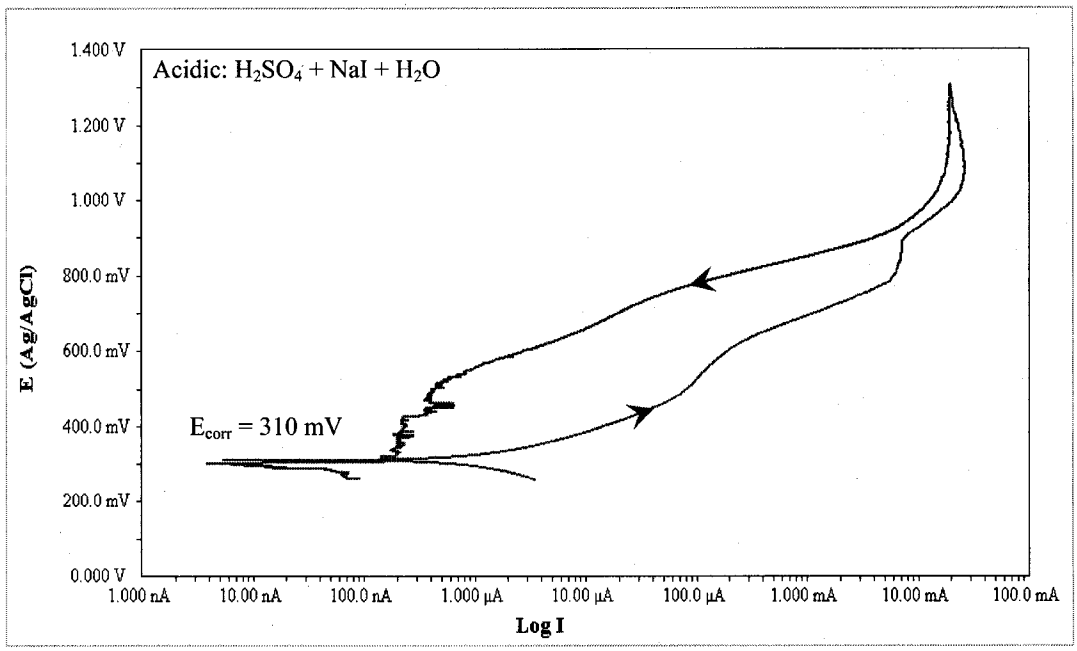

Sample 2

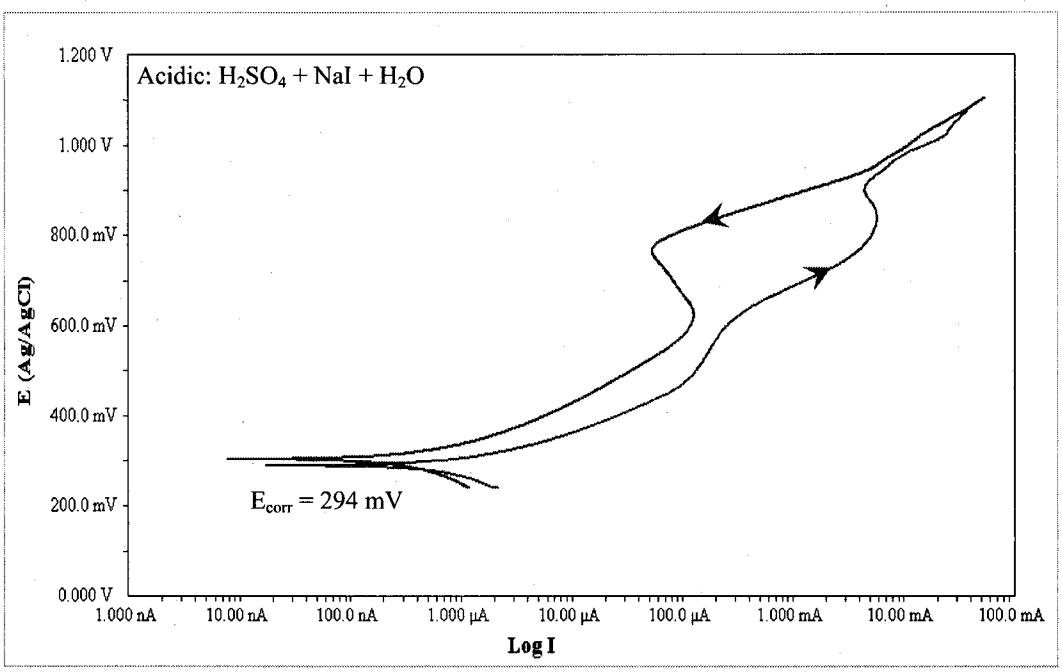

Sample 3

C.1.2. CPP diagrams at 60°C

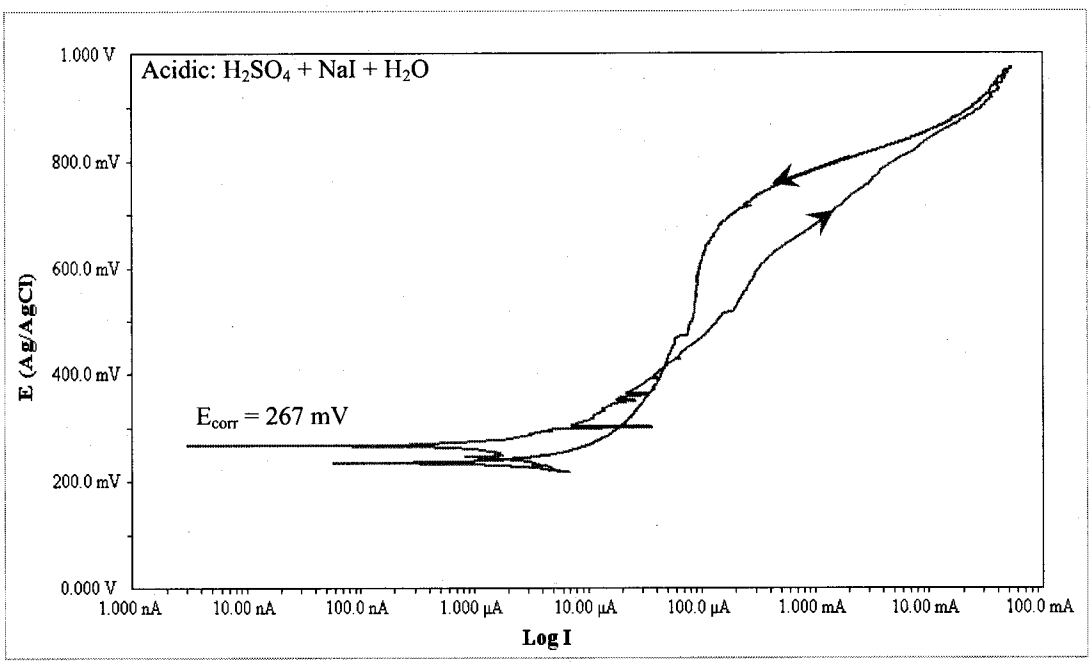

Sample 1

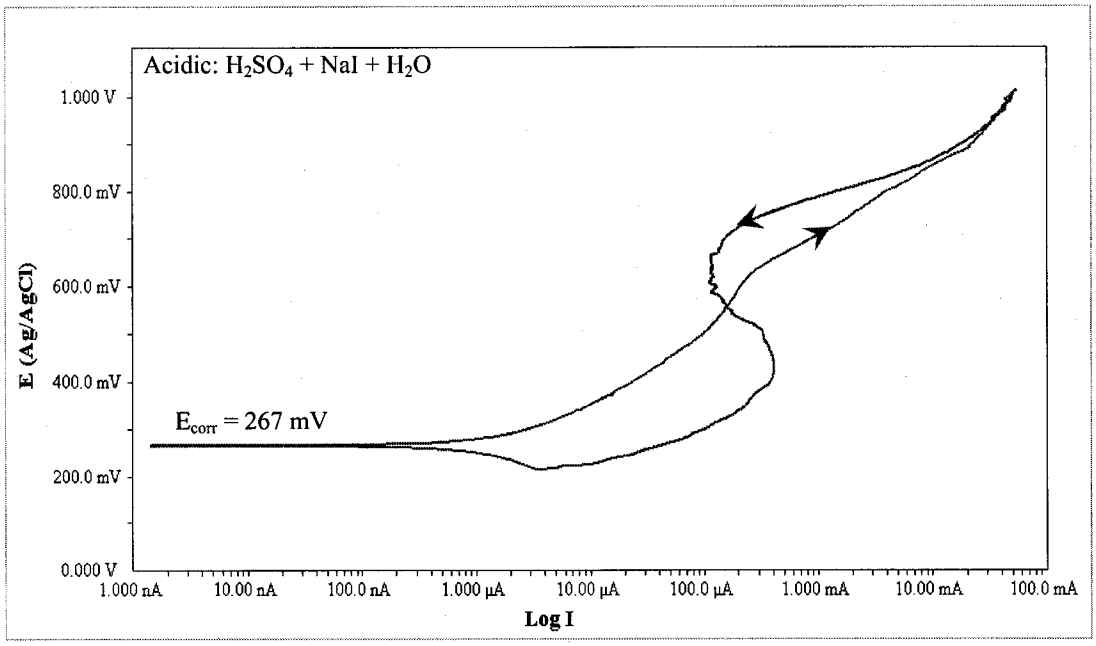

Sample 2

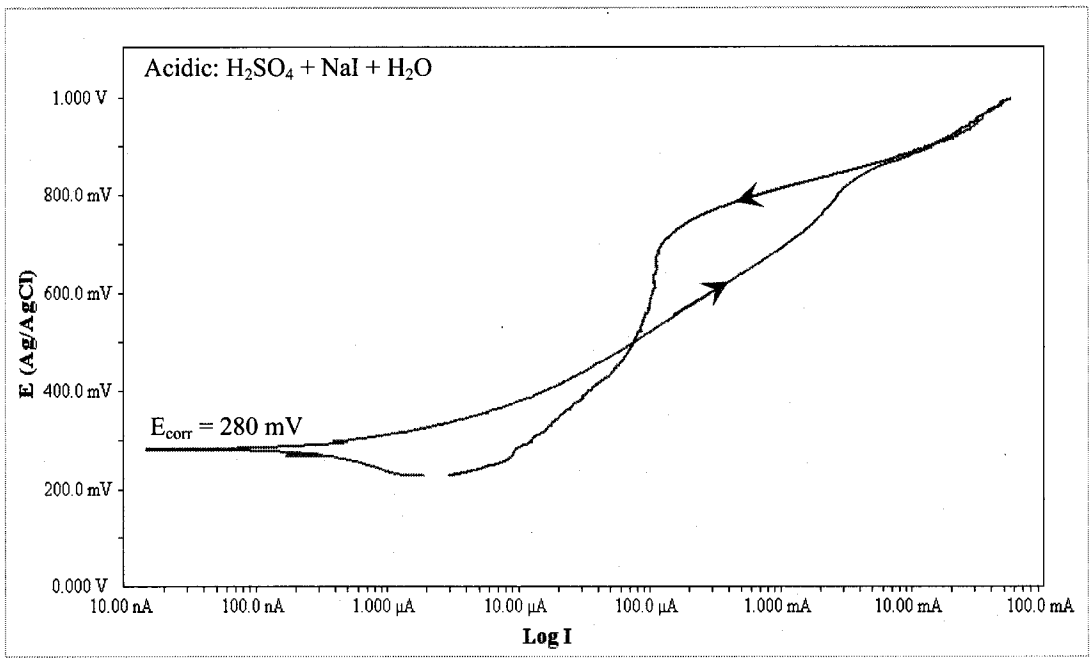

Sample 3

C.1.3. CPP diagrams at 90°C

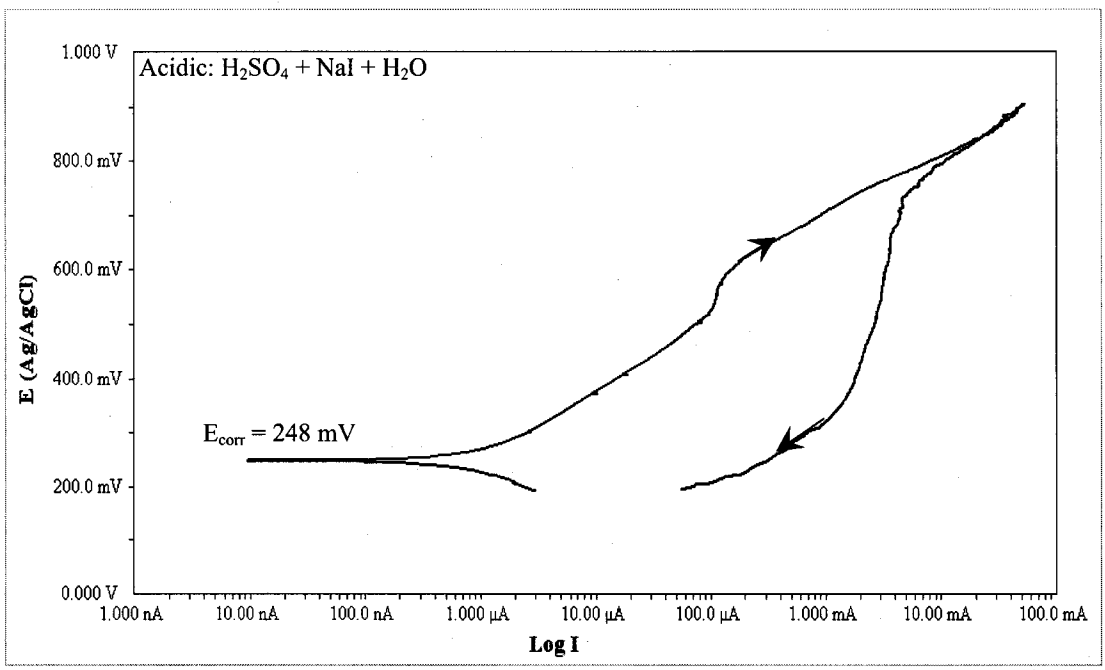

Sample 1

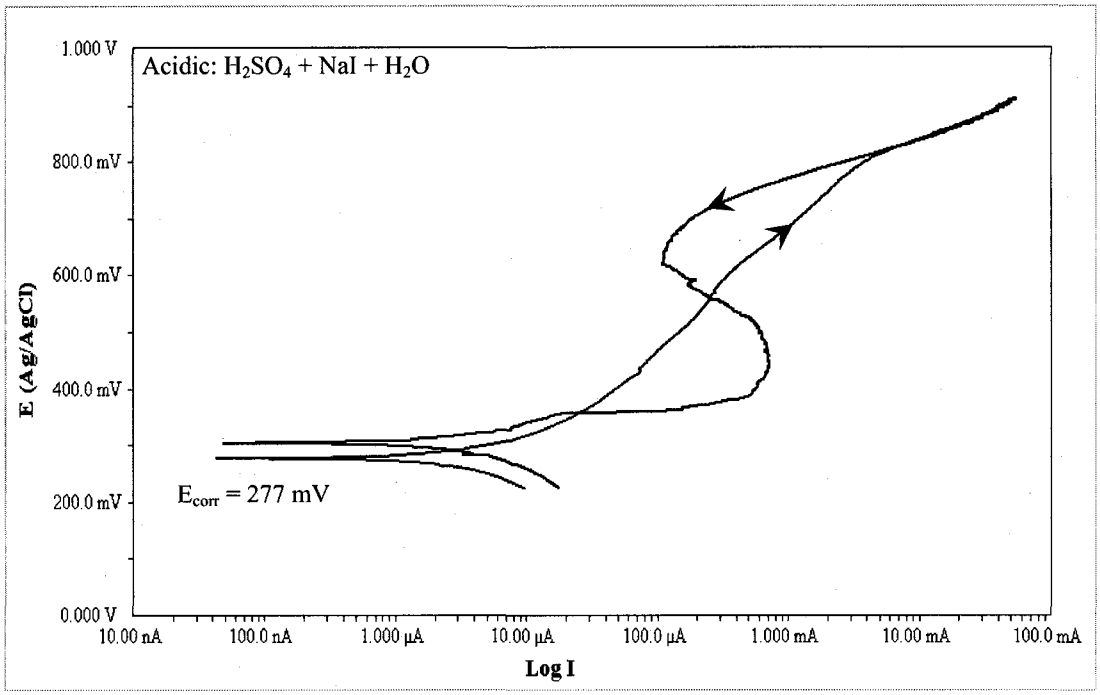

Sample 2

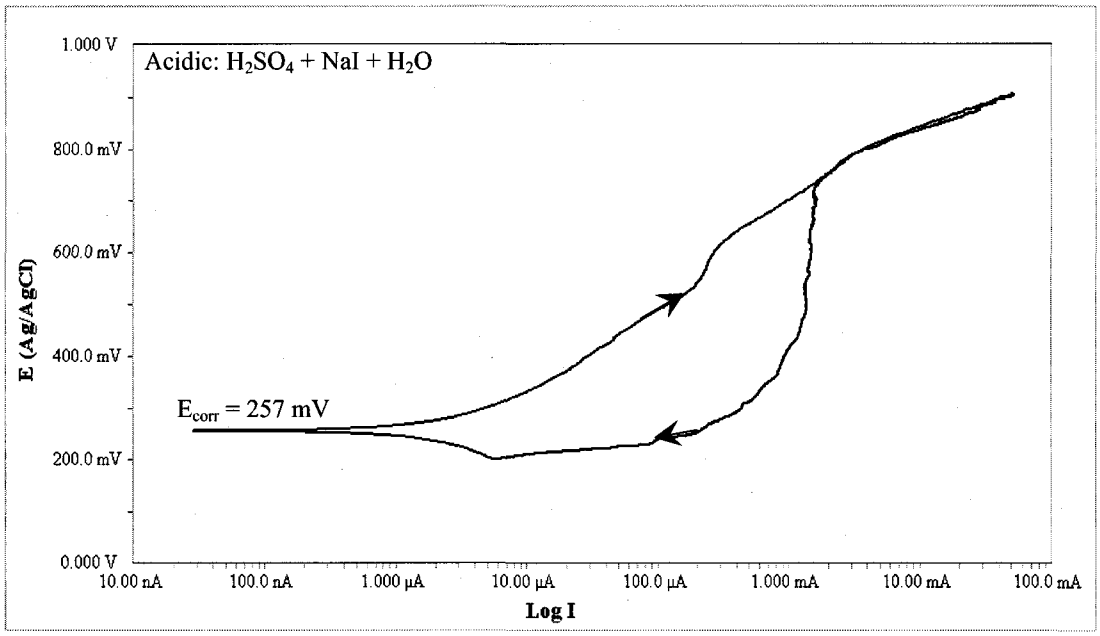

Sample 3

Table C.1. Critical Potentials for Alloy 800H

Test Temperature, °C	Sample #	E_{corr}, mV	E_{pit}, mV
30	Sample 1	296	615
	Sample 2	310	624
	Sample 3	294	620
60	Sample 1	267	608
	Sample 2	267	609
	Sample 3	280	615
90	Sample 1	248	595
	Sample 2	277	597
	Sample 3	257	601

APPENDIX D

SSR UNDER CONTROLLED POTENTIAL TEST DATA

Zr705 specimens were subjected to SSR testing under both cathodic and anodic controlled potential (E_{cont}) testing. All E_{cont} tests were conducted at room temperature in an acidic solution (pH~1) containing sodium iodide, sulfuric acid and deionized water.

D.1. CATHODIC CONTROL POTENTIAL DATA

D.1.1. E_{cont} at -300mV with respect to E_{corr}

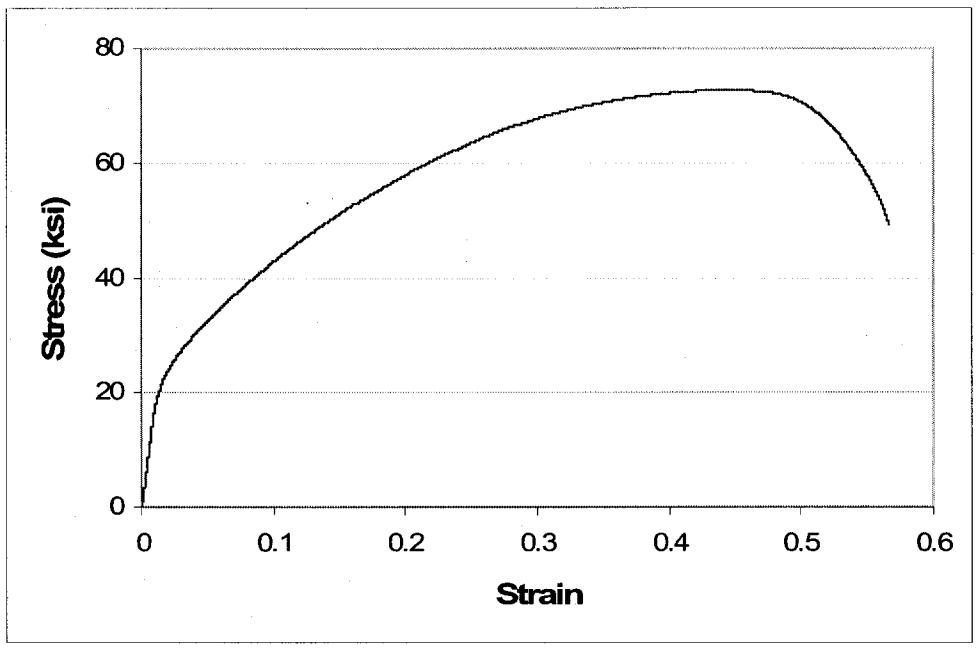

Sample 1

D.1.2. E_{cont} at -500mV with respect to E_{corr}

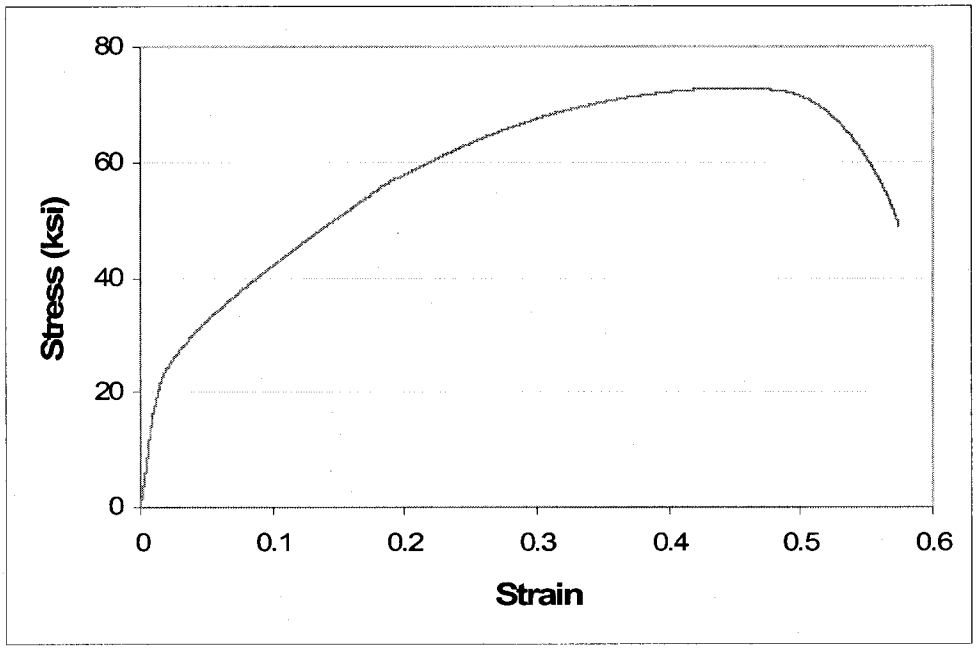

Sample 1

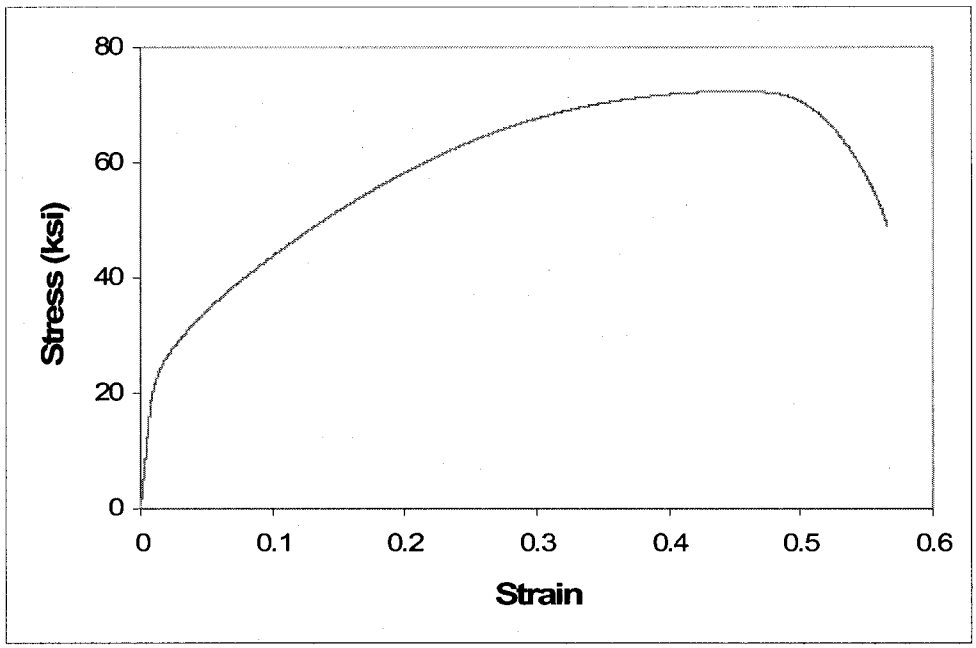

Sample 2

Table D.1. SCC Parameters under Cathodic E_{cont}

Sample #	E_{cont}, mV	σ_f, ksi	%El	%RA	TTF, hrs
Sample 1	20	142.8	55.9	65.6	48.8
Sample 1	-220	138.8	56.0	64.8	48.9
Sample 2	-220	144.6	56.0	67.0	48.9

D.2. ANODIC CONTROL POTENTIAL DATA

D.2.1. E_{cont} at +100mV with respect to E_{pit}

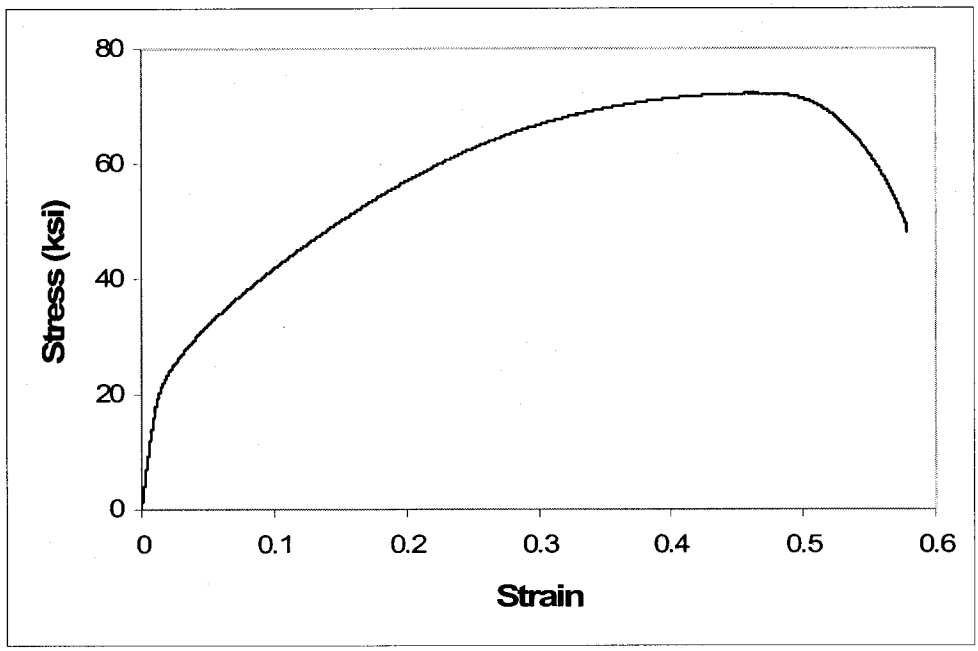

Sample 1

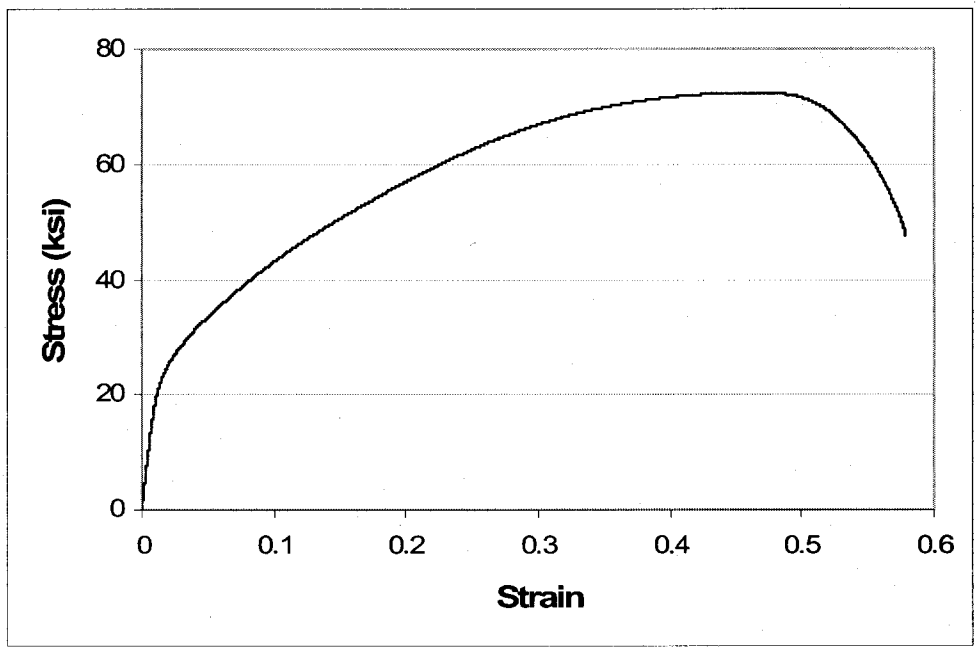

Sample 2

D.2.2. E_{cont} at +300mV with respect to E_{pit}

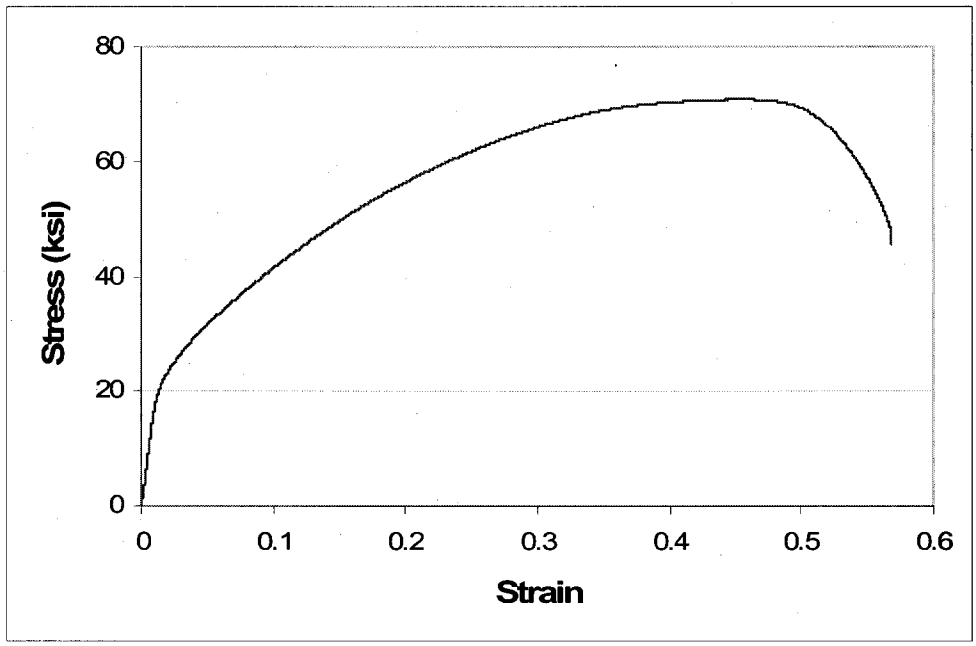

Sample 1

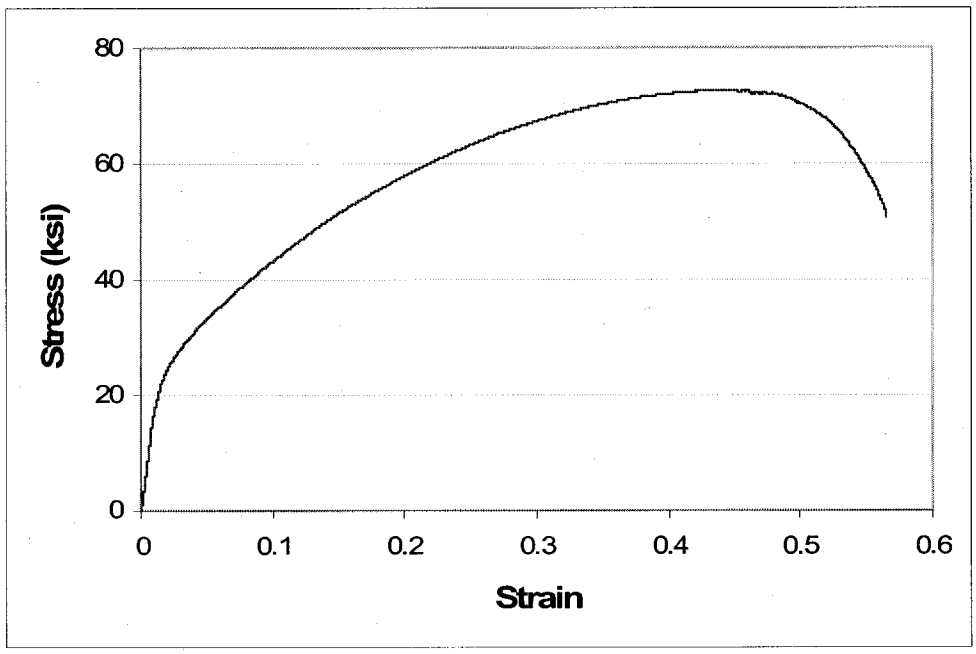

Sample 2

D.2.3. E_{cont} at +400mV with respect to E_{pit}

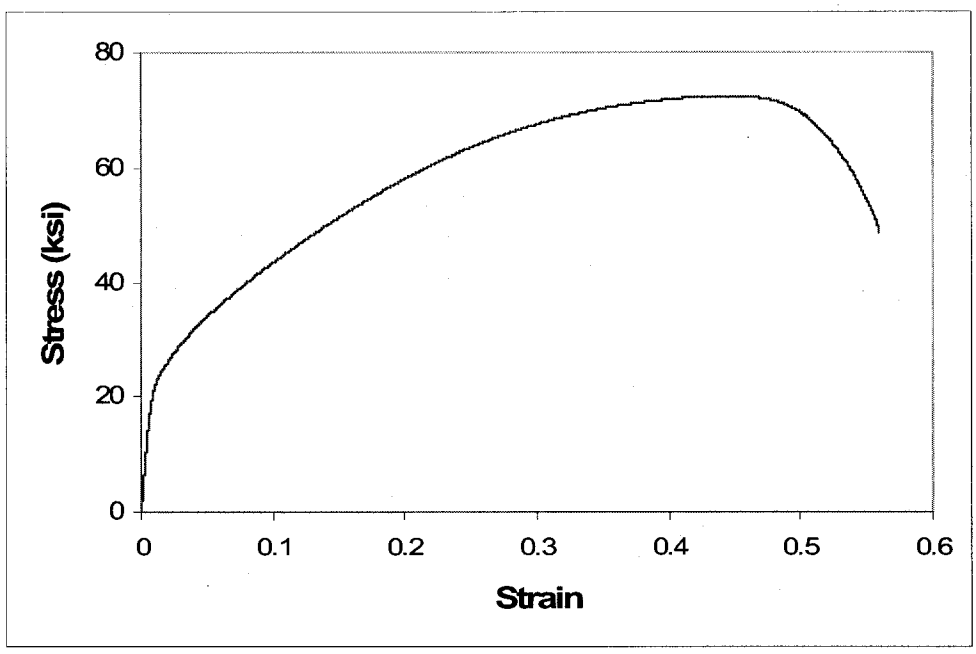

Sample 1

D.2.4. E_{cont} at +600mV with respect to E_{pit}

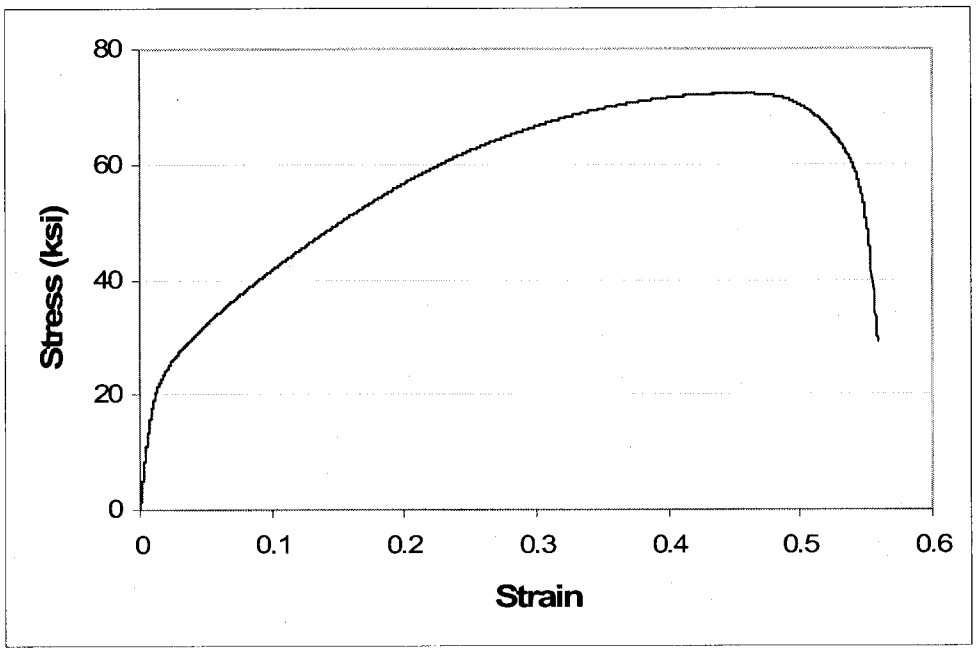

Sample 1

Table D.2. SCC Parameters under Anodic E_{cont}

Sample #	E_{cont}, mV	σ_f, ksi	%El	%RA	TTF, hrs
Sample 1	700	151.9	57.5	68.4	49.1
Sample 2	700	150.8	56.3	68.5	49.0
Sample 1	900	140.6	55.9	66.8	48.3
Sample 2	900	148.8	55.2	66.8	48.4
Sample 1	1000	134.6	56.0	66.1	48.2
Sample 1	1200	76.2	54.5	61.9	46.7

APPENDIX E

UNCERTAINTY ANALYSES

In any experiment, there is direct measurement of quantities like lengths, times etc. The instruments used to determine these measurements may vary in quality every time it is being used. Also, the parameters that are out of control of the researcher might cause undesired variations in these measurements. These measured values are then used to perform calculations to determine the experimental results that are compared with other experimental results and/or with the predictions of theories. Efforts were taken at materials performance laboratory (MPL) to repeat all the experiments in order to determine an average value. However, the undesired variations might have caused variations in the derived results. These variations if caused by the machines used in the experiments can be reduced by calibrating them on a timely basis. However the variations caused due to human errors and environmental factors cannot be avoided. Uncertainty analysis of these derived results determines the variations/errors in them.

In this section, a model developed by Kline and McClintock is being used to calculate the uncertainties. This method is known to be one of the precise methods to estimate uncertainties in experimental results, since it considers careful specifications of the uncertainties in all levels of the experimental measurements [97]. If for example, the slow-strain-rate experimental setup used in this investigation has a maximum load-cell reading of 7500lbs, but has a variation of $\pm$ 0.3% lbs. Thus, it can be said that the reading

on the load scale is uncertain to some extent which is expressed as a deviation either in the positive side or the negative side from the standard maximum value. Periodical and frequent calibration of the instrument may reduce this uncertainty. It should however, be noted that the level of uncertainty is also dependent on the calibration standard. Calibration of instruments using high-precision standards will lead to lower level of uncertainty compared to that performed using gages or instruments of unknown calibration.

All the experimental setups at MPL were calibrated on a timely basis ensuring that the uncertainties in the results derived are expected to be in the lower level. However, in order to prove this, the equation suggested by Kline and McClintock for uncertainty analysis was considered as shown below. The uncertainty levels calculated in this section are based on this relationship.

$$W_R = \left[\left(\frac{\partial R}{\partial x_1} w_1 \right)^2 + \left(\frac{\partial R}{\partial x_2} w_2 \right)^2 + \cdots + \left(\frac{\partial R}{\partial x_n} w_n \right)^2 \right]^{\frac{1}{2}} \qquad \text{(E.1)}$$

Where, W_R = Uncertainty in the results

R = Given function of the independent variables $x_1, x_2, \ldots\ldots x_n$)

$R = R(x_1, x_2, \ldots\ldots x_n)$

$w_1, w_2, \ldots\ldots w_n$ = Uncertainty in the independent variables

E.1. Uncertainty Calculation for Parameters Derived from MTS Results

As indicated earlier, most of the tensile testing was performed on the Materials Testing System (MTS). The results generated from this machine included calculation of stress (σ), percent elongation (%El), and percent reduction in area (%RA). The stress calculated was based on the measured load (P) and the initial cross-sectional area (A_i) of the tested specimen using the equation E.2. The %El was based on the change in length, (Δl= difference of final length (L_f) and initial length (L_i) of the specimen) after the testing and the %RA is based on the initial and final cross-sectional areas (A_i and A_f). The magnitude of P was obtained from the load-cell of the MTS unit. However, the values for L_f, L_i A_i, and A_f were calculated based on measurements by a caliper. The uncertainties in load-cell and caliper were ± 0.03% lbs and ± 0.001 in, respectively, as obtained from the calibration. The uncertainty in the initial notched diameter of the notched cylindrical specimen was ± 0.001, which was provided by the manufacturer, and the uncertainty in the final notched diameter was ± 0.001 which was obtained by the caliper used.

$$\sigma = \frac{P}{A_i} \qquad \text{(E.2)}$$

Where P = load

A_i = initial Area

E.1.1. Calculation of Uncertainty in Stress (U_σ)

$$U_\sigma = U_{(P,\, Ai)}$$

$$U_{Ai} = (U_{Di})^2$$

Uncertainty in load-cell = ± 0.03% lbs

Uncertainty in caliper = ± 0.001 in

Sample calculation:

For yield stress (YS) = 39.80 ksi

The measured P = 1961.5 lbs

Uncertainty in load (U_p) = 1961.5*0.0003 = ± 0.5885 lbs

Uncertainty in cross-sectional area (U_{Ai}) for the smooth specimen:

Measured initial Diameter (D_i) = 0.2505 in

Uncertainty in diameter (U_{Di}) = ± 0.001 in

$$Area(A_i) = \frac{\pi D_i^2}{4} = 0.0493 \text{ in}^2$$

$$\frac{dA_i}{dD_i} = \frac{\pi D_i}{2} = 0.393 \text{ in}$$

Uncertainty in area,

$$U_{Ai} = \left[\left(\frac{dA_i}{dD_i} \cdot U_{D_i}\right)^2\right]^{\frac{1}{2}}$$

$$= 0.393*0.001 \text{ in}^2$$

$$= \pm 0.000393 \text{ in}^2$$

Uncertainty in stress,

$$U_\sigma = \left[\left(\frac{\partial \sigma}{\partial P} \cdot_u P\right)^2 + \left(\frac{\partial \sigma}{\partial A_i} \cdot_u A_i\right)^2\right]^{\frac{1}{2}} \quad \text{(E.3)}$$

$$\frac{\partial \sigma}{\partial P} = \frac{1}{A_i} = 20.284$$

$$\frac{\partial \sigma}{\partial A_i} = -\frac{p}{A_i^2} = -807038.9098$$

Substituting these values in equation E.3,

$$U_\sigma = \left[(20.284 * 0.5885)^2 + (807038.9098 * 0.000393)^2\right]^{\frac{1}{2}}$$

$$= 317.39 \text{ psi}$$

$$= \pm 0.317 \text{ ksi}$$

E.1.2. Calculation of Uncertainty in Percentage Elongation ($U_{\%El}$)

Sample calculation:

Change in length (Δl) = 0.5711 in

Gage length (l) = 1.00 in

$$\%El = \frac{\Delta l}{l} * 100$$

Uncertainty in Δl ($U_{\Delta l}$) $= \pm 0.001$ in

Uncertainty in %El ($U_{\%El}$),

$$U_{\%El} = \left[\left(\frac{d\%El}{d\Delta l}_{,u} \Delta l\right)^2\right]^{\frac{1}{2}} \quad \text{(E.4)}$$

$$\frac{d\%El}{d\Delta l} = \frac{100}{l}$$

$$= 100$$

Substituting the values in equation E.4,

$$U_{\%El} = \left[(100 * 0.001)^2\right]^{\frac{1}{2}}$$

$U_{\%EL} = \pm 0.1$ in

E.1.3. Calculation of Uncertainty in Percentage Reduction in Area ($U_{\%RA}$)

Sample calculation:

For %RA = 66.77%

From section E.1,

Uncertainty in initial cross-sectional area (U_{Ai}) = ± 0.000393 in

Uncertainty in final cross-sectional area (U_{Af}),

Final Diameter (D_f) = 0.1444 in

Uncertainty in final diameter (U_{Df}) = ± 0.001 in

$$\text{Area } (A_f) = \frac{\pi D_f^{\,2}}{4}$$

$$= 0.0164 \text{ in}^2$$

$$\frac{dA_f}{dD_f} = \frac{\pi D_f}{2}$$

$$= 0.227$$

Uncertainty in final cross-sectional area,

$$U_{A_f} = \left[\left(\frac{dA_f}{dD_f} * U_{D_f} \right)^2 \right]^{\frac{1}{2}}$$

$$= 0.227 * 0.001 \text{ in}^2$$

$$= 0.000227 \text{ in}^2$$

Uncertainty in $U_{\%RA}$,

$$U_{\%RA} = \left[\left(\frac{\partial \%RA}{\partial A_i} * U_{A_i} \right)^2 + \left(\frac{\partial \%RA}{\partial A_f} * U_{A_f} \right)^2 \right]^{\frac{1}{2}} \qquad \text{(E.5)}$$

$$\%RA = \left(\frac{A_i - A_f}{A_i}\right) * 100$$

$$= \left(1 - \frac{A_f}{A_i}\right) * 100$$

$$\frac{\partial \%RA}{\partial A_i} = \frac{100 A_f}{A_i^{\,2}}$$

$$= 674.761$$

$$\frac{\partial \%RA}{\partial A_f} = -\frac{100}{A_i}$$

$$= -2028.398$$

Substituting the values in equation E.5,

$$U_{\%RA} = \left[(674.761 * 0.000393)^2 + (-2028.398 * 0.000227)^2\right]^{\frac{1}{2}}$$

$$= 0.532 \text{ in}^2$$

E.2. Uncertainty Calculation for Parameters derived from SSR Results

E.2.1. Calculation of Uncertainty in Time-to-Failure (U_{TTF})

The TTF is obtained from the Filed Point software of the SSR unit, which is accurate up to 1/100th of a second in finding the TTF. Therefore, the uncertainty of the TTF in the SSR testing is negligible.

E.3. Uncertainty Calculation for Parameters derived from CPP Results

The uncertainty of the potentiostat provided by the manufacturer is ± 0.003 mV within a range of 1 mV.

Sample calculation:

For corrosion potential (E_{corr}) = 302 mV

The uncertainty in E_{corr} = 302*0.003 = ± 0.906 mV

One example of the use of the uncertainty analysis is shown in this section. This can be implemented to all experimental results discussed in this thesis.

BIBLIOGRAPHY

1. B. C. R. Ewan, R. W. K. Allen "A figure of merit assessment of the routes to hydrogen," *International Journal of Hydrogen Energy*, Volume 30, 2005, pp. 809 – 819.
2. Paul M. Mathias, Lloyd C. Brown, "Thermodynamics of the sulfur-iodine Cycle for Thermochemical Hydrogen Production," *Presented at the 68th Annual meeting of the society of Chemical Engineers*, Japan, March, 2003.
3. How the hydrogen economy works by Marshall Brain, www.howstuffworks.com
4. Leon Walters, David Wade, and David Lewis, "Transition to a Nuclear/Hydrogen Energy System," *World Nuclear Association Annual Symposium*, London, September, 2002.
5. Stephen Goldstein, Lean Marc Borgard, Xavier Vitart, "Upper bound and best estimate of the efficiency of the iodine sulphur cycle," *International Journal of Hydrogen Energy*, Volume 30, 2005, pp. 619 – 626.
6. G. E. Beghi, "Development of thermochemical and hybrid processes for hydrogen production," *International Journal of Hydrogen Energy*, Volume 10, No. 7/8, 1985, pp. 431 – 438.
7. James E. Funk, "Thermochemical hydrogen production: past and present," *International Journal of Hydrogen Energy*, Volume 26, 2001, pp. 185 – 190.

8. Bilge Yildiz, Mujid S. Kazimi, "Efficiency of hydrogen production systems using alternative nuclear energy technologies," *International Journal of Hydrogen Energy*, Article in press.

9. D. O'Keefe, C. Allen, G. Besenbruch, L. Brown, J. Norman, R. Sharp, "Preliminary results from bench-scale testing of a sulfur-iodine thermochemical water-splitting cycle," *International Journal of Hydrogen Energy*, Volume 7, No. 5, 1982, pp. 381 – 392.

10. Swindeman, R. W., Maziasz, P. J., "Evaluation of advanced alloys relative to alloy design criteria for steam service," *Oak ridge National Laboratory Report* (1991), pp. 59.

11. Ganeshan, P., Smith, G. D., Tassen, C. S., "Mechanical properties and corrosion resistance of Incoloy alloy 803," *Applications and Materials Performance, Proceedings of the Nickel Cobalt 97 International symposium*, Sudbury, Ontario, August 17-20, 1997, pp. 97-111.

12. P. Dumaz, C. Regnard, G. Robert and J. M. Terriez, "Microstructure Effects and Modeling of Incoloy 800 Behavior," *Res Mechanica*, Volume 21, 1987, pp. 165-189.

13. F. A. Khalid, N. Hussain, K. A. Shahid, "Microstructure and Morphology of High Temperature Oxidation in Superalloys," *Materials Science and Engineering*, Volume A265, 1999, pp. 87-94.

14. P. D. Hicks and C. J. Altstetter, "Internal Hydrogen Effects on Tensile Properties of Iron-and Nickel-Base Superalloys," *Metallurgical Transactions*, Volume 21A, February 1990, pp. 365-372.

15. Narendra Kothapalli, "Characterization of Alloy C-276 as a Structural Material for High-Temperature Heat Exchangers," M.S. Thesis, Department of Mechanical Engineering, University of Nevada, Las Vegas, Summer 2005.

16. A technical publication prepared by "The Special Metals Corporation," Publication Number SMC-047, Sep. 2004, pp. 1-13.

17. Yoshio Monma, Masao Sakamoto, Akimtsu Miyazaki, "Assessment of Elevated-Temperature Property Data for Alloy 800H," *Transactions of National Research Institute for Metals*, Volume 26, No. 3, 1984.

18. Betteridge W. et al., "Alloy 800," Proc. Petten International Conference, North-Holland 1978, pp. 3-19.

19. Koinuma A, "Symposium on the Maintenance of components and piping materials in high-temperature reactors," *Society of Chemical Engineers*. Japan, 1980, pp. 20-23.

20. Nickel Topics, No.1, 8, *International Nickel Company*. 1981.

21. Wada, Y, Private communications, O-arai Eng. Center, PNC.

22. M. E. Abd El-Azim, "Correlation between and tensile and creep data in Alloy 800H at 850°C," *Journal of Nuclear Materials*, Volume 231, 1996, pp. 146-150.

23. H. Mecking, Work Hardening in Tension and Fatigue, AIME, New York, 1997, pp. 67.

24. R. R. Jensen, T. E. Howson and T. K. Tien, Superalloys, ASM, Metals Park, OH, 1980, pp. 679.

25. S. L. Mannan and P. Rodriguez, High Temperature Material Processing 6, 1984, pp. 225.

26. M. Steen, W. Provast and A. Dhooge, Structural Mechanics in Reactor Technology, Volume L, Amsterdam, 1985, pp. 99.

27. A. Gutierrez, J. de Damborenea, "Laser-Surface-alloying of iron based superalloy Incoloy-800H with Al," *Materials Science and Processing*, 1996, Volume Applied Physics A 63, pp. 461-465.

28. W. J. Molloy, Advanced Materials Processing, 1990, pp. 23.

29. T. Khan, Advanced Materials Processing, 1990, pp. 19.

30. G. W. Goward, Materials Science and Technology 2, 1986, pp. 194.

31. R. W. Richards, R. D. Jones, P. D. Clements, and H. Clarke, International Materials Rev. 39, 1994, pp. 191.

32. G. C. Wood and F. H. Scott, Materials Science and Technology 3, 1987, pp. 519.

33. R. C. Hurst and J. F. Norton, "The effect of high temperature carburization upon the ambient temperature ductility of Alloy 800H," *High Temperature Technology*, November 1983, pp. 319-325.

34. Schnass, A. and Grabke, H. J., "Changes in material properties of austenitic Cr Ni Fe-alloys by carburization," *Werkstoffe and Korrosion 29*, 1978, pp. 635-644.

35. Wenschhof, D. E. and Harris, J. A., "The influence of carburization on the mechanical wrought nickel alloys," *Corrosion 34*, No. 1, 1978, pp. 23-26.

36. Guttmann, V. and Burgel, R., "The effect of a carburizing environment on the creep behavior of some austenitic steels," Corrosion Resistance Materials for Coal Conversion Systems, Applied Science Publishers Ltd., 1983, pp. 423-438.

37. Ennis, P. J. and Lupton, D. F., "The relationship between carburisation and ductility loss," Proc. Conf. on Behavior of High Temperature Alloys in Aggressive Environments, *The Metals Society*, 1980, pp. 979-991.

38. G. Palumbo, P. J. King and K. T. Aust, "Pitting Corrosion Behavior of Alloy 800 in Chloride-Sulfate Media," *National Association of Corrosion Engineers*, January 1987, Volume 43, No. 1, pp.37-45.

39. J. Hickling, N. Wieling, Corrosion, Volume 37, No. 3, 1981, pp. 147.

40. P. J. King, D. P. Dautovich, Nuclear Technology, Volume 55, 1981, pp. 196.

41. G. Bellamy, et al., Proc. 2nd International Symposium of Environmental Degradation of Materials in Nuclear Power Systems-Water Reactors, *National Association of Corrosion Engineers*, Houston, Texas, 1986, pp. 247.

42. P. V. Balakrishnan, Proc. International Water Conference, Engineering Society of Western Pennsylvania, Pittsburgh, Pennsylvania, 1977, pp. 131.

43. Anon., "Nickel-chromium-iron alloy resists corrosion at high heat," *Advanced Materials and Processes*, Volume 161, December 2003, pp 9-EOA.

44. Udo Bruch and Dieter Schuhmacher, "Tensile and Impact properties of candidate alloys for high-temperature gas-cooled reactor applications," *Nuclear Technology*, 1984, Volume 66, pp. 357-362.

45. E. A. Polman, T. Fransen, and P. J. Gellings, "High-Temperature Corrosion and Mechanical Properties of protective scales on Incoloy 800H: The influence of Preoxidation and Ion Implantation." *Oxidation of metals*, 1990, Volume 33, pp. 135-155.

46. ALLOY 800/800AT/800H technical data, www.hightempmetals.com

47. Heat Resistant Nickel Alloy Plate, http://www.sandmeyersteel.com/index.html

48. Alloy 800H Technical data, www.cornes.com.sg

49. High Performance Alloys, Incoloy 800H, http://www.hpalloy.com/index.html

50. Heat Resistant Alloys, Incoloy® 800H/800HT®, www.painc.com

51. Alloy 800H/HT, Material Data Safety Sheet, www.corrosionmaterials.com

52. Heat Resistant Alloys, www.multialloys.co.za

53. High-Temperature Steels and Alloys, www.m-woite.de

54. High-Temperature Alloys, Incoloy 800H/HT, www.a-1wire.com

55. Metal Samples, Corrosion Monitoring Systems, http://www.alspi.com/ms.htm

56. Corrosion, Wear & Heat Resistant Alloys and High-Performance Superalloys, http://www.rey.it/alloy.html

57. ASTM E 8 04, "Standard Test Methods for Tension Testing of Metallic Materials," *Annual Book of ASTM Standards*, Volume 03.01 (West Conshohocken, PA: ASTM International, 2004), pp. 86-109.

58. March, J. L., Ruprecht, W. J., and Reed, George, "Machining of Notched Tension Specimens," ASTM Bulletin, ASTBA, *American Society for Testing and Materials*, No.244, 1960, pp. 52-55.

59. R. C. Juvinall, K. M. Marshek, "Fundamentals of Machine Component Design," 3rd ed. (New York, NY: John Wiley and Sons), figure 4.36(b), pp. 146.

60. ASTM Designation G 38 (01), "Standard practice for making and using C-Ring stress-corrosion test specimens," *American Society for Testing and Materials (ASTM) International.*

61. ASTM Designation G 30 (97), "Standard practice for making and using U-Bend stress-corrosion test specimens," *American Society for testing and Materials (ASTM) International.*

62. Corrosion Testing Equipment, Cortest, Incorporated. http://www.cortest.com

63. A. K. Roy, S. Pothana, H. Aquino, B. J. O'Toole, M. B. Trabia, Z. Wang, "Environment-Assisted-Cracking of Cladding Materials under Different Loading Conditions", November 30, 2002.

64. ASTM Designation G 129-00, "Standard Practice for Slow Strain Rate Testing to Evaluate the Susceptibility of Metallic Materials to Environmentally Assisted Cracking," *American Society for Testing and Materials (ASTM) International.*

65. Slow-Strain-Rate Testing, Corrosion Source Website http://www.corrosionsource.com/handbook/testing/ssrt.htm

66. A. K. Roy, et al., "Effect of Controlled Potential on SCC of Nuclear Waste Package Container Materials," *Proceedings of NACE Corrosion 2000*, Paper No. 00188, Orlando, FL (2000).

67. A. K. Roy, et al., "Stress Corrosion Cracking of Ni-Base and Ti Alloys Under Controlled Potential," 7th *International Conference on Nuclear Engineering*, Paper No. ICONE-7048, Tokyo, Japan, April 19-23, 1999.

68. A. K. Roy, et al., "Cracking of Titanium Alloys under Cathodic Applied Potential," *Micron, Elsevier Science*, 2001, Volume 32, pp. 211–218.

69. ASTM Designation G 05-94 (1999) e1, "Standard Reference Test Method for Making Potentiostatic and Potentiodynamic Anodic Polarization Measurements," *American Society for Testing and Materials (ASTM) International.*

70. Etchants for Ni-superalloys, www.metallography.com

71. X. Wang, E. Brunger, and G. Gottstein, "Microstructure characterization and dynamic recrystallization in an Alloy 800H," *Materials Science and Engineering A*, Volume 290, 2000, pp. 180-185.

72. E. Brunger, X. Wang, and G. Gottstein, "Nucleation Mechanisms of Dynamic recrystallization in austenitic steel Alloy 800H," *Scripta Materialia*, Volume 38, 1998, pp. 1843-1849.

73. Unnikrishnan Valliyil, "The role of applied potential on cracking of Zircaloy-2," M.S. Thesis, Department of Mechanical Engineering, University of Nevada, Las Vegas, Summer 2005.

74. Elumalai Govindaraj, "Corrosion Study of Zirconium Alloys under Controlled Cathodic Potential," M.S. Thesis, Department of Mechanical Engineering, University of Nevada, Las Vegas, Summer 2005.

75. F. G. Hodge and R. W. Kirchner, "An Improved Ni-Cr-Mo Alloy for Corrosion Service", *Corrosion-NACE*, August 1974, pp.332-336.

76. Richard A. Corbett and William S. Morrison, "Comparative Corrosion Resistance of Some High-Nickel, Chromium-Molybdenum Alloys", *Materials Performance*, February 1989, pp.56.

77. S. C. Tjong, "Localized Corrosion Behavior of Ni-Base Superalloys", *Metals Forum*, Volume 7, 1984, pp. 251-253.

78. A. K. Roy, et al., "A Comparative Study of Alloys C-22 and 625," 8th International *High Level Radioactive Waste Management Conference* (IHLRWM), May 1998, Las Vegas, Nevada, pp. 666-668

79. A. K. Roy, et al., "Localized Corrosion Behavior of Candidate Nuclear Waste Package Container Materials," *Materials Performance*, NACE International, vol. 37, March 1998, pp. 54-58

80. Ancila Kaiparambil, "Corrosion Study of Zirconium Alloys under Controlled Cathodic Potential," M.S. Thesis, Department of Mechanical Engineering, University of Nevada, Las Vegas, Summer 2005.

81. M. E. Abd El-Azim, K. E. Mohamed and F. H. Hammad, "The deformation characteristics of alloy 800H and alloy 617," *Mechanics of Materials*, 1992, Volume 14, pp. 33-46.

82. Seong-Gu Hong, Soon-Bok Lee, "Mechanism of dynamic strain aging and characterization of its effect on the low-cycle fatigue behavior in type 316L stainless steel," *Journal of Nuclear Materials*, 2005, Volume 340, pp. 307-314.

83. L. H. de Almeida, S. N. Monteiro, Proceedings of the second International Conference on Mechanical Behavior of Materials, Boston, 1976, pp. 1697.

84. C. Gupta, J. K. Chakravartty, S. L. Wadekar, J. S. Dubey, *Materials Science and Engineering A*, Volume 292, 2000, pp. 49.

85. Y. Bergsrom, W. Roberts, *Acta Metallurgica*, 19, 1971, pp. 1243.

86. Soon H. Hong, Hee Y. Kim, Jin S. Jang and H. Kuk, "Dynamic strain aging behavior of Inconel 600 Alloy," *Superalloys*, 1996, pp. 401.

87. H. Wilson, M. A. Korhonen and Chen Yu Li, "Effects of grain boundary sliding on the flow properties of Incoloy 800H," *Materials Science and Engineering A*, Volume 156, 1992, pp. 33-EOA.

88. J. W. Edington, *Prog. Materials Science*, 21, 1976, pp. 63.

89. J. W. Edington, *Metallurgical Transactions A*, 13, 1982, pp. 703.

90. W. D. Nix, *Superplastic Forming*, American Society for Metals, Metals Park, OH, 1985, pp. 3.

91. Physical Metallurgy Principles by Reza Abbaschian, Robert E. Reed-Hill, pp 295-297.

92. A. K. Roy, et.al. "Tensile Properties of Martensitic stainless steels at elevated temperatures," *Journal of Materials Engineering and Performance*, Volume 14(2), April 2005, pp 212 – 218.

93. D. Gavillet, P. Marmy, and M.Victoria, "The Microstructure of the 1.4914 MANET Martensitic Steel before and after Irradiation with 590 MeV Protons," *Journal of Nuclear Materials*, Volume 890, 1992, pp 191-194.

94. P. Marmy, J.L. Martin, and M. Victoria, "Deformation Mechanisms of Ferritic-Martensitic Steel between 290 and 870 K," *Materials Science Engineering*, Volume A164, 1993, pp 159-163.

95. M. Victoria, D. Gavillet, P. Spatig, F. Rezia-Aria, and S. Rossman, " Microstructure and Mechanical Properties of Newly Developed low Activation Martensitic Steels," *Journal of Nuclear Materials*, Volume 233-237, 1996, pp 326-330.

96. Paul E. Manning, "An Improved Intergranular Corrosion Test for Hastelloy Alloy C-276", *Laboratory Corrosion Tests and Standards*, ASTM STP 866, pp.437-454.

97. Jack P. Holman, "Experimental Methods for Engineers," McGraw-Hill Book Company, 4th Edition, pp. 50.

VITA

Graduate College
University of Nevada, Las Vegas

Vinay Virupaksha

Address:

4210, Cottage Circle, Apt # 4
Las Vegas, NV 89119, USA.

Degree:

Bachelor of Engineering, Mechanical Engineering, 2001
University of Mysore, Mysore, India

Special Honors and Awards:

- Secured III Rank in the Bachelor's Degree Program for University of Mysore.

Publications:

- Vinay Virupaksha, Ajit Roy, "Characterization of Alloy 800H for Heat Exchanger Applications," MS&T Conference, September 26-28th, 2005, Pittsburgh, PA, USA.
- Vinay Virupaksha, Ajit Roy, "Metallurgical and Corrosion study of Alloy 800H," SAMPE 2005, October 31- November 3rd, 2005, Seattle, WA, USA.
- Vinay Virupaksha, Ajit Roy and et al., "Use of Alloy 800H as a Heat-Exchanger Material," AIChE Conference, October 30-November 4th, 2005, Cincinnati, OH, USA.

- Vinay Virupaksha, Ajit Roy, "High-Temperature Deformation Characteristics and Corrosion Susceptibility of Alloy 800H," MRS Fall 2005, November 28-December 2nd, 2005, Boston, MA, USA
- Vinay Virupaksha, Ajit Roy, "Performance of Alloy 800H at Elevated Temperature for Heat-Exchanger Application," TMS Conference, March 13-16th, 2006, San Antonio, TX, USA. (Abstract)

Thesis Title: "Use of Alloy 800H for Applications in Hydrogen Generation using Nuclear Power"

Thesis Examination Committee:
Chairperson, Dr. Ajit K. Roy, Ph. D.
Committee Member, Dr. Anthony E. Hechanova, Ph. D.
Committee Member, Dr. Brendan J. O'Toole, Ph. D.
Graduate College Representative, Dr. Edward S. Neumann, Ph. D.